

Applied Pyrolysis for Conversion of Sewage Sludge into Value-Added Products

Ali Zaker

A Thesis
In the Department
of
Building, Civil and Environmental Engineering

Presented in Partial Fulfillment of the Requirements
For the Degree of
Doctor of Philosophy (Civil Engineering) at
Concordia University
Montreal, Quebec, Canada

September 2021

© Ali Zaker, 2021

CONCORDIA UNIVERSITY
SCHOOL OF GRADUATE STUDIES

This is to certify that the thesis prepared

By: **Ali Zaker**

Entitled: **Applied Pyrolysis for Conversion of Sewage Sludge into Value-Added Products**
and submitted in partial fulfillment of the requirements for the degree of

Doctor of Philosophy (Civil Engineering)

complies with the regulations of the University and meets the accepted standards with respect to originality and quality.

Signed by the final examining committee:

_____ Chair
Dr. Tiberiu Popa

_____ External Examiner
Dr. Dongling Ma

_____ External to Program
Dr. Mehdi Hojjati

_____ Examiner
Dr. Fuzhan Nasiri

_____ Examiner
Dr. Chunjiang An

_____ Thesis Supervisor
Dr. Zhi Chen

Approved by _____
Dr. Michelle Nokken, Graduate Program Director

13 September, 2021

Dr. Mourad Debbabi, Dean
Gina Cody School of Engineering and Computer Science

ABSTRACT

Applied Pyrolysis for Conversion of Sewage Sludge into Value-Added Products

Ali Zaker, Ph.D.

Concordia University, 2021

Reducing sewage sludge (SS) waste has been a substantial challenge in urban areas. Utilization of SS with organic-rich residue as a renewable resource for conversion to value-added products is an alternative solution. It can manage the continuously increasing SS generation while is an appealing pathway for energy sustainability and environmental protection. In this respect, pyrolysis is a promising technology for the thermochemical valorization of SS to useful products, including char, bio-oil and bio-gas with different applications. Accordingly, in the present research, the thermal behaviors, kinetics and thermodynamics of SS and low-density polyethylene (LDPE) during co-pyrolysis were studied through thermogravimetric analysis. Discrepancies between theoretical and experimental weight loss curves as a measurement of the extent of synergic effect proved the existence of chemical interactions during the process. Meanwhile, kinetic and thermodynamic parameters provided vital information on the degradation behavior of the reactants. Furthermore, this work focused on extending the application of activated char (AC) derived from pyrolysis of SS. In this context, a fixed bed pyrolysis reactor system was designed and implemented. Firstly, the produced AC was used as an alternative catalyst to HZSM5 in catalytic pyrolysis of SS. As a result, both catalysts promoted SS pyrolysis reaction rate by abridging the average activation energy. Interestingly, the catalysts effectively reduced the harmful evolved gaseous generated during the process (eg., CH₄, CO₂, HCN, NO₂, SO₂ and CH₃SH). Moreover, the bio-oil composition analysis showed a major upgrade in terms of oxygen-nitrogen-containing compounds removal. Upgraded bio-oil was dominated by C4-C9 hydrocarbons (72%) at higher catalyst loadings. Also, generation of value-added chemicals such as light aromatic hydrocarbons was enriched in the catalytic process. Secondly, the application of sludge-based AC, as a sorbent, for the recovery of oil spills on surface waters was invested. The inherent Fe-minerals in SS texture were converted to magnetic Fe₃O₄ particles during the pyrolysis reaction allowing the exhausted sorbent to be recovered with a magnetic field. Concurrently, superhydrophobic property was created by modification of AC with myristic acid, resulting in a water contact angle

of 152.2°. Feasibility studies proved the potential use of sludge-based sorbent for oil spill response operations.

ACKNOWLEDGEMENTS

With all the effort, struggle and spirit, I am very glad to say that finally, this project has come to an end. For this, I would like to express my deepest gratitude and sincere appreciation to professor Zhi Chen for his continuous encouragement, constructive criticism, enthusiastic guidance, support, trust and understanding throughout my doctoral program.

I would like to thank Ms. Hong Guan and Mr. Josef Hrib, experience technicians of the Department of Building, Civil and Environmental Engineering at Concordia University, which gave me invaluable training and assistance throughout my program.

Special thanks to Dr. Galyna Shul from the NanoQAM facilities at the Université du Québec à Montréal for her valuable guidance during my experiments.

My appreciation also goes to my committee members viz: Dr. Fuzhan Nasiri, Dr. Chunjiang An, Dr. Mehdi Hojjati, Dr. Ali Dolatabadi and Dr. Dongling Ma for their inputs that helped improve the results of my work.

Finally, I would like to thank all of my friends (too many to list here) for providing the friendship and support that I needed.

DEDECATION

This work is dedicated to my beloved parents.

Dr. Farhad Zaker

Mahnaz Baghery Shad

All my honors are for my parents. Under their influence, I have been with a heart of appreciation of the world. I am especially grateful to them who have been continuously supporting me and giving me the best education throughout my entire life. Without their optimism, trust, love, motivation, inspiration and support, any accomplishment would not have been possible.

I owe everything that I am to the greatest teachers in my life,
my parents.

TABLE OF CONTENTS

| | |
|--|------|
| LIST OF FIGURES | xi |
| LIST OF TABLES..... | xiii |
| NOMENCLATURE | xv |
| CHAPTER 1 | |
| INTRODUCTION | 1 |
| 1.1. Background and significance of research | 1 |
| 1.2. Problem statement | 2 |
| 1.3. Research objectives | 4 |
| 1.4. Thesis outline..... | 4 |
| CHAPTER 2 | |
| LITERATURE REVIEW | 7 |
| 2.1. Sewage sludge | 7 |
| 2.2. Sewage sludge pyrolysis technologies..... | 9 |
| 2.3. Kinetic study of sewage sludge | 11 |
| 2.4. Pyrolysis: a potential route for sewage sludge valorization | 12 |
| 2.5. Co-pyrolysis of sewage sludge | 14 |
| 2.6. Catalytic pyrolysis of sewage sludge | 17 |
| 2.7. Production of sludge-derived AC for different applications | 18 |
| 2.8. Summary of the literature review | 20 |
| CHAPTER 3 | |
| EXPERIMENTAL SECTION | 22 |
| 3.1. SS preparation and characterization | 22 |
| 3.2. Thermogravimetric (TGA) evaluation | 23 |
| 3.3. Kinetic theory | 24 |
| 3.4. Pyrolyzer system design | 25 |
| 3.4.1. Optimization of pyrolyzer set-up | 27 |
| 3.5. AC preparation and characterization..... | 29 |

CHAPTER 4

CO-PYROLYSIS OF SEWAGE SLUDGE AND LOW-DENSITY POLYETHYLENE: A THERMOGRAVIMETRIC STUDY OF THERMO-KINETICS AND THERMODYNAMIC PARAMETERS 31

4.1. Introduction..... 31

4.2. Material and methods..... 33

4.2.1. Materials 33

4.2.2. Pyrolysis and co-pyrolysis using TGA 34

4.2.3. Assessment of synergistic effects 35

4.2.4. Kinetic approaches..... 35

4.2.4.1. Model-fitting method..... 35

4.2.4.2. Model-free methods..... 36

4.2.5. Thermodynamic parameters calculation..... 37

4.3. Results and discussion 37

4.3.1. Thermal behavior 37

4.3.2. Evaluation of synergistic interaction 43

4.3.3. Evaluation of model-fitting kinetic..... 46

4.3.4. Evaluation of model-free kinetics..... 47

4.3.5. Evaluation of thermodynamic parameters..... 53

4.4. Conclusion 59

CHAPTER 5

CATALYTIC PYROLYSIS OF SEWAGE SLUDGE WITH HZSM5 AND SLUDGE-DERIVED ACTIVATED CHAR: A COMPARATIVE STUDY USING TGA-MS AND ARTIFICIAL NEURAL NETWORKS 60

5.1. Introduction..... 60

5.2. Materials and methods 62

5.2.1. Materials 62

5.2.2. Simultaneous TGA/MS analysis..... 62

5.2.3. Kinetic study 63

5.2.4. Artificial neural network development..... 63

5.3. Results and discussion 65

| | |
|---|-----|
| 5.3.1. Characteristics of AC catalyst | 65 |
| 5.3.2. Thermal decomposition behavior analysis | 69 |
| 5.3.3. Kinetic evaluation | 71 |
| 5.3.4. Monitoring pyrolysis gaseous | 75 |
| 5.3.5. Thermal decomposition prediction by ANN model | 79 |
| 5.3.6. Bio-oil analysis by GC/MS | 81 |
| 5.4. Conclusion | 86 |
| CHAPTER 6 | |
| DEVELOPMENT OF SLUDGE-BASED ACTIVATED CHAR SORBENT WITH ENHANCED | |
| HYDROPHOBICITY FOR OIL SPILL CLEANUP | |
| 88 | |
| 6.1. Introduction..... | 88 |
| 6.2. Materials and methods | 90 |
| 6.2.1. Materials | 90 |
| 6.2.2. Sorbent synthesis | 91 |
| 6.2.3. Characterization of sorbent | 91 |
| 6.2.4. Oil sorption capacity..... | 91 |
| 6.2.5. Reusability..... | 93 |
| 6.3. Results and discussion | 94 |
| 6.3.1. Detailed characterization of sorbent | 94 |
| 6.3.1.1. FT-IR analysis..... | 94 |
| 6.3.1.2. X-ray diffraction | 95 |
| 6.3.1.3. Morphology and textural studies | 96 |
| 6.3.1.4. Contact angle measurements..... | 97 |
| 6.3.2. Sorption capacity studies | 99 |
| 6.3.3. Sorbent reusability | 101 |
| 6.4. Conclusions..... | 102 |
| CHAPTER 7 | |
| CONCLUSION AND FUTURE WORK..... | |
| 103 | |
| 7.1. Overall conclusion..... | 103 |
| 7.2. Contribution of research | 104 |
| 7.3. Recommendations for future work..... | 104 |

| | |
|--|-----|
| References | 106 |
| Appendix A: Compounds of bio-oil detected by GC/MS | 125 |

LIST OF FIGURES

| | |
|--|----|
| Fig. 1.1. Technical route of this dissertation. | 6 |
| Fig. 3.1. Lab-scale horizontal fixed bed pyrolysis reactor system: a) Schematic diagram: (1) Nitrogen cylinder, (2) Flow meter, (3) Valve, (4) Furnace, (5) Crucible containing sample, (6) Quartz tube with flanges on both sides, (7) Ice bath, (8) Vacuum trap, (9) Gas bag; b) digital photo. | 27 |
| Fig. 3.2. Effect of final temperature on product distribution from pyrolysis of SS. | 28 |
| Fig. 4.1. (a) TGA and (b) DTG curves of individual SS, LDPE and their blends at $\beta=30$ °C/min. | 38 |
| Fig. 4.2. Co-pyrolytic (a) TGA and (b) DTG curves of SL-50 at different $\beta=10, 20, 30$ and 40 °C/min. | 42 |
| Fig. 4.3. Comparison between experimental and calculated TGA/DTG curves for the (a) SL-25, (b) SL-50 and (c) SL-75 at $\beta=30$ °C/min. | 45 |
| Fig. 4.4. Linear fit plots for determining E value of the SL-50. Where, $\ln(\beta/T^2)$, $\ln(\beta)$ and $\ln(\beta/T^{1.8})$ were plotted against inverse of pyrolysis temperature using KAS (a), FWO (b) and Starink (c) methods, respectively. | 49 |
| Fig. 4.5. E (kJ/mol) value as a function of conversion. | 52 |
| Fig. 5.1. (a) SEM image and (b) EDX of the AC catalyst. | 66 |
| Fig. 5.2. FT-IR spectrum of AC catalyst. | 67 |
| Fig. 5.3. TGA/DTG curves for AC catalyst. | 68 |
| Fig. 5.4. TGA/DTG curves for SS, SSHZSM5@1-1 and SSAC@1-1. | 71 |
| Fig. 5.5. Degree of conversion of SS, SSHZSM5@1-1 and SSAC@1-1 during pyrolysis and catalytic pyrolysis at $\beta=10$ °C/min. | 72 |
| Fig. 5.6. The relation between reaction stages and activation energy for SS, SSHZSM5@1-1 and SSAC@1-1. | 74 |

| | |
|--|-----|
| Fig. 5.7. The relation between reaction stages and average activation energy (E_m) for SS, SSHZSM5@1-1 and SSAC@1-1. | 75 |
| Fig. 5.8. Single ion current profiles monitored using MS during SS, SSHZSM5@1-1, and SSAC@1-1 pyrolysis. | 79 |
| Fig. 5.9. Comparison of experimental and ANN predicted model (ANN7-1) for SSAC@1-1 catalytic pyrolysis. | 81 |
| Fig. 5.10. Total ion chromatograms for pyrolysis of SS. | 82 |
| Fig. 5.11. Total ion chromatograms for catalytic pyrolysis of SSHZSM5@4-1 and SSAC@4-1. | 83 |
| Fig. 5.12. Total ion chromatograms for catalytic pyrolysis of SSHZSM5@2-1 and SSAC@2-1. | 84 |
| Fig. 5.13. Total ion chromatograms for catalytic pyrolysis of SSHZSM5@1-1 and SSAC@1-1. | 86 |
| Fig. 6.1(a-e). Schematic depiction of oil removal from the water surface with MAC-SS sorbent via magnet bar. | 93 |
| Fig. 6.2. FT-IR analysis of AC and MAC-SS. | 96 |
| Fig. 6.3. XRD patterns of AC and MAC-SS. | 96 |
| Fig. 6.4. SEM spectra of MAC-SS. | 97 |
| Fig. 6.5. (a) Optical image of a water droplet with spherical shape on MAC-SS surface, (b) CA of $152.2^\circ \pm 3.2$. h. | 99 |
| Fig. 6.6. The oleophilic surface of MAC-SS which the motor oil spread has penetrated the inner pores of the MAC-SS with a CA of 0° | 99 |
| Fig. 6.7. Variation in the sorption capacity of MAC-SS (g/g) on recycling of motor oil and light crude oil. | 102 |

LIST OF TABLES

| | |
|---|----|
| Table 2.1. The range of main operating parameters for pyrolysis processes..... | 10 |
| Table 2.2. Representative kinetic parameters of different models for the pyrolysis of SS..... | 12 |
| Table 2.3. Summary of co-pyrolysis of SS with different co-reactants. | 15 |
| Table 2.4. Kinetic model and activation energy for co-pyrolysis of SS with various co-reactants. | 17 |
| Table 3.1. Main characteristics of SS..... | 23 |
| Table 3.2. Different apparatuses employed during experimental procedure and uncertainty in measurement of the parameters. | 24 |
| Table 4.1. Main characteristics of SS and LDPE. | 34 |
| Table 4.2. Pyrolysis and co-pyrolysis characteristic parameters for SS, LDPE and their blends at $\beta=30$ °C/min..... | 41 |
| Table 4.3. Co-pyrolysis characteristic parameters for SL-50 blend at different β | 43 |
| Table 4.4. Kinetic parameters for SS and LDPE pyrolysis and co-pyrolysis of their blends. | 47 |
| Table 4.5. Activation energy (E), pre-exponential factor (A) and correlation coefficients (R^2) obtained from KAS, FWO and Starink methods for the solo-pyrolysis of SS and LDPE and co- pyrolysis of SL-50 blend. | 51 |
| Table 4.6. Thermodynamics parameters of SS, LDPE and SL-50 using KAS method. | 56 |
| Table 4.7. Thermodynamics parameters of SS, LDPE and SL-50 using FWO method. | 57 |
| Table 4.8. Thermodynamics parameters of SS, LDPE and SL-50 using Starink method. | 58 |
| Table 5.1. Identified pyrolytic gaseous by MS. | 63 |
| Table 5.2. Parameters used for the development of ANN model. | 65 |
| Table 5.3. Comparison of the BET results of AC derived from SS pyrolysis. | 69 |
| Table 5.4. Comparison of different ANN structure performances for SSAC@1-1. | 80 |
| Table 6.1. Characteristics of oil samples studied for sorption. | 92 |

| | |
|--|-----|
| Table 6.2. CA measurement for MAC-SS and reference data..... | 98 |
| Table 6.3. Oil sorption capacity of AC and MAC-SS in comparison to other char-based sorbents. | 100 |
| Table A.1. Major chemical compounds present in pyrolytic bio-oil of SS. | 125 |
| Table A.2. Major chemical compounds present in pyrolytic bio-oil of SSHZSM5@2-1. | 131 |
| Table A.3. Major chemical compounds present in pyrolytic bio-oil of SSAC@2-1. | 133 |
| Table A.4. Major chemical compounds present in pyrolytic bio-oil of SSHZSM5@1-1. | 135 |
| Table A.5. Major chemical compounds present in pyrolytic bio-oil of SSAC@1-1. | 137 |
| Table A.6. Major chemical compounds present in pyrolytic bio-oil of SSHZSM5@4-1. | 139 |
| Table A.7. Major chemical compounds present in pyrolytic bio-oil of SSAC@4-1. | 142 |

NOMENCLATURE

| | |
|--------------------|---|
| SS | Sewage sludge |
| WWTP | Wastewater treatment plant |
| GHGs | Greenhouse gases |
| AC | Activated char |
| FR | Free radicals |
| ME | Metallic elements |
| LDPE | Low-density polyethylene |
| H/C_{eff} | Hydrogen efficiency |
| TGA | Thermogravimetric analysis |
| TG-MS | Thermogravimetric analyzer coupled with mass spectrometer |
| PCB | Polychlorinated biphenyl |
| PAH | Polycyclic aromatic hydrocarbon |
| PCDD | Polychlorinated dibenzodioxin |
| PCDF | Polychlorinated dibenzofuran |
| POP | Persistent organic pollutants |
| MIE | Minimum ignition energy |
| T | Temperature |
| β | Heating rate |
| RT | Residence time |
| p | Particle size |
| DTG | Derivative thermogravimetric |
| DAEM | Distribution activation energy model |
| KAS | Kissinger–Akhira–Sunose |
| FWO | Flynn-Wall-Ozawa |
| E | Activation energy |
| A | Pre-exponential factor |
| R^2 | Correlation coefficient |
| HHV | High heating value |
| α | Conversion rate |

| | |
|------------|--|
| n | Reaction order |
| ICTAC | International Confederation for Thermal Analysis and Calorimetry |
| DCM | Dichloromethane |
| GC/MS | Gas chromatography/mass spectrometry |
| NIST | National Institute of Standards and Technology |
| SEM | Scanning electron microscopy |
| EDX | Energy dispersive X-ray spectroscopy |
| BET | Brunauer-Emmett-Teller |
| FT-IR | Fourier Transform Infrared |
| EHI | Effective hydrogen index |
| RMSE | Root mean square error |
| ΔH | Enthalpy |
| ΔG | Gibbs free energy |
| ΔS | Entropy |
| NMR | Nuclear magnetic resonance |
| ANN | Artificial neural network |
| m/z | Charge ratios |
| MID | Multiple ion detection |
| E_m | Average activation energy |
| FMLP | Feedforward multiple layer perception |
| LM | Levenberg-Marquardt |
| MSE | Mean square error |
| MAE | Mean absolute error |
| MBE | Mean bias error |
| TANSIG | Tangent sigmoid function |
| PURELINE | Linear transfer function |
| DI | De-ionized |
| XRD | X-ray powder diffraction |
| CA | Contact angle |

CHAPTER 1

INTRODUCTION

1.1. Background and significance of research

Sewage sludge (SS) is considered the major solid waste generated from the treatment of wastewaters. Based on the demographic projections, the amount of SS will rise while making its management a global issue (Zaker et al., 2019). The upsurge in the quantity of SS generation in recent years is due to the instantaneous expansion of municipalities and industries from human activities. For this reason, disposal of SS has become a serious environmental challenge nowadays. In general, there are two conventional disposals strategies for dealing with SS waste: incineration and landfilling. However, these options are being phased out or coming under pressure due to the emergence of environmental concerns and they suffer from various drawbacks and limitations (e.g. production of greenhouse gases and restrictive environmental regulations) (Chen et al., 2019). Moreover, there has been growing interest in renewable energy sources such as solar energy, wind power, geothermal energy, fuel cells and biomass (Shahbeig and Nosrati, 2020). Interestingly, since SS contains a high amount of organic matter, it can be considered as a biomass source. Thus, the valorization of SS as a sustainable approach has attracted a gradually increasing interest all over the world and novel processes are being developed (Syed-Hassan et al., 2017). One of the emerging management technology is pyrolysis, the thermal degradation process of material in an oxygen-free environment, which can minimize the SS volume while effectively transform the waste into useful end products (char, bio-oil and bio-gas) (Naqvi et al., 2018). Nonetheless, SS pyrolysis conversion involves complex equipment or processes which will inevitably rise the operating and implementing costs. Currently, pyrolysis of SS is under research and development phase. Therefore, in order to move pyrolysis of SS towards commercializing, the end products should have a high financial value.

1.2. Problem statement

The escalating volume of wastewater produced by municipal communities, demands new technology for the treatment/discharge of SS and the safe handling/disposal of the solid residue. For instance, Montreal wastewater treatment plant (WWTP), Jean-R. Marcotte, is one of the largest facilities in the world. A significant amount of SS is generated from primary clarifiers which are incinerated. It has been reported that 267.000 tons of SS is incinerated every year and a quarter of all the greenhouse gases (GHGs) emitted by Montreal city operation is related to the incinerators (“Can Montreal turn its sewage into black gold? | Montreal Gazette,”). Also, there is evidence for emission of considerable amounts of particulates such as several heavy metals, sulfur and nitrogen oxides emitted from the incineration plants in the literature (Hadi et al., 2015). Therefore, investigation on efficient technological strategy to shift SS management practice towards resources recovery is crucial.

Accordingly, pyrolysis may be considered as a cost-effective strategy to this problem, through paths to gain valuable bioenergy while avoiding environmental pollutions (Sfakiotakis and Vamvuka, 2018). Pyrolysis of SS has been studied as parent material in the past; for example, the pyrolysis of SS has been extensively investigated for bio-oil generation (Zaker et al., 2019) and also for obtaining bio-char products that can be used as adsorbents (Hadi et al., 2015). However, the utilization of bio-oil has been restricted because of high oxygen-nitrogen-containing compounds, relatively hydrogen deficiencies (H/C_{eff} molar ratio <0.5) and low heating values (Suriapparao et al., 2018b).

Co-pyrolysis of SS with a hydrogen-enriched feedstock such as plastic can be a potential strategy to enhance reaction performance and properties of the products (Huang et al., 2015). The mechanism is similar to pyrolysis with a second feedstock mixed with SS in the process. There is evidence that plastics could act as hydrogen-donors and enhance the properties of bio-oil by decreasing the oxygen content (Hu et al., 2017). Although several research has been devoted to the co-pyrolysis of SS with different types of feedstocks, co-feeding with plastic wastes to enrich the SS is missing in research. In addition, no unified conclusion on the synergetic effects between the materials has been stated and the studies are limited to a few.

Subsequently, the range of catalysts that have been studied comparatively with SS for upgrading the pyrolytic products is limited in the literature. Most of the research has been devoted

to catalytic pyrolysis of SS with zeolites (Persson et al., 2019; Wang et al., 2017; Xie et al., 2014; Zheng et al., 2018; Zhou et al., 2018) for their usefulness for oxygen and nitrogen removal. Yet, zeolite-based catalysts are relatively expensive, and the catalyst preparation steps are time and energy-consuming. They suffer from rapid deactivation and coke formation with a drop in the liquid yields. It is thus important to explore a feasible solution for the utilization of SS via catalytic pyrolysis. Therefore, this study is an attempt to know the viability of using activated char (AC) derived from SS as a potential catalyst in contrast to commercial HZSM5 in SS pyrolysis for the first time. The sludge-derived AC could be suitable for catalytic purposes because of its bulky surface area, porosity, embedded active sites, availability and most essentially low cost (Daorattanachai et al., 2018; Gao et al., 2020; Zhang et al., 2018b). Notably, metal species such as Fe are dispersed in the sludge-based char matrix inherently which can eliminate the toxic and expensive synthesis procedures. The free radicals (FR) from the evolved volatiles may react with metallic elements (ME) on the surface of AC ($FR + AC-ME \leftrightarrow AC-FR + ME$) (Fu et al., 2018).

In addition, recently, increasing efforts are dedicated to developing sorbent materials with high oil sorption capacity, high oil-water separation efficiency, and superior reusability (Ifelebuegu and Johnson, 2017). Based on the literature survey, a lack of a facile and nontoxic method to fabricate a sorbent with magnetic superhydrophobic properties derived from natural and abundant materials for separation of various types of oils and chemicals from the water was noticed. Sorbents should have excellent hydrophobicity and oleophobicity to the strong affinity water. For that reason, researchers have used chemical modification such as silylation agents as the main hydrophobic treatment methods (Phanthong et al., 2018). Nevertheless, chemical modification methods are costly and highly toxic to aquatic life, thus, their applications are still limited. Moreover, to facilitate the separation of the sorbent from the water magnetic separation has been developed upon research (Ahamad et al., 2019; Ieamviteevanich et al., 2020; Raj and Joy, 2015). The magnetic property is added to the sorbent by usually precipitation technique which is a time and energy-consuming procedure. In this respect, AC derived from pyrolysis of SS can be selected as an interesting candidate for oil spill response. By adjusting pyrolysis reaction conditions, it is evidence that Fe-mineral species in SS can be decomposed to form magnetic Fe_3O_4 particles (Gu et al., 2018). Moreover, decorating sludge-based AC with non-toxic carboxylic acids can enhance hydrophobicity while increasing the oil uptake (Navarathna et al., 2020).

1.3. Research objectives

The general objective of this study is to deliver scientific reference and technical support for the research and further development of pyrolysis conversion technology for SS waste processing. Using pyrolysis reaction, SS waste resources can be transformed into value-added products. In this regard, the intention of this research is two-fold. Firstly, the challenges of SS and plastic waste management and increasing energy demand can promptly be investigated by the co-pyrolysis behavior of SS and low-density polyethylene (LDPE). Secondly, it is interesting to build knowledge on the beneficial use of sludge-derived AC in different applications owing to low-cost and facile generation from pyrolysis. One of the primary goals is to explore the use of AC as an alternative catalyst to HZSM5. The inherent metallic minerals and high surface area with abundant functional groups on the surface make sludge-derived AC a potential material. Other benefits of sludge-based AC include being examined as a high-performance sorbent for oil spill cleanup. In the light of the above discussion, the following objectives are specifically considered as the main targets of this research:

- 1) To design an experimental pyrolysis setup for conversion of SS to value-added products.
- 2) To explore the feasibility and process efficiency of SS and LDPE co-pyrolysis by a combined consideration of multi-heating rates and different blending ratios to evaluate the synergistic effects in terms of different kinetic and thermodynamic parameters models.
- 3) To evaluate the use of sludge-derived AC as an alternative catalyst in contrast to HZSM5 by assessing their potential to reduce harmful pyrolytic gaseous and improving the reaction kinetics while upgrading the bio-oil derived from catalytic pyrolysis of SS.
- 4) To make innovative use of sludge-based AC as an oil spill sorbent with magnetic and superhydrophobic properties.

1.4. Thesis outline

This dissertation contains seven chapters. The motivation of this research is to develop and extend the application of SS pyrolysis for production of value-added products. The main chapters of the thesis are:

Chapter 1 is a general introduction providing the background information relevant to this study.

Chapter 2 reviews previous literature concerning fundamental information associated with chemical composition and thermal behavior to understand the nature of SS. Furthermore, co-pyrolysis and catalytic pyrolysis of SS used for different applications are discussed.

Chapter 3 describes experimental procedures applied in this study and the design and optimization of the pyrolysis setup. Initially, SS characteristics analyses are explained and provided. Next, pyrolysis experiments are described.

Chapter 4 investigates the feasibility of co-pyrolysis of SS and LDPE for the first time. LDPE was used as a hydrogen-donor to increase the effective hydrogen efficiency (H/C_{eff}). The integrated process was carried out by thermogravimetric analysis (TGA). The thermo-kinetics and thermodynamic parameters of co-pyrolysis were systematically examined and a synergistic effect between the SS and LDPE was observed.

Chapter 5 is devoted to the fabrication of sludge-derived AC to be used as an inexpensive and eco-friendly alternative catalyst in contrast to HZSM5 in pyrolysis of SS. In this chapter, the catalytic pyrolysis experiments were conducted using a thermogravimetric analyzer coupled with a mass spectrometer (TG-MS) to explore the process efficiency and evolved pyrolytic gases. In addition, artificial neural networks were trained as a prediction model of the thermal behavior of the catalytic reaction. Meanwhile, the effect of catalyst loading on bio-oil quality from catalytic pyrolysis of SS over sludge-derived AC and HZSM5 was examined in a horizontal fixed bed pyrolysis reactor.

Chapter 6 discusses the utilization of sludge-based AC as a green oil spill sorbent. The sorbent is decorated with a non-toxic myristic acid to improve the oleophobicity and hydrophobicity of the material. Different properties of the sorbent are characterized in detail. Also, sorption capacity studies along with regeneration of the sorbent are carried out.

Chapter 7 presents the overall conclusions and major findings associated with the research objectives. In addition, recommendations for the future work, and implications of this research are suggested.

The technical route of this dissertation is shown in Fig. 1.1.

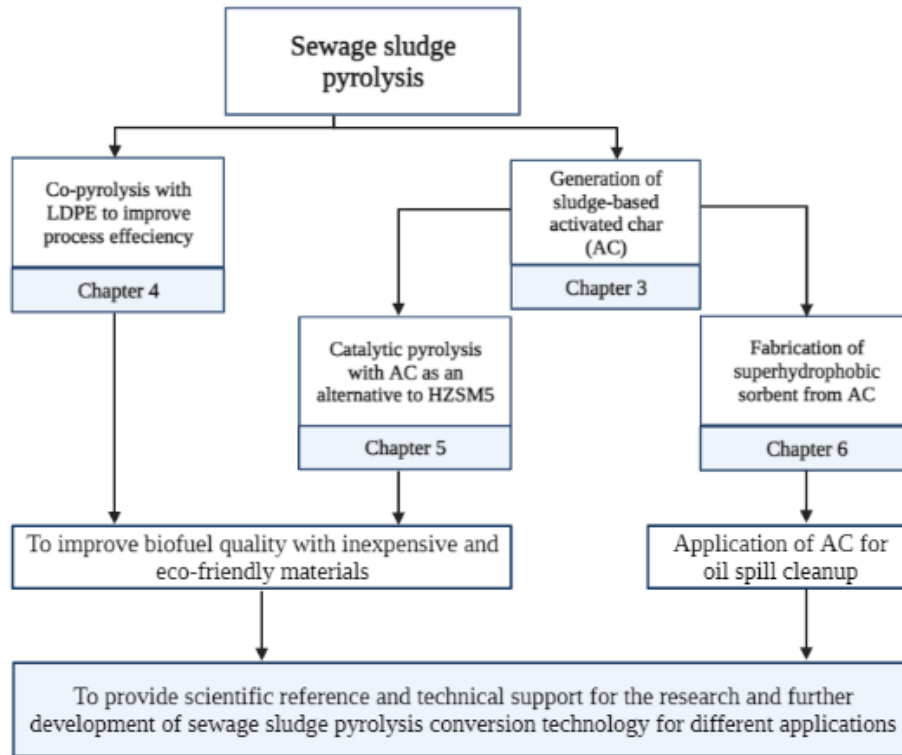


Fig. 1.1. Technical route of this dissertation.

CHAPTER 2

LITERATURE REVIEW

2.1. Sewage sludge

A source of bioenergy, SS is a retained filter cake made by dewatering the solids remaining after treatment in effluent treatment plants (Zaker et al., 2019). It is an unavoidable byproduct of the sewage treatment process which is continuously generated in the form of very dilute suspension (Dai et al., 2018). According to demographic projections for the improvement of living standards, SS is expected to continue increasing in quantity worldwide (Wang et al., 2017). SS can be generated by three main stages of the wastewater treatment process, including the primary (physical and/or chemical), secondary (biological) and tertiary (an addition to the secondary stage, often involving nutrient removal) treatments. In general, the wet sludge is high in water content. This water can be classified into several categories: (i) free (or bulk), (ii) interstitial, (iii) vicinal (or surface) and (iv) chemically bound (or hydration) water (Syed-Hassan et al., 2017). The free and interstitial water is removed using processes such as a belt filter press or centrifuge. The dewatered SS still consists of about 70–85% moisture made up of vicinal water. These water molecules adhere to the particle surface via hydrogen bonding and can only be vaporized and eliminated by applying heat. The sludge is typically very greasy at such high levels of water content, making it difficult to handle and transport (Wzorek, 2012). Correspondingly, the main reason for its foul odor is the result of biologically active substances.

The composition and properties of SS are variable and depend on: (i) the wastewater characteristics and pollutant loading entering the treatment plant (origin of the wastewater), (ii) the treatment method used in the wastewater treatment plant, (iii) environmental legislation, (iv) water reclamation requirements, (v) the processing stage, (vi) seasonal variations, due to which even sludge from the same wastewater treatment plant can vary in its characteristics from one day to the next, and (vii) the duration and conditions of storage and the coagulant agents used (Syed-Hassan et al., 2017).

To determine the convenience of using SS in pyrolysis, it is crucial to determine its physical and chemical characteristics. The components of SS can be categorized into six essential groups:

- 1) Non-toxic organic carbon (60% on a dry basis).
- 2) Components containing nitrogen and phosphorus.
- 3) A wide range of toxic inorganic pollutants including heavy metals such as zinc, copper, nickel, cadmium, lead, mercury, and chromium, which restrict the use of sludge for agricultural purposes (Barakat et al., 2017) and organic pollutants such as (i) polychlorinated biphenyls (PCBs), (ii) polycyclic aromatic hydrocarbons (PAHs), (iii) polychlorinated dibenzodioxins (PCDDs), (iv) polychlorinated dibenzofurans (PCDFs), (v) pesticides, (vi) linear-alkyl-sulfonates, (vii) nonyl-phenols and (viii) polybrominated fire retardants (Liu et al., 2018).
- 4) Pathogens and other microbiological pollutants like living organisms, bacteria, viruses, protozoa and other parasitic helminths, which can result in possible risks to the health of living creatures (Fijalkowski et al., 2014).
- 5) Inorganic compounds such as silicates, aluminates and compounds containing calcium and magnesium.

The nitrogen in SS is mainly derived from the protein in the source material, which results from the microorganisms used for water purification (Fonts et al., 2012; Samolada and Zabaniotou, 2014). The total percentage of nitrogen in SS is variable, which can range from less than 0.1% to a maximum of 18% with a median of 3.3%, while the level of mineral nitrogen may upsurge to 6.7% (Cheng et al., 2018; Ignatowicz, 2017). Similarly to nitrogen, the phosphorus content in SS may vary from less than 0.1% to up to 14% of the dry weight, based on the origin of the raw sludge and the treatment procedure (Shiba and Ntuli, 2017; Tomasi Morgano et al., 2018). The phosphorus in sludge mostly exists in an inorganic form and its bioavailability is influenced by the compounds used for sludge stabilization (Hossain et al., 2011).

There is no significant difference in the concentrations of metals and minerals in sludge in industrialized countries (Praspaliauskas and Pedišius, 2017). It is found that a larger city is usually associated with a higher total concentration of heavy metals (Adar et al., 2016). Zinc, copper, and chrome appear in the highest concentrations, followed by lead and nickel, and cadmium and mercury exist in trivial quantities (Ignatowicz, 2017). PCBs as persistent organic pollutants (POPs) and aforementioned PAHs are very toxic, mutagenic and carcinogenic (Barakat et al., 2017), which

are found in sludge. For instance, a concentration of 5.9 ± 0.1 mg/kg PAHs (inclusive) in SS from municipal sewage treatment is typical (Oleszczuk et al., 2012).

Approximately 60% of the primary energy content of wastewater is attributable to high concentrations of organic carbon and is centralized in SS after treatment. However, only after the SS is dried and the moisture content is reduced to less than 5% can it be considered an attractive source of energy in the pyrolysis process. The energy content is comparable to those of other low-rank fuels, including lignite and most biomass, with a typical minimum ignition energy (MIE) greater than 1000 mJ in the solid form (Fernandez-Anez et al., 2018). Its calorific value is similar to that of sub-bituminous coal (Adar et al., 2016; Syed-Hassan et al., 2017). Moreover, proximate and ultimate analysis play key roles in evaluating the thermochemical conversion fundamentals of biomass. The assessment of the proportions of moisture, volatile matter, fixed carbon and ash is achieved by proximate analysis, while ultimate analysis measures individual elements such as C, H, O, N and S. To understand the pyrolysis of SS, proximate and ultimate analysis must be brought into account.

2.2. Sewage sludge pyrolysis technologies

Pyrolysis technology, despite its long history of use, has recently developed as a frontier research area compared to the widespread application of SS resource recovery techniques such as combustion/incineration, hydrothermal treatment, wet air oxidation or supercritical wet oxidation. Pyrolysis is defined as thermal decomposition of organic components in the absence of oxygen (inert atmosphere) and moderate temperatures, resulting in the production of solid residue, and both condensable and non-condensable gases (Gao et al., 2017; Tsai et al., 2009). In this case, pyrolysis has the potential to transform any type of bio-solid into biofuels and chemicals. Also, pyrolysis produces less greenhouse gas emissions (NO_x and SO_x), it has the potential to be environmentally friendly and more financially beneficial (Praspaliauskas et al., 2018).

The four key operating parameters considered in pyrolysis are as follows: (i) temperature (T , °C), (ii) heating rate (β , °C/s), (iii) residence time (RT, s) and (iv) particle size (p , mm). Pyrolysis can be classified as slow, fast, and flash processes depending on the operating conditions (see Table 2.1) and the ultimate target of products (Al Arni, 2018). Furthermore, Tripathi et al. mentioned three more subclasses of the pyrolysis process: vacuum, intermediate and hydro-

pyrolysis (Tripathi et al., 2016). Vacuum pyrolysis transpires in a low-pressure range of 0.1-0.2 atm and has a similar β to slow pyrolysis. This process allows the formation of immense magnitudes of pyrolysis oil and char, which are considered realistic fuels. The operating conditions of intermediate pyrolysis exist between those of slow and fast pyrolysis, with low residence time and classical product distribution of 50% liquid, 25% char and 25% gas (Mahmood et al., 2013). The yielded liquid is often seen to separate readily into organic and aqueous phases. In terms of viscosity and heating value, the organic phase formed reveals promising qualities (Yang et al., 2014). Hydro-pyrolysis is the exothermic process of decomposition in the presence of hydrogen. It generates heat which helps sustain endothermal pyrolysis reactions taking place in greater atmospheric pressures (50-200 atm) with the aim of producing higher quality bio-oil, mostly by deoxygenation of fatty acids such as pentadecanoic acid and palmitic acid (Resende, 2016). In general, hydro-pyrolysis is the same as fast pyrolysis with a difference in the attendance of hydrogen in the reactor. The presence of hydrogen in the atmosphere removes oxygen in the form of water by shifting the reaction pathway from decarbonylation and decarboxylation to dehydration (Gamliel et al., 2018). The range of the operating parameters for pyrolysis processes is summarized in Table 2.1.

Table 2.1. The range of main operating parameters for pyrolysis processes (Zaker et al., 2019).

| | Temperature (°C) | Heating rate (°C/s) | Residence time (s) | Particle size (mm) | Pressure (MPa) |
|-----------------|------------------|---------------------|--------------------|--------------------|----------------|
| Slow pyrolysis | 300–700 | 0.1-1 | 300-550 | 5–50 | 0.1 |
| Fast pyrolysis | 550–1250 | 10–300 | 0.5–20 | <1 | 0.1 |
| Flash pyrolysis | 800–1300 | >1000 | <0.5 | <0.2 | 0.1 |
| Vacuum | 300–600 | 0.1–1.0 | 0.001–1.0 | n/a | 0.01–0.02 |
| Intermediate | 500–650 | 1.0–10 | 0.5–20 | 1–5 | 0.1 |
| Hydro | 350–600 | 10–300 | >15 | n/a | 5–20 |

n/a Data not available.

The two main phases of pyrolysis are the primary and secondary phases. In the first phase, the organic molecules are decomposed or depolymerized by heat into their main components (for instance, carboxyl, carbonyl and hydroxyl groups). The primary phase includes the dehydration, decarboxylation and dehydrogenation of the organic matter. Next, the secondary stage, thermal

cracking, takes place, breaking long chains of hydrocarbons into smaller ones. The longer the residence time of the vapors in the heating zone, the more gases, such as methane, carbon monoxide and carbon dioxide, are produced.

2.3. Kinetic study of sewage sludge

A study on the kinetic behavior of SS is essential to examine the thermo-degradation rates of SS and the generation rates of products during the pyrolysis. The information derived from the mathematical kinetic modeling can provide valuable information to optimize the process (Hu et al., 2018). The TGA and derivative thermogravimetric (DTG) profiles obtained from the TGA can be studied for a better understanding of mechanism and reaction chemistry associated with pyrolysis of SS (Dai et al., 2015). The resulted curves depict the rates of mass loss during the thermal decomposition of SS samples; accordingly, they can be correlated to the kinetics of these reactions. Based on various investigations (Hameed et al., 2018; Hernández et al., 2017; Ji et al., 2010; Naqvi et al., 2019), decomposition of different components in SS has three stages. The first stage starts with release of moisture and light components in the range of ambient temperature to $\sim 150^{\circ}\text{C}$. The second stage can occur at temperatures from ~ 200 to $\sim 600^{\circ}\text{C}$, during which organic materials (biodegradable or non-biodegradable) devolatilize simultaneously. This stage is named the active pyrolysis zone due to excessive mass loss. In the active zone, protein, polysaccharides, carboxylic acid, silicates and non-biodegradable organic materials discharge from sewage sludge under heating. The inorganic material from the SS decomposes at temperatures above $\sim 600^{\circ}\text{C}$. The Arrhenius correlation, distribution activation energy model (DAEM), Coats-Redfern's method, Kissinger–Akhira–Sunose (KAS), Flynn-Wall-Ozawa (FWO) and Starink methods are some examples of the mathematical models to determine the kinetics of SS pyrolysis (Hameed et al., 2018; Lin et al., 2016; Liu et al., 2015). In these models, activation energy (E , kJ/mol) and pre-exponential factor (A , s^{-1}) are determined, and a high correlation coefficient (R^2) along with other analyses exhibit the suitable model for the description of SS pyrolysis kinetics. Table 2.2 gives representative studies on kinetic parameters of different models for SS pyrolysis.

Table 2.2. Representative kinetic parameters of different models for the pyrolysis of SS.

| Model | Reaction order | Activation energy (kJ/mol) | Pre-exponential factor (s ⁻¹) | Correlation coefficient (R ²) | Ref. |
|-------------------|----------------|----------------------------|---|---|-----------------------|
| Coats and Redfern | 1 | 11.50 | 3.43 | 0.99 | (Hameed et al., 2018) |
| | 2 | 37.02 | 3.53 | 0.99 | |
| | 3 | 51.06 | 6.66 | 0.99 | |
| DAEM | 1 | 428.00 | n/a | 0.97 | (Liu et al., 2015) |
| Coats and Redfern | 2 | 29.81 | 15.15 | 0.99 | (Shao et al., 2008) |
| KAS | - | 257.00 | n/a | 0.95 | (Lin et al., 2016) |
| Starink | - | 257.10 | n/a | | |
| Coats and Redfern | 1 | 27.40 | 3.44 | 0.97 | (Naqvi et al., 2019) |
| | 1.5 | 0.04 | 3.44 | 0.97 | |

n/a Data not available.

Recent investigations indicate that the pyrolysis of SS has great potential to solve the SS problem compared to other methods such as incineration or gasification (Samolada and Zabaniotou, 2014). This is due to pyrolysis zero-waste method, volume reduction of up to 90% and marketable products.

2.4. Pyrolysis: a potential route for sewage sludge valorization

Since 1986, several investigations have been carried out by researchers for SS pyrolysis as a potential route for obtaining the pyrolysis oil and chemicals (Fonts et al., 2012). Studies based on the lignocellulosic biomass pyrolysis have been used as baseline references for investigations into the valorization of SS. However, it's important to outline that the differences in chemical composition especially the high amount of ash in SS involves considerable alter in the chemical and physical properties of the products obtained with each feedstock. The operation parameters play a crucial role in pyrolysis. In this aspect, different studies have been conducted regarding the optimization of the operating parameters. Several researchers have studied the effect of final temperature of pyrolysis on product yields.

An early study carried out by Shen and Zhang (Shen and Zhang, 2005) investigated the influence of temperature and retention time to identify optimum process conditions for maximizing

the oil yield in two stages rotary kiln reactor. Experiments were performed between 400 and 550 °C and solid retention time of 20 to 60 min. Maximum pyrolysis oil was obtained at the highest temperature and lowest retention time. Another study examined the effect of final temperatures of 350, 450, 550 and 950 °C in a fixed bed reactor (Sánchez et al., 2009). The results indicated that by increase of temperature the valorization was promoted as the yields of condensable and non-condensable gases increased, whereas the solid residue decreased. The highest portion of liquid was obtained at 450 °C, however, gas yield reached a maximum at 950 °C. Product yields of SS regarding reaction temperature were examined by flash pyrolysis in a conical spouted bed reactor (Alvarez et al., 2015a). The results revealed that the liquid yield increased with the increase of temperature and reached a maximum of 500 °C. However, temperatures higher than 500 °C favored secondary reactions of volatiles and thermal cracking, leading to the reduction of liquid yield and a rise in the gas portion. From these studies, it can be concluded that temperature plays a critical role in the portion of products. The disparity between the value of final temperature reported by different authors should be attributed to differences in the reactor configuration and the origin of the SS, particularly have different ash content and composition. Moreover, the β influence (5 and 60 °C/min) has been investigated on product portions of SS pyrolysis in a horizontal quartz reactor (M. Inguanzo, A. Dominguez, J.A. Mene´ndez , C.G. Blanco, 2002). The investigations lead to the outcome that a higher β value can enhance the liquid and gas yield while decreasing the solid residue. Similarly, the effect of β via TGA has shown the same conclusion by release of higher mass-loss rates and lower amount of residue left after the process (Kan et al., 2016). The particle size as another vital factor affecting the yield of liquid products has been explored (Park et al., 2010). A range of 0.2<p<0.8 mm has been announced to be the optimum range to maximize the bio-oil portion. The interpretation is due to the differences in the rates of intraparticle mass and heat transfer resulting in slow heat up for larger particles and overheating for small particles (Syed-Hassan et al., 2017). All in all, the mentioned operation variables are the most influential, and in order to maximize the liquid yield, it is indispensable to explore the optimum.

From the viewpoint of bio-oil quality, pyrolysis operating conditions also influence composition. A study was carried out in order the determine the effect of temperature on the distribution of the liquid product formed from the fast pyrolysis of SS in a drop tube quartz reactor. The thermal decomposition process was performed at a prescribed temperature between 400 and

700 °C (Huang et al., 2014). The bio-oils obtained at low temperatures are species such as alkenes, alkanes, long-chain fatty acids and esters, and aliphatic nitriles and amides. At high temperatures, aliphatic and thermally labile oxygen-contained compounds were mainly cracked to gaseous products, while the nitrogen-contained species tended to form aromatic species, chiefly N-heterocyclic ones. The authors stated that due to high nitrogen content, utilization of bio-oil is not applicable because of problems related to NO_x emissions when the oil is combusted. The alike examination was also conducted in a pyrolysis centrifuge reactor regarding influence of the pyrolysis temperature on properties of the sludge oils (Trinh et al., 2013). The water-insoluble portion, molecular-weight distribution, high heating value (HHV, MJ/kg), and thermal behaviors of bio-oils were observed to be noticeably influenced by the applied pyrolysis temperatures. The optimal temperature was at 575 °C where an HHV of 25.5 MJ/kg was stated. Bio-oil derived from the screw pyrolysis of SS was carried out at temperatures between 350 and 500 °C (Tomasi Morgano et al., 2018). With the increase of temperature C/H and the C/O ratios increase while the C/N decreases. That is reflected in a slightly increasing heating value from 28.0 MJ/kg at 350 °C to 30.2 MJ/kg at 500 °C. The direct application of the bio-oil was mentioned to be hindered because of the high percentage of nitrogen, sulfur and oxygen.

2.5. Co-pyrolysis of sewage sludge

To enhance the quality and yield of products from the pyrolysis of SS, blending other co-reactants to the SS via co-processing has drawn attention. The co-pyrolysis of SS and lignocellulosic biomass has been conducted in a conical spouted bed reactor at 500 °C with a 1:1 blend ratio (Alvarez et al., 2015b). As a result of the synergetic effects, it was reported that the bio-oil and bio-char yield decreased while bio-gas increased compared to the theoretical average values. From the prospect of bio-oil composition, higher oxygenated compounds were observed in the mixture by almost 8% as compared to SS-derived bio-oil. Meanwhile, the nitrogen-containing compounds have dropped by approximately 4% and sulfur content has vanished and remained in bio-char. The feasibility of the co-pyrolysis of SS and digested manure with a blend ratio of 1:1 was performed at 525 °C in a stirred batch reactor (Ruiz-Gómez et al., 2017). The product yields did not show noticeable synergistic effects except for the yields of organic compounds, being slightly higher than the predicted average. Furthermore, the oxygen content had

increased in the organic phase resulting in a decrease in the heating value. SS was pyrolyzed with 40% mixed wood, 40% rapeseed and 40% straw to investigate the impact of co-pyrolysis on the liquid phase in terms of composition at 450 °C (Samanya et al., 2012). In all mixtures, oxygen content had enhanced while nitrogen and sulfur species had dropped. In this context, a negative impact was observed in terms of HHV by a decrease in the value. Table 2.3 summarizes the findings of the existing literature on the use of different biomasses as a co-reactant with SS in co-pyrolysis.

Table 2.3. Summary of co-pyrolysis of SS with different co-reactants.

| Co-reactant categories | Reaction conditions | | | Results | | | Ref. |
|------------------------|-------------------------|------------|--------------------------------|--------------------|------------------------------|---|---------------------------|
| | SS to co-reactant ratio | Temp. (°C) | Reactor | H/C _{eff} | Pyrolytic liquid yield (wt%) | Pyrolytic liquid characteristic, calorific value (MJ kg ⁻¹) and oxygen-nitrogen content (wt%) | |
| Pinewood sawdust | 1:1 | 500 | Conical spouted bed | ~0.21 | 55 | O = 48.59 N = 9.40 | (Alvarez et al., 2015b) |
| Manure | 1:1 | 525 | Stirred batch reactor | ~0 | ~40 | HHV= 29.40 O=19 N=6.90 | (Ruiz-Gómez et al., 2017) |
| Wood | | | | ~0.01 | 40.9 | HHV= 31.30 O= 17.80 N= 1.70 | |
| Rapeseed | 60:40 | 450 | Cylindrical shaped quartz tube | ~0.96 | 33.2 | HHV= 34.80 O=19.50 N= 4.60 | (Samanya et al., 2012) |
| Straw | | | | ~0 | 27.8 | HHV=32.50 O=30.90 N=4.20 | |

Investigation regarding thermal behavior and kinetics have also been examined via TGA by researchers to study the feasibility of co-pyrolysis from the standpoint of synergy and E value. Wang et al. studied the interaction between SS and wheat straw (Wang et al., 2016). The results revealed a weak synergetic effect based on the mass-loss rates of the TGA test, however, the co-pyrolysis in the fixed bed pyrolyzer had greatly promoted the liquid and gas phase production. This phenomenon was interpreted due to the presence of metals in the ash which promoted secondary reactions such as cracking and dehydrogenation. Another study was carried out by

mixing SS and pine sawdust with different blend ratios to observe the coupling effects (Zhu et al., 2015). Although the release of volatile matter was accelerated by the increase of rice straw, no obvious occurrence of the synergistic activities during the decomposition was observed. This means each component of the mixture had act individually. Seemingly, the same behavior was announced when SS was blended with rice straw (Huang et al., 2015). He and coworkers have pointed out the synergistic effect tendency of SS and 3 different ranked coals (He et al., 2020). Devolatilization was reported to be unfavorable during the process for all various blending ratios, while char formation was facilitated (Hu et al., 2018). In another study, thermal decomposition characteristics of co-pyrolysis of SS and hazelnut shell was (Xu et al., 2017; Zhao et al., 2018). The devolatilization rates were divided into two ranges of temperatures, 260 to 400 °C and 400 to 900 °C. In the first range, the effect of co-pyrolysis was inhibitive due to the poor thermal conductivity of hazelnut shell in the blends. The interaction in the second range was reported accelerative caused by formation of free radicals promoting the contact chance between the raw materials. Table 2.4 is a summary of research available upon literature for the amount of E value, computed with different kinetic models, required for the co-pyrolysis of SS with different types of co-reactants. From energy-saving point of view, reaction with greater E value necessities higher reaction temperature or longer reaction time, which means higher energy is required to be inputted to the thermal process.

Table 2.4. Kinetic model and activation energy for co-pyrolysis of SS with various co-reactants.

| Co-reactant | Blend ratio | Kinetic study method | Temperature range (°C)/ Conversion degree (α) | Activation energy of SS (kJ/mol) | Activation energy of blend (kJ/mol) | Ref. |
|-------------------------------|--------------------|----------------------|--|----------------------------------|-------------------------------------|-----------------------|
| Sugar Cane Bagasse | 1:1 | Coats-Redfern method | 200-400 | ~68 | 73.46 | (Hameed et al., 2018) |
| | | | 400-600 | ~27 | 20.27 | |
| Hazelnut shell | Hazelnut 30%/SS70% | FWO-KAS-Starink | 0.2-0.4 | n/a | 123.99–174.07 | (Zhao et al., 2018) |
| | | Coats-Redfern method | 0.5-0.8 | n/a | 202.07–608.15 | |
| Oil shale | 1:1 | KAS | 0.2-0.8 | 257.00 | 243.00 | (Lin et al., 2016) |
| | | Starink | average | 257.10 | 243.20 | |
| Hongshaquan coal | | | | | 180.30 | |
| Shuicheng lignite | 1:1 | DAEM | n/a | 168.40 | 179.80 | (He et al., 2020) |
| Shaerhu coal | | | | | 184.10 | |
| Activated wind turbine blades | 1:1 | Coats-Redfern method | 300-600 | 53 | 35.42 | (Hu et al., 2018) |
| Pine sawdust | 1:1 | DAEM | 0.05-0.95 | 147.98 | 148.05 | (Zhu et al., 2015) |
| | | Friedman | average | 151.39 | 152.39 | |

2.6. Catalytic pyrolysis of sewage sludge

Although a tremendous number of catalytic pyrolysis studies have been carried out to upgrade the bio-oil derived from biomass (Morgan et al., 2017), still catalytic pyrolysis of SS remains scarce in the literature. The effect of metal oxides (Al_2O_3 , CaO , Fe_2O_3 , TiO_2 , and ZnO) was explored by means of TGA to check the pyrolysis behavior for SS (Shao et al., 2010). The presence of Fe_2O_3 and ZnO was reported to inhibit the mass loss rate of devolatilization, while Al_2O_3 , CaO , and TiO_2 stimulated the degradation of organic matters to form fewer solid residues. On the other hand, Al_2O_3 and TiO_2 had decreased pyrolysis time, counter wise, CaO , Fe_2O_3 , and ZnO had prolonged. The presence of catalysts had diverse effects on the degradation process and no clear conclusion was made. Azura et al. explored the influence of a catalytic post-treatment of

pyrolysis vapors using gamma-alumina (γ -Al₂O₃) as a catalyst in a bubbling fluidized bed reactor (Azuara et al., 2015). Perfections in bio-oil properties such as HHV, chemical composition, etc. by a minor decrease in the yield was observed. The improvements in the bio-oil were attributed to a reduction in the portion of oxygen-containing compounds. However, the problem of high nitrogen-containing compounds in the liquid remained.

There are evidence that zeolite catalysts can be employed for deoxygenation and denitrogenation of lignocellulosic biomass, proteinaceous feedstocks and municipal solid wastes in pyrolysis (Liu et al., 2016). Nonetheless, research on pyrolysis of SS with the assist of zeolite catalyst is limited. An early study was performed to evaluate the effect of zeolite as a potential catalyst to enhance the production of bio-oil (Kim and Parker, 2008). The incorporation of zeolite into the sludge matrix did not show any improvement in the liquid yield and no information was provided in terms of bio-oil composition. Commercial HZSM5 was examined in a tandem micro-reactor system with aim of producing higher value chemicals (Wang et al., 2017). The results indicated that catalyst temperature has a crucial influence on composition. For instance, the carbon yield of olefins increased from 12.90% to 26.31% as catalysis temperature increased from 400 °C to 700 °C, before decreasing to 21.08% at 800 °C and aromatics portion topped at catalysis temperature of 600 °C. Different portions of HZSM5 to SS were investigated in a microwave-assisted pyrolysis system to upgrade the bio-oil quality (Xie et al., 2014). The authors pointed that the temperature had a great effect on both quality and quantity of bio-oil and 550 °C was noticed as optimum. Moreover, higher ratios of catalysts had higher removal of oxygen-nitrogen-containing compounds. The reduction in the oxygen-containing compounds was due to aromatization reactions which transformed carbohydrates to benzene. Liu et al. carried out catalytic pyrolysis over HZSM5 in a tandem microfurnace pyrolyzer (Liu et al., 2016). The catalyst had better performance at higher temperatures to enhance the deoxygenation process and promoted the formation of hydrocarbons. The explanation was due to the formation of smaller volatile molecules at higher temperatures that can travel through catalyst pores.

2.7. Production of sludge-derived AC for different applications

One of the pioneering topics is the reuse of pyrolyzed sludge as a value-added adsorbent for the removal of contaminants from wastewater streams and soil (Hadi et al., 2015). Application

of such low-price solid waste for remediation processes has a dual ecological prominence, the transformation of SS to char which tackles the disposal issues while it can remove pollutants from the environment. Moreover, in the past few years, char derived from biomasses have been used in catalysis reactions due to their morphology and porosity. However, char without activation exhibits very poor catalytic properties (Lee et al., 2017). Hence, many pieces of research have been directed to modify char morphology and porosity via various treatments and used commercial types (Dong et al., 2015). Zhang et al. have examined the use of corn stover-derived activated carbon catalyst with phosphoric acid activation for waste plastic pyrolysis (Zhang et al., 2018a). The result showed jet fuel-ranged alkanes and aromatic production were favored by using activated carbon. Another recent study has used rice husk for the production of Fe modified activated carbon for catalytic pyrolysis of corn cob for bio-oil production (Dai et al., 2019). The modified catalyst indicated selectivity to value-added products such as phenol and cresol. Similarly, a char-supported metal catalyst derived from rice husk was prepared for reforming bio-oil quality (Guo et al., 2018). Results indicated that when the vapors from biomass pyrolysis passed through metallic supported char, the selectivity and the relative contents of phenol and 4-methyl-phenol increased. However, to the best of our knowledge, few studies have focused on the catalytic performance of sludge-derived AC. The AC derived from SS pyrolysis seems a practical choice for catalytic purposes because it is easy to generate, widely available and essentially inexpensive (Gao et al., 2020). Notably, metal species are dispersed in the sludge-based char matrix inherently which can enhance the catalytic performance without the toxic and expensive synthesis procedures.

Moreover, the development of porous materials, named sorbent, with hydrophobicity and oleophobicity properties has gained interest. The created functional architectures can serve as efficient sorbents for the remediation of spilled oils or leakage chemicals. The mentioned properties allow the sorbent to be wetted by oils only. Seemingly, the open-cell texture provides efficient channels and spaces for oil diffusion and enrichment. In this regard, recently much effort has been devoted to developing advanced porous sorbents mostly from artificial synthetic materials (Saleem et al., 2018). However, these sorbents exhibit poor hydrophobicity, hence, surface modification with toxic chemicals (e.g., 1H,1H,2H,2H-perfluorooctyltriethoxysilan) to enhance the oil-wettability and hydrophobicity have been carried out (Li et al., 2014). On the other hand, magnetic sorbents, for easy recovery and reuse of the materials from oil/water mixtures,

have been synthesized mostly by co-precipitation which is an environmentally hazardous method (Karzar Jeddi et al., 2019; Shokry et al., 2020). Therefore, the use of natural-based chars produced via pyrolysis of biomasses has also been tested as oil adsorbents. The main drawback of these types of sorbents for oil spill treatment is that they absorb water quickly and sink when applied to bodies of water (Zhu et al., 2019). To overcome this challenge, decoration with a toxic chemical, lauric acid, has been examined which is detrimental to the marine ecosystem (Navarathna et al., 2020).

2.8. Summary of the literature review

Study on the development of pyrolysis technology is still ongoing. The investigations have been conducted for enriching the theoretical groundwork of co-feeding of SS with different carbon-based materials in co-pyrolysis applications. However, the studies are limited to a few and the co-reactants that were blended with SS did not show considerable synergic effect due to different decomposition temperature regimes. It is important to mention the co-reactants that were employed for the joint valorization with SS were not generated locally and/or limited to seasonal supplies making the process impracticable. Furthermore, most of the feedstocks investigated with SS in co-pyrolysis exhibited an extreme lack of hydrogen which from the perspective of bio-oil yield and selectivity (e.g., olefins and aromatic hydrocarbons) is a drawback.

A difference of SS with other types of biomasses is the presence of nitrogen and sulfur that usually ends up in condensable and non-condensable products of valorization. As for pyrolysis gas, is mainly composed of H_2 , CH_4 , CO and CO_2 and contains air pollutants, such as HCN , NO_2 , SO_2 and CH_3SH . These harmful gaseous can downgrade the pyrolysis gas quality and lead to environmental problems, enhancing additional energy and types of equipment for further treatment. Nevertheless, little research has been devoted to the investigation of these pyrolytic gaseous from the process. Thus, it is vital to figure out a beneficial procedure that can eliminate and mitigate these compounds from the aspects of harmful gaseous while enhancing energy conversion efficiencies. In addition, the bio-oil derived from SS contains a high percentage of oxygen and nitrogen species, limiting the application of these fuels. To date, contradiction studies have shown improvements by applying HZSM5. However, it is to be mentioned that these studies mainly focused on commercial catalysts to upgrade the pyrolytic vapors from SS pyrolysis which

the cost of them is a big question here and are still miles away from their final implementation. Interestingly, the solid product derived from the pyrolysis of biomass had the potential to be employed as a catalyst in the preliminary steps of research. However, auxiliary activation and metal-modification were carried out to attain higher surface area and dispersion of active sites for greater catalytic efficiency for reforming the pyrolytic vapors.

Seemingly, creation of a recyclable, cost-effective, sustainable and scalable sorbent with good uptake capacity is a challenging task, because the high-performance sorbents are facing some critical defects, such as eco-unfriendliness and complex synthesis procedures and issues in large-scale production and applications. In general, an efficient sorbent should possess oleophilic character along with other favorable properties such as high rate of sorption capacity, high selectivity towards oil, good buoyancy, easy recovery, sufficient reusability and non-toxicity. Therefore, facile and environmentally friendly alternative strategies for massive production from renewable resource is of critical importance to alleviate environmental pollution.

CHAPTER 3

EXPERIMENTAL SECTION

3.1. SS preparation and characterization

SS was obtained from Montreal WWTP, Jean-R. Marcotte, in Quebec, Canada. It was collected from the clarifiers which are a mixture of sludge decanted at the bottom and the scum from the top of the clarifier. After in situ mechanical dewatering at the site, the dewatered sludge cakes with a surface moisture content of approximately 68% were collected for the experiment. The initial pH of SS was 6.21. SS sample was dried at 105 °C in an oven for 24 h to reduce the surface moisture content to less than 10%. According to the literature, the best p value for decomposition of volatile matter from SS mainly for high β values is in the range of $0.2 < p < 0.8$ mm (Naqvi et al., 2018). The elucidation is to assure that the experiments would be conducted in the kinetic regime, eliminating mass and heat transfer effects on the results due to the low thermal conductivity of SS (Bridgwater, 2012; Sfakiotakis and Vamvuka, 2018). In this case, the dried SS was pulverized and sieved into a fine powder with $p = 0.5$ mm; then, sealed in air-tight bags and stored in the fridge.

Basic physicochemical characteristics of SS was determined by proximate and ultimate analyzes. In the proximate analysis, moisture, ash, volatiles and fixed carbon were measured using ASTM (D1762-84) standard methods. The ultimate analysis was conducted using a CHNS/O elemental analyzer (ThermoFischer Scientific Flash 2000). The HHV is the amount of energy stored in the material. In order to avoid expensive and inaccurate experimental procedures, an appropriate model established to date was employed to compute HHV as described (Nhuchhen and Abdul Salam, 2012). According to the elemental analysis, the simplified chemical formula of the SS that derives can be written as $(CH_{1.732}N_{0.073}S_{0.0058}O_{0.52})_n$. The element composition was analyzed by ICP-OES (Agilent Technologies 5100, USA). The proximate and ultimate analysis were conducted thrice to prevent sampling errors of the raw materials and the average values are displayed in Table 3.1.

Table 3.1. Main characteristics of SS.

| Sample | Proximate analysis (wt.%) | | | Ultimate analysis (wt.%) ^a | | | | | H/C _{eff} | HHV (MJ/kg) |
|---|---------------------------|------------------|-----------------------------|---------------------------------------|-------|------|------|-------|--------------------|-------------|
| | Volatil e ^a | Ash ^a | Fixed carbon _{a,b} | C | H | N | S | O | | |
| SS | 56.50 | 41 | 2.50 | 28.89 | 4.20 | 2.48 | 0.45 | 20.39 | 0.40 | 13.05 |
| Elemental analysis (mg/kg) ^a | | | | | | | | | | |
| K | P | Ca | Mg | Al | Fe | As | Cd | Co | Cr | Cu |
| 4600 | 14400 | 63800 | 7220 | 26300 | 24800 | 7.50 | 5.67 | 45.90 | 44.70 | 338 |
| Hg | Mn | Mo | Ni | Pb | Se | Zn | Ba | | | |
| 0.26 | 212 | 5.02 | 33.50 | 54.80 | 26.30 | 458 | 208 | | | |

^a Dry basis.^b By difference.

3.2. Thermogravimetric (TGA) evaluation

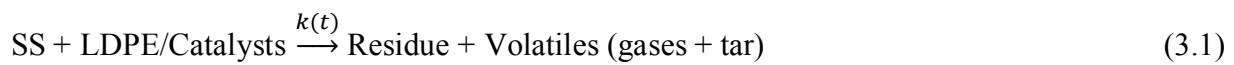
Pyrolysis, co-pyrolysis and catalytic pyrolysis experiments were performed in a TGA instrument (TA-Q500). A blank run was performed with an empty crucible before running each sample under identical conditions to reduce the effect of buoyancy and achieve a stable baseline (He et al., 2020). Sample masses were kept below 5 mg to avoid heat and mass transfer at high β and subsequently loaded in the TGA crucible. Samples were then heated upto 1000 °C at a constant β . To maintain an inert atmosphere with a low-noise TGA signal, it was important to purge argon with a uniform flow. Thus, a constant argon flow of 100 ml/min was set in all experiments. The apparatus is linked to a computer for data logging and the thermal analysis was performed using the TRIOS[®] software. The uncertainty related to the experimental measurement of the parameters has been provided in Table 3.2. Accordingly, the accuracy of the TGA instrument is high both for the measurement of mass and for temperature control. It is justified that the uncertainties are negligible for the kinetic plots in this study. In addition, to ensure the reproducibility and repeatability of the data; triplicate TGA tests were performed. The maximum variation in the conversion rate (α) from sample to sample of the same materials was 0.02 and their mean value was presented in the outcomes.

Table 3.2. Different apparatuses employed during experimental procedure and uncertainty in measurement of the parameters.

| Variable/analysis | Apparatus used | Uncertainty |
|---|--|-------------|
| Primary drying of SS (°C) | Laboratory hot air oven | ±3 |
| Weighing apparatus (g) | Sartorius analytical balance (RK-11955-22) | ±0.0001 |
| Proximate analysis (°C) | Thermo Scientific™ Box Furnaces | ±1 |
| Argon flow rate (mL/min) | Mass flow controller (Fisherbrand™) | ±0.20 |
| Temperature (°C) | TA-Q500 | ±1 |
| Weighing Precision (%) | TA-Q500 | ±0.01 |
| Sensitivity in the mass Measurements (µg) | TA-Q500 | 0.1 |
| Heating Rate (°C/min) | TA-Q500 | ±0.01 |

3.3. Kinetic theory

Kinetic modeling of heterogeneous solid materials during the co-pyrolysis of SS and LDPE was adapted in order to analyze the behavior of the solid-state in a wide range of experimental conditions. In fact, providing an in-depth understanding of the reactions occurring during co-pyrolysis is crucial in determining the role of different constituents (Raza et al., 2019). In general, it is difficult to predict the possible reaction mechanism of SS pyrolysis. However, the general kinetic equation of heterogeneous solid-state thermal transformation in a linear temperature β can be described as follows (Zaker et al., 2019):



The primary goal of pyrolysis and co-pyrolysis kinetic modeling is to calculate the kinetic parameters using mathematical models, E value, A value and the reaction mechanism, $f(\alpha)$, which may involve other parameters, such as the reaction order (n). All kinetic analyses go through the Arrhenius law; provide information about the rate of reaction. The rate of non-isothermal solid decomposition equation is as follows (Özsin and Pütün, 2017):

$$\frac{d\alpha}{dt} = k(T)f(\alpha) = A \exp\left(\frac{-E}{RT}\right) (1 - \alpha)^n \quad (3.2)$$

where T is the reaction temperature (K), k is the rate constant; A is the pre-exponential factor (s^{-1}), E is the activation energy (kJ/mol), and R is the gas constant ($0.008314 \text{ kJ mol}^{-1}\text{K}^{-1}$). $f(\alpha)$ is differential form of the kinetic mechanism and usually is expressed as $(1-\alpha)^n$, where, n is the reaction order and α is a dimensionless measurement of the amount of reactants that have been converted into products defined as follows :

$$\alpha = \text{conversion rate} = \frac{W_0 - W_t}{W_0 - W_f} \quad (3.3)$$

where, W_0 (mg) is the first-stage sampling weight, W_f (mg) is the weight at the end of reaction and W_t is the weight at time (t).

Eq. (3.2) is the basic formulation for computing the kinetic parameters based on the TGA data. Herein, Coats–Redfern (Salema et al., 2019), KAS, FWO and Starink methods were applied to determine the E value. Due to the feasible procedure for estimation of E value and good adaptability and validity, iso-conversional approaches are recommended by International Confederation for Thermal Analysis and Calorimetry (ICTAC) (Zhao et al., 2018). It's worth to mention that the non-isothermal or dynamic TGA method is most often selected over the isothermal TGA since fewer data are required to determine the reaction kinetics.

3.4. Pyrolyzer system design

To date, various reactor types have been applied for the pyrolysis of SS (Mastral et al., 2015; Trinh et al., 2013; Yu et al., 2016; Zhang et al., 2011; J. Zhang et al., 2017b). Interestingly, fix-bed reactors are of particular interest owing to their ease of use, large loading capacity and the high contact between the co-reactants and/or catalyst, etc. (Zhang et al., 2019). Although it may face poor heat transfer in large-scale pyrolysis systems, overall it is a suitable and cost-effective option for laboratory experiments and has been widely utilized by researchers in the field (Gunasee et al., 2017; Hu et al., 2017; Wang et al., 2016). Herein, a horizontal fixed-bed reactor (700 mm length and 25 mm O.D) sealed with two flange end caps was specifically designed and implemented. The furnace (Lindberg/Blue M Mini-Mite™ Tube Furnaces, Thermo Scientific) was heated electrically, and the temperature was measured using an internal thermocouple. A control program was used to manage dwell time, final temperatures and β value. A schematic diagram of the fixed-bed pyrolysis system is shown in Fig. 3.1.

For the bio-oil experiments, approximately 3 g of sample (dry basis) was added into a ceramic boat (Fisherbrand™ Porcelain Combustion Boats) which was then placed inside the furnace with a continuous flow of high-purity nitrogen through the reactor (0.5 L/min) before each experiment for 20 min. A flow meter (Riteflow® Panel/Bench Mounted Flowmeters) was used to control the gas flow of nitrogen. The RT of pyrolytic vapors inside the horizontal reactor was assessed from the following equation (Gunasee et al., 2017):

$$\text{Residence Time (RT)} = \frac{V}{Q} \quad (3.4)$$

where, V is the volume of the reactor in the heating zone (V, 14.72 10⁻⁵ m³) and the Q is the volumetric flow rate of the nitrogen gas (Q, 8.33 10⁻⁶ m³/s). The computed residence time is approximately 17 s. The temperature of the furnace was elevated to a pre-set temperature with a specific β, and nitrogen gas was purged throughout the reactor to direct the pyrolysis vapors towards the condensers. The exit tube from the reactor was connected to a condensation sequence through a short connection tube to avoid condensation of the hot pyrolytic volatiles before reaching the condensers. The condensation sequence was consisting of two vacuum traps (Synthware™ Vacuum Trap with Hose Connection on Side and Top) immersed in a water-ice bath containing dichloromethane (DCM) to collect the liquid product. The non-condensable portion of pyrolysis gas was collected as the biogas in Tedler sample gas bag. The product yields of char and the pyrolytic liquid were obtained by applying Eq. 3.5. The yield of the gas product was calculated from the difference in the char and pyrolytic liquid (Zheng et al., 2018).

$$\text{Products yield (\%)} = \left[\frac{\text{Mass of product fraction}}{\text{Mass of raw SS}} \right] \times 100 \quad (3.5)$$

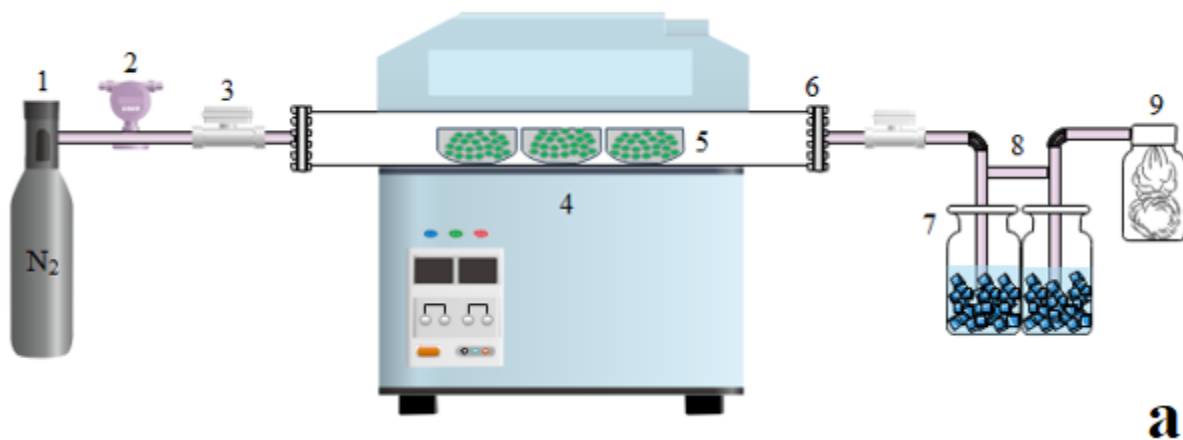


Fig. 3.1. Lab-scale horizontal fixed bed pyrolysis reactor system: a) Schematic diagram: (1) Nitrogen cylinder, (2) Flow meter, (3) Valve, (4) Furnace, (5) Crucible containing sample, (6) Quartz tube with flanges on both sides, (7) Ice bath, (8) Vacuum trap, (9) Gas bag; b) digital photo.

3.4.1. Optimization of pyrolyzer set-up

In order to get the highest portion of bio-oil yield, pyrolysis of SS was conducted in the built pyrolyzer setup to optimize the final temperature based on the TGA results and literature

survey (Dai et al., 2014; H. Zhang et al., 2017; Zielińska et al., 2015). For this purpose, four different target final temperatures (450, 500, 550 and 600 °C) with a dwell time of 60 min and $\beta=30$ °C/min were tested. Owing to the heterogeneity of the SS, it is crucial to launch the product yields after multiple experiments (Suriapparao et al., 2018a). Fig. 3.2 shows different portions of char, pyrolytic liquid and bio-gas based on the average of triplicate experiments at different temperatures. The experiment outcomes indicated a decrease of the char portion with the increase of temperature due to progressive pyrolysis conversion (Huang et al., 2014). The yield of bio-oil amplified with the change of temperature and reached a maximum at 550 °C, then the liquid portion decreased as temperature increased. This phenomenon was in an agreement with the previous study (F. Huang et al., 2018). The drop in bio-oil portion above 550 °C can be explained due to secondary reactions such as thermal cracking of the volatile compounds (Xie et al., 2014). Correspondingly, the increase of bio-gas yield at higher temperatures can be attributed to this phenomenon.

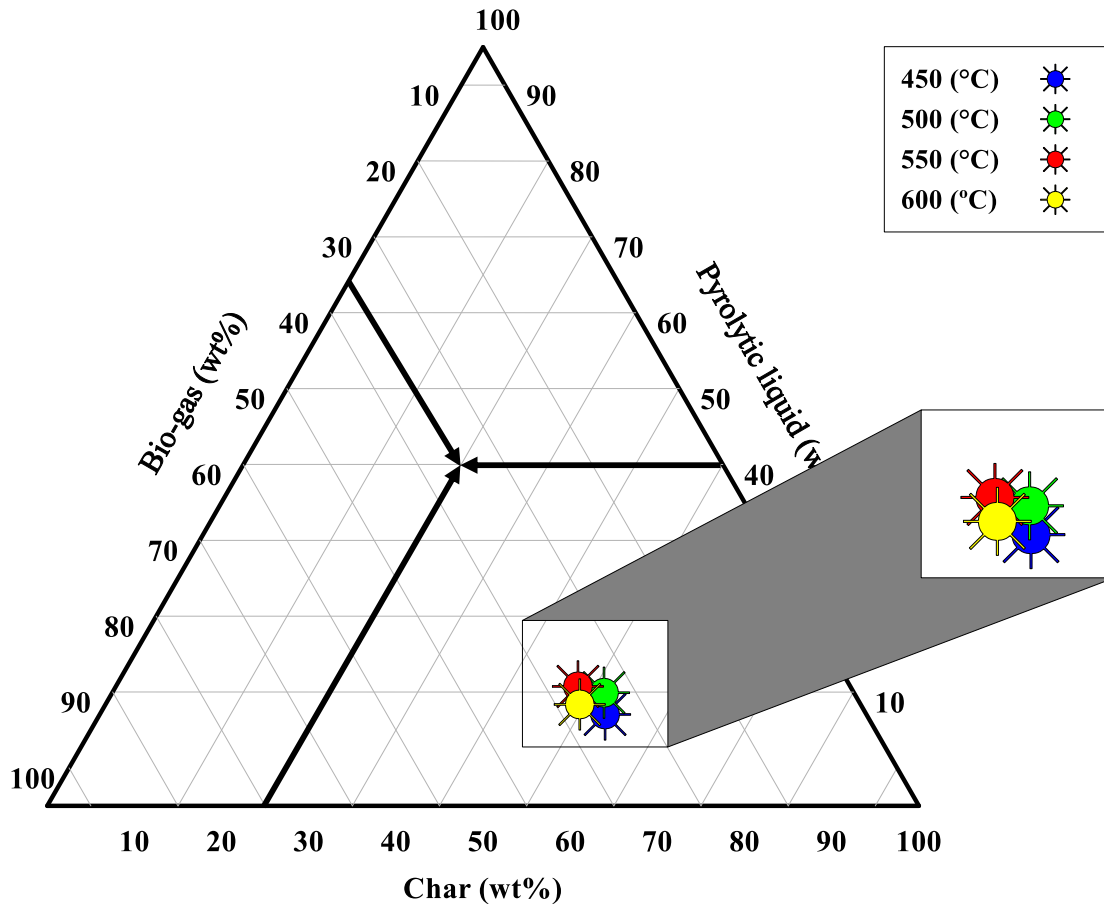


Fig. 3.2. Effect of final temperature on product distribution from pyrolysis of SS.

The chemical composition of the pyrolysis and catalytic pyrolysis bio-oil was analyzed using gas chromatography/mass spectrometry (GC/MS) (Agilent 7890) with a HP-5 MS capillary column. Helium was used as the carrier gas at a flow rate of 1.2 mL/min. The injection size was 1 μ L with a split ratio of 1:10. The oven temperature was 40 °C initially held for 3 min and then increased to 290 °C at a β of 5 °C/min, and held at 290 °C for 5 min. The temperatures of the injector and detector were maintained at 250 and 230 °C, respectively. The pyrolytic liquid was filtered and diluted 5 times with DCM (HPLC grade, 99.8%, Alfa Aesar, USA). The compounds were identified by comparing their mass spectra with those from the National Institute of Standards and Technology (NIST) mass spectral data library. A semi-quantitative method was used to determine the relative proportion of each compound in the liquid by calculating the chromatographic area percentage.

3.5. AC preparation and characterization

Dried SS was homogeneously blended with NaOH pellets in a 1:1 ratio. The blend was placed in a crucible (Fisherbrand™ Porcelain Combustion Boats) and carbonized in a tubular reactor (Lindberg/Blue M Mini-Mite™ Tube Furnaces, Thermo Scientific) at 700 °C with a β of 10 °C/min lasting for 120 min with N₂ as carrier gas at 0.5 L/min. At the end of the reaction, the nitrogen atmosphere was maintained until reaching the ambient temperature and then the AC was collected and sealed away in the desiccator. The obtained AC was washed with 2M HCl for 4 h, and subsequently by cold and hot deionized water of 60 °C for 2 h until reaching neutral pH. The synthetic AC was oven-dried at 105 °C for 24 h.

The thermal stability of the AC catalyst was analyzed by the TGA instrument (TA-Q500) using an argon atmosphere with β = 10 °C/min, from ambient temperature to 1000 °C. The morphology of AC was analyzed using an FEI Quanta 450 scanning electron microscopy (SEM) (Thermo Fisher Scientific, USA), operating at 25 kV and equipped with an Everhart-Thornley secondary electron detector. Energy-dispersive X-ray spectroscopy (EDX) was employed for the elemental composition analysis using FEI Quanta 450 SEM equipped with an INCA microanalytical system (Oxford Instruments, UK). The surface area was measured from N₂ isotherms at -196.15 °C using a gas sorption analyzer (NOVA-1200; Quantachrome Corp., USA). The sample was degassed for 12 h under the inert condition at 200 °C before applying adsorption

measurements. The N_2 adsorbed per gram of samples schemed versus the relative vapor pressure (P/P_0) of N_2 , and the data were fitted to the Brunauer-Emmett-Teller (BET) equation to compute surface area. Fourier Transform Infrared (FT-IR) spectroscopy (Thermo Scientific, 4700) was employed to evaluate the functional groups of AC. The infrared spectra were collected in a range of $4000-500\text{ cm}^{-1}$ with a resolution of 8 cm^{-1} . All analyses were carried out in triplicate.

CHAPTER 4

CO-PYROLYSIS OF SEWAGE SLUDGE AND LOW-DENSITY POLYETHYLENE: A THERMOGRAVIMETRIC STUDY OF THERMO-KINETICS AND THERMODYNAMIC PARAMETERS

4.1. Introduction

SS generation has considerably increased in recent years due to the hasty expansion of municipalities and industries. SS annual production in US was expected to approach 10 million tons (dry base) by 2020 (Lin et al., 2019). Recently, SS has been considered as a potential renewable energy resource for substitution of fossil fuels (Syed-Hassan et al., 2017). On the other hand, demand for fossil fuel hydrocarbons such as plastics has led to an annual production of 300 million tons of new plastic material which is added to the existing plastic (Xiang et al., 2018b). This is problematic, as the plastics are non-degradable and can last for centuries in the environment. In general, there are two main procedures for dealing with SS and plastic waste: incineration and landfilling. However, these options are time-consuming and suffer from various drawbacks and limitations (e.g. production of greenhouse gases and restrictive environmental regulations) (Chen et al., 2019). Thus, it's an urgent need for alternative technology that can simultaneously overcome these restrictions and recycle the wastes into valuable products.

Increasing attention has been paid to pyrolysis as a low energy-intensive and environmentally friendly procedure with dominance over biological processes due to higher efficiency (Ahmad et al., 2017b; Shao et al., 2010). Pyrolysis is esteemed as one of the reliable practices to convert waste to renewable energy which is carried out in an inert atmosphere at elevated temperatures (400~600 °C) along with bio-oil production as a source of energy, bio-char and bio-gases as value-added products (Zaker et al., 2019). To optimize the process parameters and maximize desired products, knowledge about the reactivity and kinetic mechanism is very critical for guidance and control of thermal conversion and the design of large-scale pyrolysis reactors (Azizi et al., 2017). Nevertheless, obtaining adequate data of kinetic rate constants that can be used for heterogeneous materials (e.g., agricultural residue and SS) and for different β is very challenging due to an enormous number of reactions and the differences in compositions of the main compounds. TGA has helped to understand the pyrolysis behavior of heterogeneous

reactions involved in such complex processes (Mehmood et al., 2017). Moreover, it provides information about mathematical modeling simplification. The most critical steps to analyze TGA data are model-fitting and model-free (iso-conversion) methods.

SS co-pyrolysis with biomass has gained attention as an important strategy for solid waste management (Salema et al., 2019). The mechanism is similar to pyrolysis with a second feedstock mixed with SS in the process. The benefits can be pointed out as cost-effective, environmentally friendly and highly efficient technology. Generally, most SS feedstocks are hydrogen deficient, which has opposing impacts on hydrocarbon production from the pyrolysis. The effective hydrogen index (EHI) (Eq. 4.1) reflects hydrogen content of various biomass samples. EHI is an indicator of hydrogen/carbon ratio after debiting the compound's hydrogen content for complete conversion of heteroatoms to NH_3 , H_2S and H_2O , which is expressed as the following equation (Xie et al., 2015),

$$\text{EHI} = (\text{H} - 2\text{O} - 3\text{N} - 2\text{S}) / \text{C} \quad (4.1)$$

Where H, C, O, N and S are the number of moles of hydrogen, carbon, oxygen, nitrogen and sulfur in the feedstock, respectively. In this context, addition of other feedstocks with appropriate EHI value to the SS via co-pyrolysis is a versatile approach (Gao et al., 2020). Moreover, the mixing ratio in co-pyrolysis is a vital parameter to understand the synergistic effects. Several synergistic effects can happen during the co-feeding of SS and a feedstock that has a high EHI value to accelerate the release of volatile matter and lower the E value (Huang et al., 2015; Jin et al., 2016). Decreasing the E value will cut down the energy consumption of the process with the proper mixing ratio (Lin et al., 2016).

TGA has been used to investigate the co-pyrolysis kinetics of SS and several kinds of feedstocks including woody biomass (Samanya et al., 2012), pine sawdust (Zhu et al., 2015), lignocellulosic biomass (Alvarez et al., 2015b), oil shale (Lin et al., 2016), digested manure (Ruiz-Gómez et al., 2017), hazelnut shell (Zhao et al., 2018), rice husk (Raza et al., 2019) and bagasse (Hameed et al., 2018; Lin et al., 2019). These studies agree on the differentiation of different split ratios of SS and the feedstocks that influence the kinetic parameters. However, these feedstocks had a low $\text{EHI} < 1$ value and results revealed weak synergetic effects based on the mass-loss rates

meaning each component of the mixture acts as alone. In addition, the mentioned co-reactants were limited to regional and seasonal variations.

Typically, plastics are rich with hydrogen compounds (EHI= ~2) making them a potential cost-effective option when co-fed with SS and are abundantly available (Li et al., 2013). More than 40% of the plastic production belongs to packaging sector which approximately 50% is in the form of LDPE (Patil et al., 2018). Under this context, the benefits of employing a co-reactant such as LDPE in the co-feeding process could be a feasible approach that can simultaneously tackle the problematic issue related to the increase of waste in the environment and has a beneficial effect on SS conversion (Xiang et al., 2018b).

Co-pyrolysis of biomass-LDPE has proven positive synergistic interaction by decreasing the E value and modifying reaction mechanism of oxygen removal to enhance the quality of bio-oil (Zhang et al., 2016a; Zheng et al., 2018). Although several kinds of research have been carried out on co-feeding of biomass and plastics (Lu et al., 2018; Xiang et al., 2018b; Zhang et al., 2016c), there have been no investigations on co-pyrolysis of SS and plastics. The challenges of SS and plastic waste management and increasing energy demand can instantaneously be investigated by co-pyrolysis. It is vital to address the detailed characterization of materials together with TGA analysis to expand the information about the thermal conversion applications of various blends of SS/LDPE samples and gain insight into the different β values influence. To the best of our knowledge and based on the literature survey, this study aims to present for the first time the co-pyrolysis of SS/LDPE blends through a TGA approach. This paper includes studies of the co-pyrolysis by a combined consideration of multi β and different blending ratios and evaluates the synergistic effect in terms of kinetics (model-fitting and model-free methods) and process thermodynamics. The data obtained in this study will provide referral information for biofuel generation from SS/LDPE co-pyrolysis.

4.2. Material and methods

4.2.1. Materials

Dried SS pulverized and sieved into a fine powder with p value of 500 μm . LDPE powder with p value of 500 μm was purchased from Alfa Aesar Co, LTD. Basic physico-chemical characteristics of LDPE was determined by proximate and ultimate analyzes. According to the

elemental analysis, the simplified chemical formula of the LDPE is $(CH_2CH_2)_n$. The Main characteristics of LDPE are given in Table 4.1.

Table 4.1. Main characteristics of SS and LDPE.

| Sample | Proximate analysis (wt.%) | | | Ultimate analysis (wt.%) ^a | | | | | EHI | HHV (MJ/kg) |
|--------|---------------------------|------------------|-----------------------------|---------------------------------------|------|---|---|---|-----|----------------|
| | Volatile ^a | Ash ^a | Fixed carbon ^{a,b} | C | H | N | S | O | | |
| LDPE | 100 | - | - | 86.5 | 13.5 | - | - | - | 1.9 | 34.7 |

^a Dry basis.

^b By difference.

4.2.2. Pyrolysis and co-pyrolysis using TGA

Pyrolysis and co-pyrolysis experiments of SS, LDPE and their blends were performed in a TGA instrument. Experiments were conducted into two sets. The first set consists of SS/LDPE blended in different ratios. Samples containing 25%, 50% and 75% mass percentage of LDPE were nominated SL-25, SL-50 and SL-75, respectively. Samples mass were kept below 5 mg with a maximum deviation of ± 0.3 mg in order to avoid heat and mass transfer influence at high β and were loaded in the TGA crucible and heated from 30 to 1000 °C at a constant β of 30 °C/min. The second pyrolysis experiment was that the mixed SL-50 was raised from 30 to 1000 °C at different β of 10, 20, 30 and 40 °C/min, respectively. It was intended to examine the effect of different β values considered in the thermal behavior and estimation of the kinetic parameters for the whole decomposition temperature range.

To determine the discharge act of volatile components, a comprehensive index $D(D_i)$ (Eqs. 4.2-4.4) was employed as a principle for pyrolysis and co-pyrolysis release characteristics (He et al., 2019).

$$D_i = \frac{DTG_{\max} DTG_{\text{mean}} W_{\infty}}{T_i T_{\max} \Delta T_{1/2}} \quad (4.2)$$

$$\Delta T_{1/2} = \frac{T_f - T_i}{2} \quad (4.3)$$

$$D = \sum D_i \quad (4.4)$$

where, DTG_{max} and DTG_{mean} indicate maximum and mean decomposition rate obtained from DTG results (%/min), respectively. T_i is the initial devolatilization temperature ($^{\circ}C$), T_{max} is the maximum mass loss temperature ($^{\circ}C$); $\Delta T_{1/2}$ ($^{\circ}C$) indicates the temperature related to the temperature range of pyrolysis and W_{∞} is weight loss (%) in the total weight loss. D_i is the index of each peak for multiple phases of the thermal decomposition, representing the activeness of devolatilization property.

4.2.3. Assessment of synergistic effects

In order to estimate the coupling synergistic effect between the co-reactants, the calculated curves of these blends are the sum of the weight of parent components by their portion at that temperature (Yao et al., 2017). The calculated TGA/DTG curves are obtained using Eqs. (4.5) and (4.6) (Garba et al., 2018):

$$TGA_{cal} = x_{SS}TGA_{SS} + x_{LDPE}TGA_{LDPE} \quad (4.5)$$

$$DTG_{cal} = x_{SS}DTG_{SS} + x_{LDPE}DTG_{LDPE} \quad (4.6)$$

where, TGA_{SS} and TGA_{LDPE} are the weight loss rate of pure SS and LDPE, x_{SS} and x_{LDPE} are the weight fraction of each reactant in the mixture, and DTG_{SS} and DTG_{LDPE} are the thermal decomposition rate of materials during pyrolysis under the same operational conditions (Zheng et al., 2018). To further discuss the extent of the interactions during co-pyrolysis, the root mean square error (RMSE) values of the deviation between experimental TGA/DTG_e curves and calculated TGA/DTG_c curves was defined as (Wu et al., 2016):

$$RMSE = \sqrt{\frac{1}{n}[\sum_{i=1}^n (TGA/DTG_e - TGA/DTG_c)^2]} \quad (4.7)$$

4.2.4. Kinetic approaches

4.2.4.1. Model-fitting method

Coats-Redfern model is often applied for determination of E value, A and n (El-Sayed and Mostafa, 2015; Mishra and Mohanty, 2018). Rearranging Eq. (3.2) and integrating both sides followed by logarithm of the obtained equation for a constant pyrolysis heating rate ($\beta=dT/dt$) leads to:

$$\ln \left[-\frac{\ln(1-\alpha)}{T^2} \right] = \ln \left[\frac{AR}{\beta E} \left(1 - \frac{2RT}{E} \right) \right] - \frac{E}{RT} \quad (n=1) \quad (4.8)$$

and,

$$\ln \left[-\frac{1-(1-\alpha)^{1-n}}{T^2(1-n)} \right] = \ln \left[\frac{AR}{\beta E} \left(1 - \frac{2RT}{E} \right) \right] - \frac{E}{RT} \quad (n \neq 1) \quad (4.9)$$

As $\exp(-(E/RT)) \approx 0$, Eq. (4.8 & 4.9) can be simplified as,

$$\ln \left[-\frac{\ln(1-\alpha)}{T^2} \right] = \ln \left[\frac{AR}{\beta E} \right] - \frac{E}{RT} \quad (n=1) \quad (4.10)$$

and,

$$\ln \left[-\frac{1-(1-\alpha)^{1-n}}{T^2(1-n)} \right] = \ln \left[\frac{AR}{\beta E} \right] - \frac{E}{RT} \quad (n \neq 1) \quad (4.11)$$

This equation can be written as a straight line ($Y=mX+b$), where $\ln \left[-\frac{\ln(1-\alpha)}{T^2} \right]$ and $\ln \left[-\frac{1-(1-\alpha)^{1-n}}{T^2(1-n)} \right]$ are considered Y, respectively, and $1/T$ is X for easy understanding. The value of α and T at time t could be determined from the experimental TGA/DTG data. Thus, by plotting LHS vs $1/T$, a straight line will be achieved. From the slope and intercept of the line, E and A can be determined. The criterion to attain precise and satisfactory E and A values were premised on the ultimate value of n that should concede values of E with the highest coefficient of determination, R^2 to the fitted regression line. In the first step, n was considered to be first-order reaction and later with the assist of Excel the best linear regression for reaction order was determined.

4.2.4.2. Model-free methods

This method is used to determine the E value from experimental data at a given β . In this paper, KAS, FWO and Starink methods are implemented to E value calculation based on mathematical models (Zhao et al., 2018);

$$\text{KAS method: } \ln \left(\frac{\beta}{T^2} \right) = \ln \left[\frac{AE}{Rg(\alpha)} \right] - \frac{E}{RT} \quad (4.12)$$

$$\text{FWO method: } \ln \beta = \ln \left[\frac{AE}{Rg(\alpha)} \right] - 1.0516 \frac{E}{RT} \quad (4.13)$$

$$\text{Starink method: } \ln \left(\frac{\beta}{T^{1.8}} \right) = C_s - 1.0037 \frac{E}{RT} \quad (4.14)$$

At constant value of α , the plot of $\ln(\beta)$, $\ln\left(\frac{\beta}{T^2}\right)$ and $\ln\left(\frac{\beta}{T^{1.8}}\right)$ versus $1/T$ obtained from thermograms recorded at several β help in yielding a straight line whose slope allows evaluation of the E value from the above methods, respectively.

4.2.5. Thermodynamic parameters calculation

Iso-conversional methods are often limited to estimate the A value and predict the reaction model. In order to improve this limitation, Kissinger developed a model-free non-isothermal equation (He et al., 2019):

$$A = \beta E \exp\left(\frac{E}{RT_{\max}}\right) / RT_{\max}^2 \quad (4.15)$$

Thermodynamic parameters include a change in enthalpy (ΔH , kJ/mol), gibbs free energy (ΔG , kJ/mol) and entropy (ΔS , kJ/mol.K) and can be obtained from the TGA data. These parameters can be obtained based on the kinetic data of SS, LDPE and blend of SS/LDPE from the following equations (Hameed et al., 2018; Mehmood et al., 2017; Raza et al., 2019).

$$\Delta H = E - RT \quad (4.16)$$

$$\Delta G = E + RT_{\max} \ln\left(\frac{K_B T_{\max}}{hA}\right) \quad (4.17)$$

$$\Delta S = \frac{\Delta H - \Delta G}{T_{\max}} \quad (4.18)$$

where K_B is the Boltzmann constant ($1.381 \times 10^{-23} \text{ m}^2 \text{ kg s}^{-2} \text{ K}^{-1}$), h is the Planck's constant ($6.626 \times 10^{-34} \text{ m}^2 \text{ kg s}^{-1}$), T_{\max} is the peak temperature of the DTG curve and T the temperature at the degree of conversion α .

4.3. Results and discussion

4.3.1. Thermal behavior

Pyrolysis of heterogeneous material is a complex process due to the series of reactions occurring simultaneously. Thus it is important to conceive the fundamentals of SS pyrolysis reaction chemistry to explore its potential for bioenergy and chemicals (Mehmood et al., 2017). Fig. 4.1(a and b) indicate the remaining weight (%) and its derivatives (%/min) curves. As can be seen from Fig. 4.1b., the major loss of LDPE occurring over a narrow range temperature of 414-

510 °C, and the decomposition domain was intense (Fig. 4.1a). One should note that LDPE was entirely decomposed, and no solid residue was left at the end of experiment.

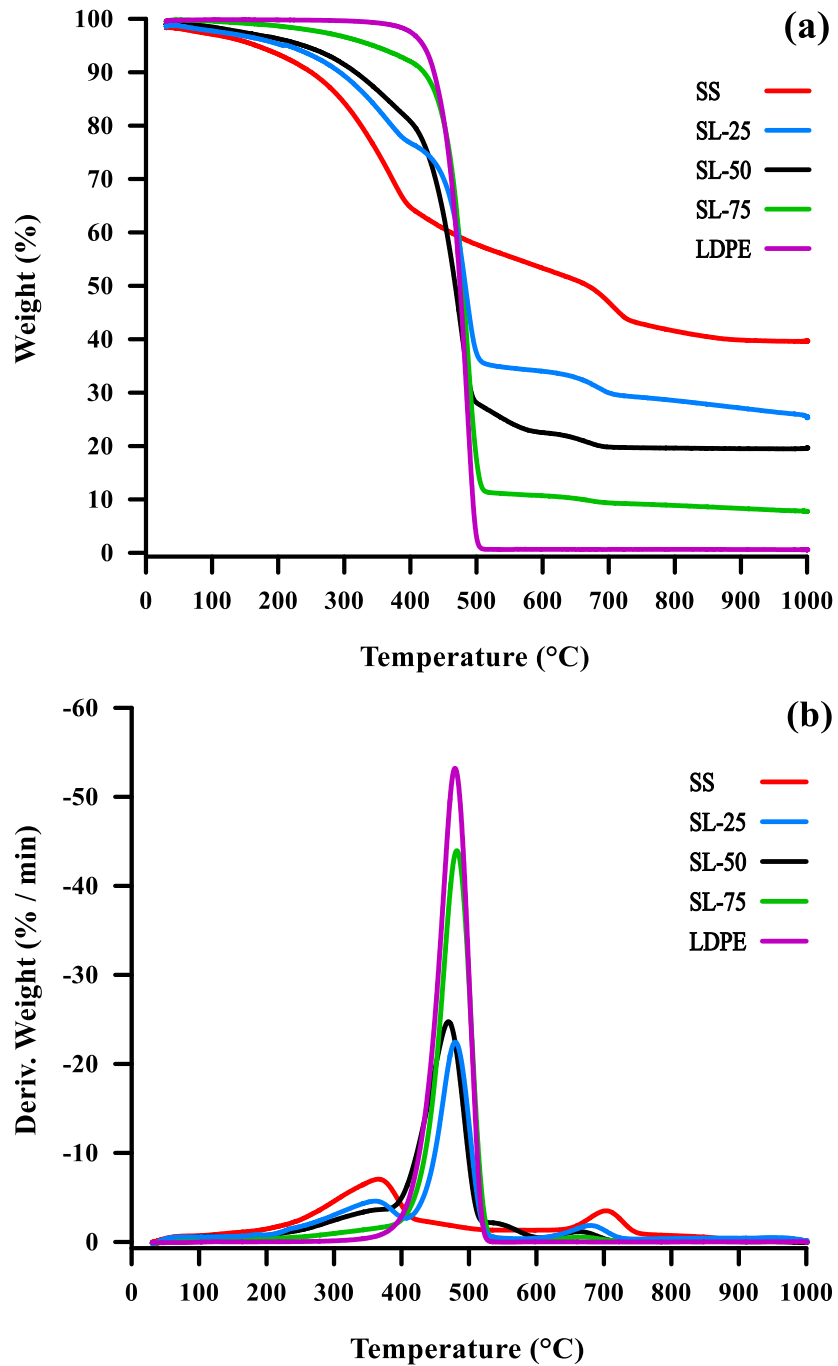


Fig. 4.1. (a) TGA and (b) DTG curves of individual SS, LDPE and their blends at $\beta=30$ °C/min.

As exhibited in Fig. 4.1(a and b), the curves of SS and LDPE have different behaviors. In fact, SS contains organics, bacteria, inorganic particles and colloids, thus, it has a complex thermal degradation process and a random distribution of volatile matters (Zhao et al., 2018). As a result, SS pyrolysis occurred in three stages with two phases during stage two. The first stage started from ambient temperature until ~ 200 °C, where the mass loss was recorded at 8% of the initial sample. The moisture content of less than 10% is considered a suitable sample for pyrolysis since higher values decrease the heating value (Ahmad et al., 2017b). The mass loss was attributed to the dehydration and the decomposition of the bonded hydrated compounds along with some light volatiles (Kan et al., 2016). The main decomposition occurred after dehydration and raised sharply above ~ 200 °C. It reached $T_{\max} \sim 360$ °C and then ceased at ~ 600 °C. It is an active pyrolysis stage where the major mass loss of 40% is observed. The shape of the DTG curve showed that the active pyrolysis zone can be sub-divided into two phases. In the first phase, the depolymerization of biodegradable materials phase from 200-400 °C, where biodegradable materials are released by bond breaking and forming reactions, corresponding to a mass loss of $\sim 28\%$. During this phase, the most reactive organic components (e.g., lipids, polysaccharides and silicates) and organic polymers (e.g., hemicellulose and cellulose) decomposed (Syed-Hassan et al., 2017). While SS is a complicated material with an enormous number of compounds, many of their decomposition temperature regions overlap. Thus, the second phase, 400-600 °C, illustrated a wide flat shape with a mass loss of $\sim 11\%$. This phase is allocated to the second degradation of less reactive and large molecular weight components (e.g., proteins, carboxyl group, bacterial matter and etc.) (Folgueras et al., 2013; Kan et al., 2016). Liu et al. have classified the active pyrolysis zone as the main stage for the crack of C-C bond, C-O bond, aromatic rings and oxygen-functional groups with nitrogen for the generation of volatiles (Liu et al., 2015). The third stage starts after 600 °C and it is accompanied by a mass loss rate of $\sim 14\%$ and by the decomposition of inorganic substances. The peak that appeared between 650-725 °C is mainly attributed to calcium carbonate (CaCO_3) and microcline decomposition. Similar behavior has also been pointed out by other researchers (Folgueras et al., 2013). The final residue of SS was 40% and it can be deduced that the conversion of LDPE was easier than SS at the same temperature rates while resulting in greater amounts of solid residue for SS pyrolysis.

Fig. 4.1(a and b) also displays the TGA/DTG curves of the SS/LDPE blends. The trends for all three blends were different from their raw materials. Nearly total decomposition of

SS/LDPE mixture takes place in the active pyrolysis zone. According to a previous study (Garba et al., 2018), LDPE softens below 300 °C before coating on the SS surface. This coat would prevent the escape of volatile substances. As the temperature increase, the particles of coated LDPE may act as a bridge over SS leading to a promotion in the heat transfer to the SS during thermal decomposition, hence enhancing the diffusion of the volatile matter in the blends. Lin et al. have mentioned the difficulty in identifying specific macromolecular composition due to asymmetrical shape of DTG peaks, implying that several substances may decompose together at almost the same temperature range (Lin et al., 2019). Based on the DTG curve of the blends, there was a steep peak in temperature range of 420-520 °C for all mixtures indicating the simultaneous decomposition of LDPE and SS. It is affirmed that the mixture of SL-50 could shift the high peak of individual LDPE to a lower temperature. It can be seen that the high peak shifted to 469 °C, which is lower than that of individual LDPE. The intensity of DTG peak decreased from 53%.min⁻¹ at 479 °C to 24%.min⁻¹ at 469 °C, which meant that the DTG peaks moved towards lower temperatures with the addition of SS. A similar observation was pointed out in a previous study (Xiang et al., 2018b). Some TGA/DTG characteristic parameters of individual and mixtures are listed in Table 4.2. It can be found that the comprehensive index D increased with the increase of LDPE ratio. Index D values of the whole pyrolysis were 6.96×10^{-5} , 4.68×10^{-4} , 5.33×10^{-4} , 4.75×10^{-3} and 6.4×10^{-3} for SS, SSDPE2-1, SL-50, SL-75 and LDPE, respectively. Likewise, the mixing ratio of LDPE had a crucial impact on the co-pyrolysis behavior. The yield of char dropped gradually as the increasing LDPE mass ratio which were 25.27, 19.67 and 7.73 for SL-25, SL-50 and SL-75, respectively. This phenomenon could be ascribed to the hydrogen donation by LDPE (14%) in the reactor atmosphere during co-pyrolysis of SS/LDPE. Also, the hydrogen transfer from LDPE to SS stemmed in stabilization of primary products from SS degradation and led to an increase of volatile and loss of char yield. These results indicate that the pyrolysis performance of SS can be enhanced by addition of LDPE. Furthermore, SL-50 blend can be selected as an optimum ratio from the perspective of high index D and shifting the high peak to lower temperature.

Table 4.2. Pyrolysis and co-pyrolysis characteristic parameters for SS, LDPE and their blends at $\beta=30$ °C/min.

| Features | SS | SL-25 | SL-50 | SL-75 | LDPE |
|--|-----------------------|-----------------------|-----------------------|-----------------------|----------------------|
| T_{i1}^a (°C) | 237 | 240 | 243 | 396 | 366 |
| T_{f1}^b (°C) | 537 | 531 | 598 | 534 | 533 |
| T_{max1}^c (°C) | 366 | 479 | 469 | 482 | 479 |
| DTG_{max1}^d | 7 | 22 | 24 | 43 | 53 |
| DTG_{mean1}^e | 3.57 | 5.75 | 6.22 | 17.94 | 18.03 |
| $W_{\infty 1}^f$ (%) | 34.90 | 60.09 | 72.24 | 81.10 | 98 |
| D_{i1}^g (% ² K ⁻³ min ⁻²) | 6.70×10^{-5} | 4.68×10^{-4} | 5.33×10^{-4} | 4.75×10^{-3} | 6.4×10^{-3} |
| T_{i2}^a (°C) | 633 | 618 | 610 | - | - |
| T_{f2}^b (°C) | 756 | 731 | 716 | - | - |
| T_{max2}^c (°C) | 703 | 680 | 665 | - | - |
| DTG_{max2}^d | 3.50 | 1.84 | 1.15 | - | - |
| DTG_{mean2}^e | 2.23 | 1.15 | 0.74 | - | - |
| $W_{\infty 2}^f$ (%) | 9.15 | 4.40 | 2.65 | - | - |
| D_{i2}^g (% ² K ⁻³ min ⁻²) | 2.61×10^{-6} | 3.92×10^{-7} | 1.05×10^{-7} | - | - |
| D^g (% ² K ⁻³ min ⁻²) | 6.96×10^{-5} | 4.68×10^{-4} | 5.33×10^{-4} | 4.75×10^{-3} | 6.4×10^{-3} |
| CP ^h (%) | 39.67 | 25.27 | 19.67 | 7.73 | 0 |

^a T_{i1} , T_{i2} the initial decomposition temperature according to the peaks.

^b T_{f1} , T_{f2} the final temperature according to the peaks.

^c T_{max1} , T_{max2} the peak temperature according to the peaks.

^d DTG_{max1} , DTG_{max2} the maximum weight loss rate according to the peaks.

^e DTG_{mean1} , DTG_{mean2} the mean weight loss rate according to the peaks.

^f $W_{\infty 1}$, $W_{\infty 2}$ the weight loss percentage in the total weight loss according to the peaks.

^g D the comprehensive devolatilization index; D_1 and D_2 are the index D.

^h CP the char percentage.

β value is one of the most crucial parameters affecting the thermal decomposition characteristics (Shao et al., 2008). It also provides details about the impact of β as it affects the conversion, product distribution and gives a concept about the reactor to be utilized. TGA/DTG curves of SL-50 at $\beta=10, 20, 30$ and 40 °C/min are illustrated in Fig. 4.2(a and b). Clearly, an increase in β does not significantly affect the TGA/DTG patterns. As β increases, peaks positions moved towards higher temperatures with a continuous increase in the conversion rate, which is

usually referred to thermal hysteresis (Chen et al., 2016). This phenomenon is due to the low thermal conductivity of the SS and limitations of mass and heat transfer, which is in good agreement with other studies (Kan et al., 2016).

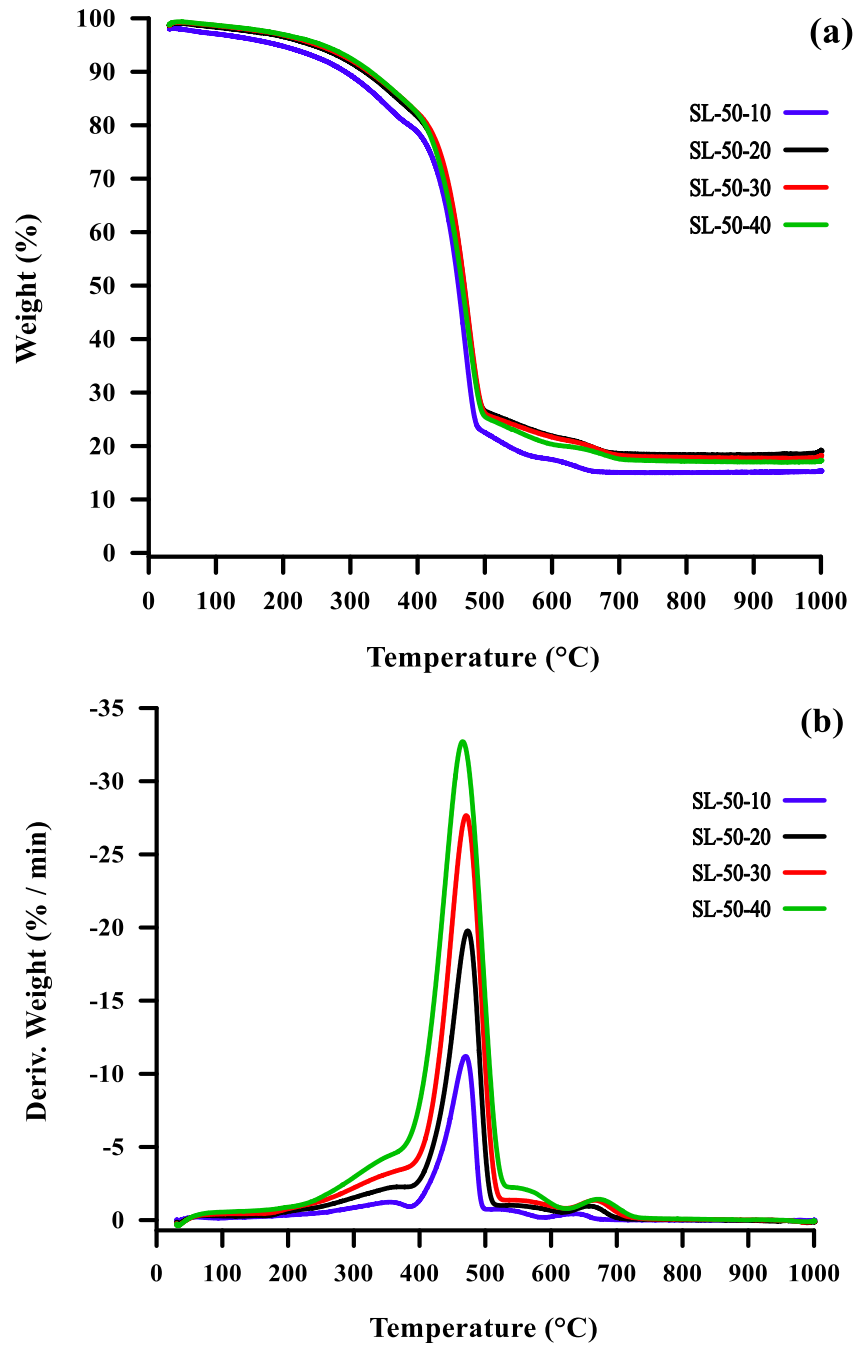


Fig. 4.2. Co-pyrolytic (a) TGA and (b) DTG curves of SL-50 at different $\beta=10, 20, 30$ and 40 $^{\circ}\text{C}/\text{min}$.

The calculated parameters of SL-50 are presented in Table 4.3 to describe the co-pyrolysis characteristics. Co-pyrolysis comprehensive devolatilization index D dramatically increased with the surge of β . The values of index D for the overall co-pyrolysis were 6.47×10^{-5} , 1.86×10^{-4} , 3.91×10^{-4} and 6.07×10^{-4} at 10, 20, 30 and 40 °C/min, respectively. These plots are also used to calculate E value by model-free and model-fitting methods.

Table 4.3. Co-pyrolysis characteristic parameters for SL-50 blend at different β .

| β (°C/min) | T_i^a (°C) | T_f^b (°C) | T_{max}^c (°C) | DTG_{max}^d | DTG_{mean}^e | W_∞^f (%) | D^g (% ² K ⁻³ min ⁻²) |
|---------------------|-----------------|-----------------|---------------------|---------------|----------------|---------------------|--|
| 10 | 292 | 669 | 469 | 11.1960 | 1.99012 | 75 | 6.47×10^{-5} |
| 20 | 309 | 701 | 473 | 19.7817 | 3.73266 | 72 | 1.86×10^{-4} |
| 30 | 316 | 709 | 470 | 27.6608 | 5.65674 | 73 | 3.91×10^{-4} |
| 40 | 319 | 722 | 465 | 32.7153 | 7.49319 | 74 | 6.07×10^{-4} |

^a T_i the initial decomposition temperature according to the peaks.

^b T_f the final temperature according to the peaks.

^c T_{max} the peak temperature according to the peaks.

^d DTG_{max} the maximum weight loss rate according to the peaks.

^e DTG_{mean} the mean weight loss rate according to the peaks.

^f W_∞ the weight loss percentage in the total weight loss.

^g D the comprehensive devolatilization index.

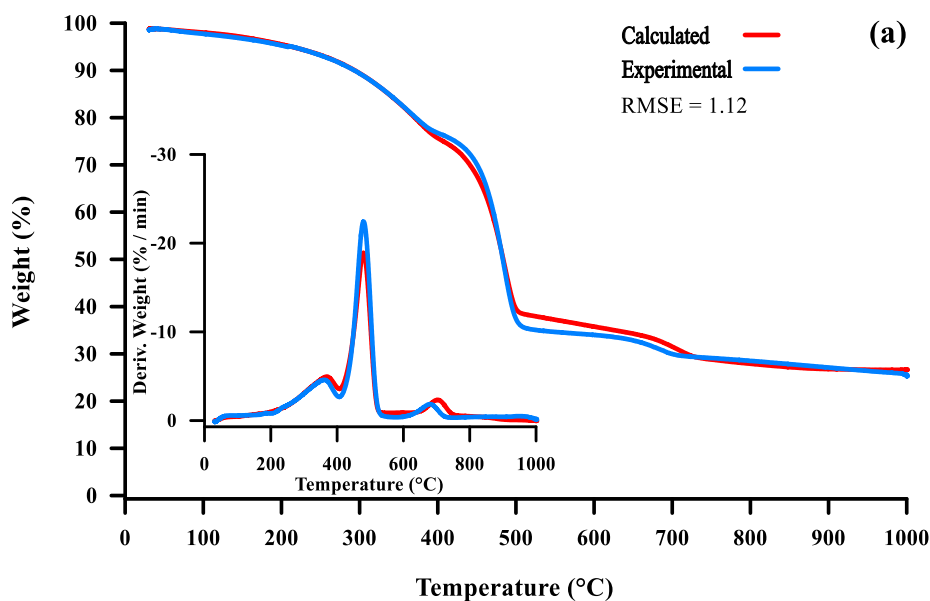
4.3.2. Evaluation of synergistic interaction

To evaluate the occurrence of interactions between SS and LDPE, experimental TGA/DTG curves of the SL-25, SL-50 and SL-75 were compared with the calculated TGA/DTG curves at $\beta=30$ °C/min (Fig. 4.3(a-c)). Obviously, the calculated and experimental weight loss rate of SL-25 follow similar devolatilization patterns. The blend did not indicate any considerable interaction between materials since the temperature corresponding to the T_{max} from DTG curve was the same. As the LDPE split ratio increased in the blends, interaction between materials was raised.

The experimentally determined weight loss values for both SL-50 and SL-75 are higher than that of the theoretical one, which indicates a synergetic interaction (Azizi et al., 2017). As aforementioned, LDPE completely decomposed at around 500 °C and it is important to note that no residue was left at the end of pyrolysis. Therefore, the synergistic effect cannot be seen in temperatures above 500 °C. In contrast to calculated results, the maximum weight loss rate of the DTG curves has increased for experimental components. Similar results were also stated by (Lu

et al., 2018). For SL-50 degradation, a positive decrease in T_{max} was observed indicating that the decomposition process has shifted towards a lower temperature when the split ratio was 1:1. This could be explained by the fact that SS pyrolysis has been accelerated by the radicals diffused from LDPE. The overlap of temperature regimes (200-600 °C) between the SS and LDPE allowed the occurrence of this interaction since the active pyrolysis zone of SS and LDPE are in the same temperature range.

Interestingly, the co-conversion of SL-50 and SL-75 lead to lower formation of char from experimental cases in comparison to the calculated cases. One explanation can be stated due to the secondary cracking of the solid residue in the presence of LDPE (Chen et al., 2016). Whilst the hydrogen transferred from the polymer structure of LDPE to the SS was related with the radicals generation. These radicals initiated the scission of synthetic polymer and accelerated polymer cracking to promote lighter hydrocarbon formation. Furthermore, hydrogen movement from polymer to SS ended in stabilization of initial products from SS decomposition and resulted in the drop of residual. It is worth mentioning that information and research about the synergetic effect between SS and LDPE are missing in the literature. One can conclude from co-conversion of cellulose and LDPE that the synergy is considerably dependent on the presence of solid-solid and solid-gas interactions where the char acts as a catalyst (Gunasee et al., 2017).



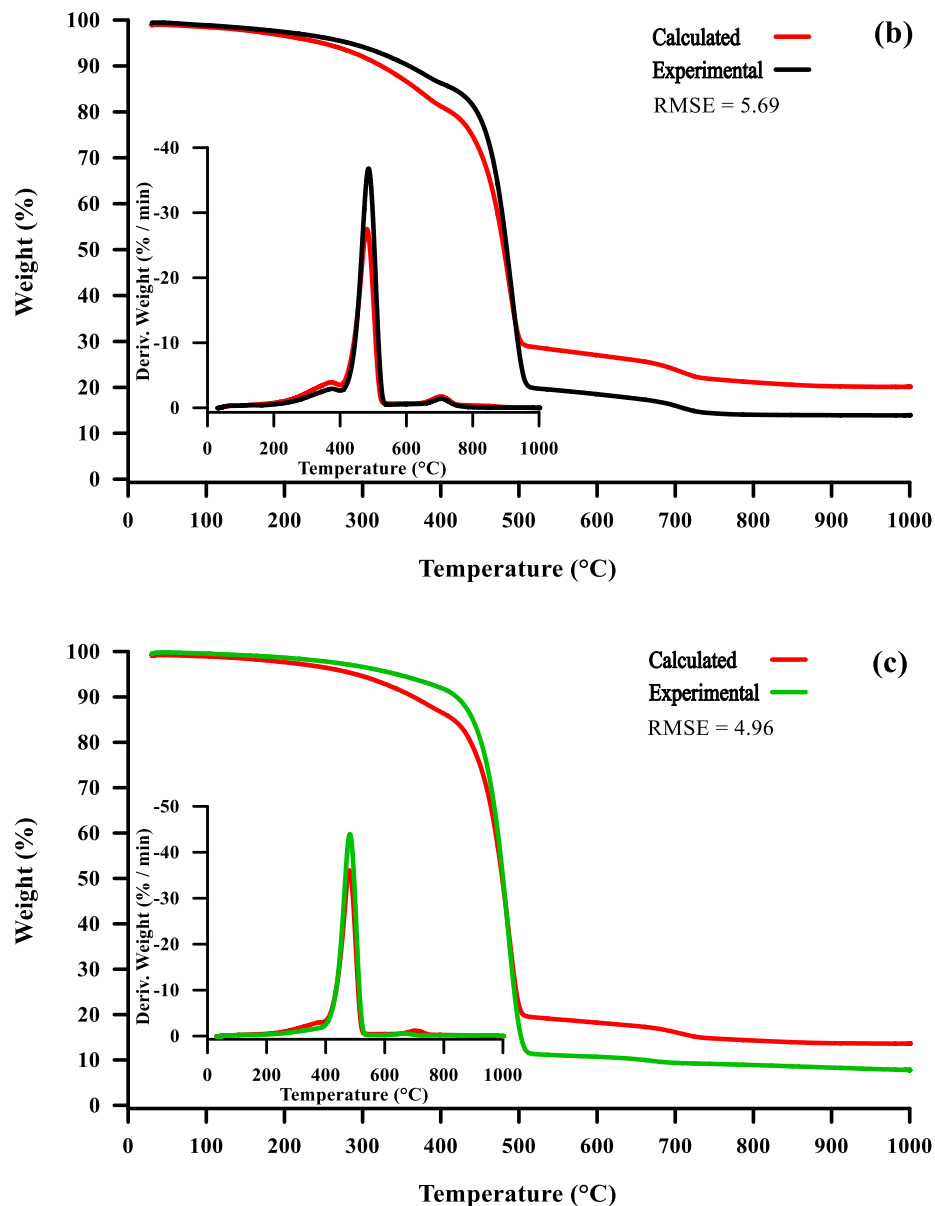


Fig. 4.3. Comparison between experimental and calculated TGA/DTG curves for the (a) SL-25, (b) SL-50 and (c) SL-75 at $\beta=30$ °C/min.

In the present study, RMSE values were 1.12, 5.69 and 4.96 for SL-25, SL-50 and SL-25, respectively. The values prove that the SL-50 had outstanding synergistic effects during the coprolysis among the other two blends, suggesting as an optimal mixture. The addition of LDPE had accelerated the decomposition process of SS when temperature passed 300 °C, resulting in lower formation of char residue. The results ascertained higher interaction between SS and LDPE

in comparison to co-pyrolysis of SS with oil shale (Lin et al., 2016), Wheat straw (Wang et al., 2016), hydrochar (Yao et al., 2017) and Sugar Cane Bagasse (Hameed et al., 2018).

4.3.3. Evaluation of model-fitting kinetic

E value is the least amount of energy required to trigger a reaction. A high value of E implies a retard reaction, whereby, E value is related to the pyrolysis reaction mechanism. This information leads to optimization of the process parameters, design and development of new pyrolysis configurations. Coats-Redfern model is based on a single β and it is widely employed to ascertain the n value (Oyedun et al., 2014; Salema et al., 2019; Yao et al., 2017).

Typical temperature ranges where the greatest percentage of volatile mass loss occurred (active zone of pyrolysis) were chosen to calculate the kinetic parameters in a single step reaction, including A factor and E value. As depicted in Table 4.4, the consecutive n-th order reactions model matched the experimental data very well ($R^2 \geq 0.9$). Reaction order was calculated using trial and error procedure by putting the various values of the n such as 0.1, 0.2, 0.3, ..., 3. The best-fitted value of the order of reaction was n=3 for SS and n=0.6 for LDPE indicating that the decomposition of SS was more complex than that of LDPE. n was found to be 1.6, 0.6 and 0.1 for co-pyrolysis of blends SL-25, SL-50 and SL-75, respectively. The relatively higher portion of SS in the mixture can increase the process complexity. The E value of individual SS at 200-700 °C was 30.01 kJ/mol lower than that of LDPE (187.40 kJ/mol) at 414-510 °C. In this case, E value for both individual SS and LDPE is in good agreement with other studies (Garba et al., 2018; Hameed et al., 2018; Naqvi et al., 2019). As presented in Table 4.4, E values for different blends of SS/LDPE samples were in the range 34.89 to 112.41 kJ/mol. E value increases with increasing the LDPE ratio in the mixture and follows the trend $SS < SL-25 < SL-50 < SL-75 < LDPE$. At the same time, it was obvious that the reactivity of the mixtures was slightly higher than that of SS and considerably lower than individual LDPE. As aforementioned, this may be attributed to the mechanism of radical interactions during the co-pyrolysis where SS components can trigger radical formation initiating the cleavage of LDPE polymer chain. This phenomenon would increase the percentage of reactant molecules per unit volume in the reactor and reduce the energy required for the reaction. A high E value means that the reaction needs more energy from the surrounding during the process. The alter of E of various mixtures amplifies that SS/LDPE blends of various compositions have different co-pyrolysis relativities. In this case, composition of SL-50 can be

selected as an optimum blend as a result of E value vicinity to SS. Results confirm the positive synergistic effect between SS and LDPE on reducing the E value. The calculated A values for the SS and LDPE pyrolysis were 0.398 and $5.060 \times 10^{10} \text{ s}^{-1}$, respectively. A factor was 0.457, 0.398 and $1.320 \times 10^5 \text{ s}^{-1}$ for SL-25, SL-50 and SL-75, respectively.

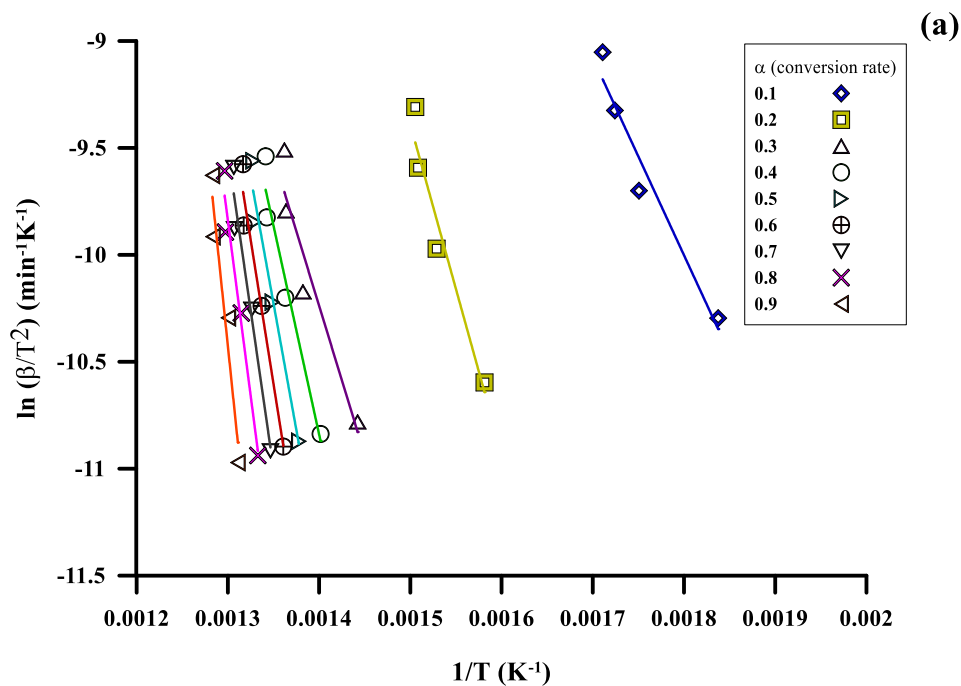
Table 4.4. Kinetic parameters for SS and LDPE pyrolysis and co-pyrolysis of their blends.

| Sample | Temperature range (°C) | Conversion (%) | E (kJ/mol) | Reaction order (n) | Pre-exponential factor (S^{-1}) | Correlation coefficient (R^2) |
|--------|------------------------|----------------|------------|--------------------|--|--|
| SS | 200-700 | 1-87 | 30.01 | 3.00 | 1.038 | 0.98 |
| SL-25 | 261-700 | 1-93 | 34.89 | 1.6 | 0.457 | 0.90 |
| SL-50 | 300-600 | 1-95 | 37.32 | 0.6 | 0.398 | 0.91 |
| SL-75 | 414-514 | 1-96 | 112.41 | 0.1 | 1.320×10^{05} | 0.98 |
| LDPE | 414-510 | 0-99 | 187.40 | 0.6 | 5.060×10^{10} | 0.99 |

4.3.4. Evaluation of model-free kinetics

As mentioned above, SS pyrolysis is a complex reaction, whose reaction dynamics and chemical kinetics are influenced by the E and A values (Mehmood et al., 2017). The model-free technique has been extensively implemented for kinetic study (Zheng et al., 2018). It can be used to obtain an accurate E value without referring to any mechanism function (Lin et al., 2019). This method is based on dependence of E value as a function of the conversion degree giving more realistic values. Three modeling approaches were proposed in this study. Linear relationships are obtained for all model-free methods. The ICTAC has indicated the use of at least four β values for iso-conversional method which can lower the uncertainties by improving sensitivity and error (Vyazovkin et al., 2014). In this case, the linear correlations for co-pyrolysis of SL-50 for KAS, FWO and Starink at $\beta=10, 20, 30$ and $40 \text{ }^\circ\text{C}/\text{min}$ were computed as shown in Fig. 4.4(a-c). The parallelism of these lines denotes a similar kinetic behavior, indicating that probably the same reaction mechanism is attained (Çepelioğullar et al., 2018). To provide an estimate, E values were calculated with selected conversion rates of $\alpha=0.1-0.9$ with a step of 0.1 according to the Eqs. (4.12-4.14). The same procedure has been applied for pure SS and LDPE materials and the results are summarized in Table 4.5. The correlation coefficient was higher than 0.9 for each model indicating that the results were credible. The average values of kinetic energy calculated from

KAS, FWO and Starink methods are 180.44 kJ/mol, 191.72 kJ/mol and 182.24 kJ/mol respectively for SS; 342.12 kJ/mol, 354.4 kJ/mol and 344.62 kJ/mol respectively for LDPE; and 200.37 kJ/mol, 212.25 kJ/mol and 202.30 kJ/mol respectively for SL-50. These results exhibited that the SL-50 considerably dropped the E value compared to pure LDPE and was slightly more than SS, which is in an intermediate value. This confirms the assumption of a positive synergistic effect between SS and LDPE on lowering E value and increasing reaction activity.



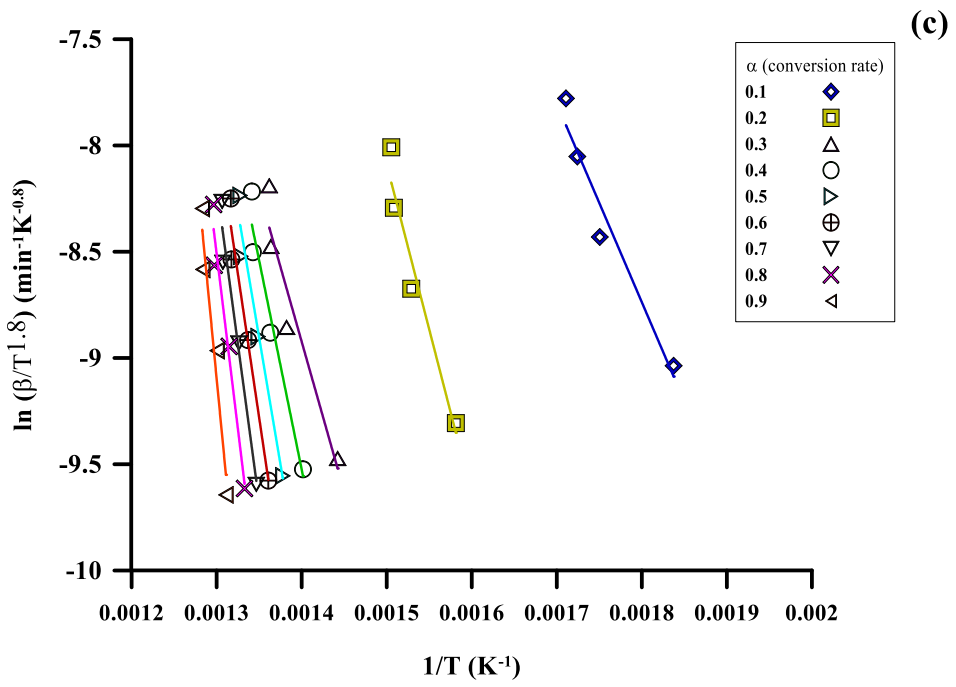
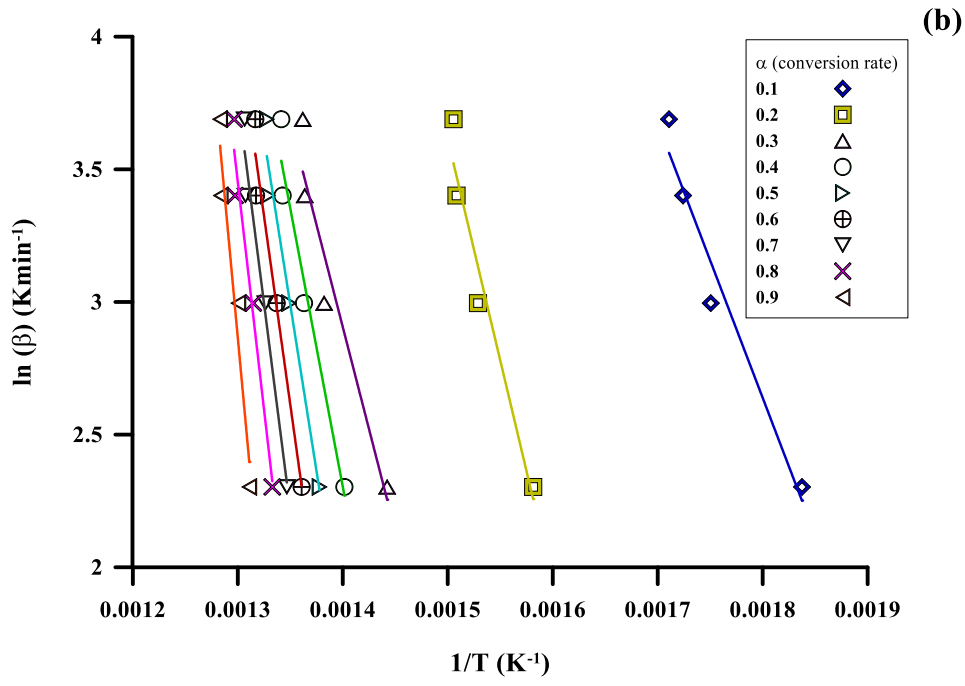


Fig. 4.4. Linear fit plots for determining E value of the SL-50. Where, $\ln(\beta/T^2)$, $\ln(\beta)$ and $\ln(\beta/T^{1.8})$ were plotted against inverse of pyrolysis temperature using KAS (a), FWO (b) and Starink (c) methods, respectively.

As shown in Table 4.5, it can be elucidated that the average R^2 value of all curves are within the small range of 0.94-0.99 indicating that the points are well agreed. The average E value computed for each method is around 3.11%, being much lower than the conventionally accepted 10% (Brachi et al., 2015). Seemingly, the E value computed from FWO method was slightly higher than the other two methods. This implies that the reaction mechanism alters in the degradation process and the E value is reliant on conversion (Naqvi et al., 2018).

Table 4.5. Activation energy (E), pre-exponential factor (A) and correlation coefficients (R^2) obtained from KAS, FWO and Starink methods for the solo-pyrolysis of SS and LDPE and co-pyrolysis of SL-50 blend.

| α | SS | | LDPE | | SL-50 | |
|----------|---------------|-------|---------------|--------|---------------|-------|
| | E (kJ/mol) | R^2 | E (kJ/mol) | R^2 | E (kJ/mol) | R^2 |
| KAS | | | | | | |
| 0.1 | 146.34 | 0.98 | 323.56 | 0.98 | 76.72 | 0.95 |
| 0.2 | 255.32 | 0.93 | 329.05 | 0.99 | 127.88 | 0.94 |
| 0.3 | 284.85 | 0.93 | 333.05 | 0.99 | 154.73 | 0.94 |
| 0.4 | 300.39 | 0.93 | 341.41 | 0.99 | 162.22 | 0.95 |
| 0.5 | 312.32 | 0.93 | 345.38 | 0.99 | 196.43 | 0.96 |
| 0.6 | 127.60 | 0.99 | 350.66 | 0.99 | 223.77 | 0.96 |
| 0.7 | 86.55 | 0.92 | 349.35 | 0.99 | 245.90 | 0.96 |
| 0.8 | 48.76 | 0.91 | 351.97 | 0.99 | 272.70 | 0.96 |
| 0.9 | 61.81 | 0.92 | 354.68 | 0.99 | 343.00 | 0.93 |
| Avg | 180.44 | 0.94 | 342.12 | 0.99 | 200.37 | 0.95 |
| FWO | | | | | | |
| 0.1 | 153.92 | 0.98 | 335.23 | 0.98 | 86.08 | 0.96 |
| 0.2 | 264.28 | 0.93 | 341.00 | 0.99 | 138.66 | 0.95 |
| 0.3 | 294.54 | 0.93 | 345.18 | 0.99 | 166.66 | 0.95 |
| 0.4 | 310.60 | 0.93 | 353.65 | 0.99 | 174.35 | 0.96 |
| 0.5 | 322.97 | 0.94 | 357.71 | 0.9972 | 208.73 | 0.96 |
| 0.6 | 139.15 | 0.99 | 363.08 | 0.9963 | 236.20 | 0.96 |
| 0.7 | 99.36 | 0.94 | 361.85 | 0.99 | 258.44 | 0.96 |
| 0.8 | 63.05 | 0.94 | 364.55 | 0.99 | 285.36 | 0.96 |
| 0.9 | 77.67 | 0.94 | 367.33 | 0.99 | 355.83 | 0.93 |
| Avg | 191.72 | 0.95 | 354.40 | 0.99 | 212.25 | 0.95 |
| Starink | | | | | | |
| 0.1 | 147.64 | 0.98 | 325.92 | 0.98 | 77.95 | 0.95 |
| 0.2 | 257.16 | 0.93 | 331.47 | 0.99 | 129.44 | 0.94 |
| 0.3 | 286.87 | 0.93 | 335.5 | 0.99 | 156.49 | 0.94 |
| 0.4 | 302.53 | 0.93 | 343.9 | 0.99 | 164.04 | 0.95 |
| 0.5 | 314.54 | 0.94 | 347.89 | 0.99 | 198.39 | 0.96 |
| 0.6 | 129.23 | 0.99 | 353.21 | 0.99 | 225.84 | 0.96 |
| 0.7 | 88.16 | 0.93 | 351.89 | 0.99 | 248.07 | 0.96 |
| 0.8 | 50.37 | 0.91 | 354.54 | 0.99 | 274.98 | 0.96 |
| 0.9 | 63.63 | 0.92 | 357.26 | 0.99 | 345.55 | 0.93 |
| Avg | 182.24 | 0.94 | 344.62 | 0.99 | 202.30 | 0.95 |

The movements of E value calculated from different kinetic free models as a function of conversion are illustrated in Fig. 4.5. E value for raw SS increased gradually until reaching 50% conversion after that, a sudden decrease is observed which continued until 90% of conversion for the three methods employed in this study. This fluctuation indicates that pyrolysis is governed by different reactions. In fact, pyrolytic degradation process of various components with very different reactivities that emerge from the difference in the chemical structure and organic nature of the constituting components represents a complex reaction mechanism. The overall mechanism involves parallel, competitive and consecutive reactions. The decreasing trend initiating from 50% conversion can be accredited to porous framework of the intermediate formed serving in the increase of non-uniformed diffusion of volatiles and undergoing decomposition with metallic components in the ash matrix (Alvarez et al., 2015a; Chanaka Udayanga et al., 2018). Therefore, the porous structure of char formed at high temperatures and the metal from ash catalyze cause the decomposition reaction and shrinking the E value. However, E value of pure LDPE barely fluctuates with the level of conversion, giving evidence of single-step reaction which is in good accordance with the findings of (Zheng et al., 2018).

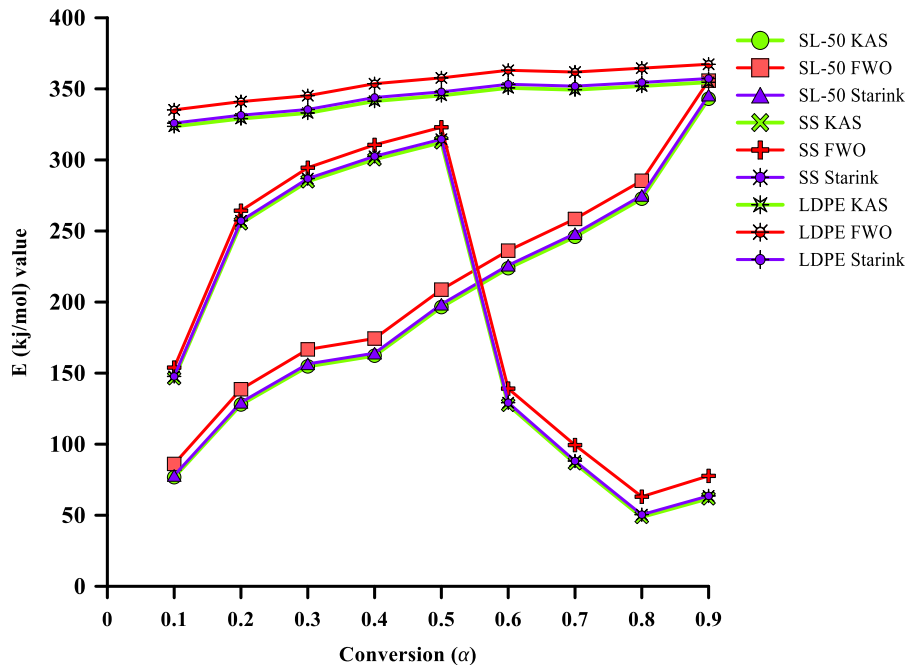


Fig. 4.5. E (kJ/mol) value as a function of conversion.

For thermal degradation of SL-50, two noticeable regions between $0.1 < \alpha \leq 0.5$ and $0.5 < \alpha < 1$ were observed. In the first region including $\alpha=0.5$, the E value was lower than both individual samples, from 50% conversion the E value was higher than SS and lower than LDPE. Consequently, the result shows that there was a positive synergy between SS and LDPE that led to lowering E value and enhancing the reactivity of the blend. The exact mechanism by which synergy between SS and LDPE causes chemical reactions during co-pyrolysis is not very clear.

4.3.5. Evaluation of thermodynamic parameters

As discussed above, E values derived from the model-free methods (Table 4.5) were employed to compute A values and thermodynamic parameters of ΔH , ΔG and ΔS for SS, LDPE and the blend of SL-50 by using Eqs. (4.15-4.18) as demonstrated in Tables 4.6, 4.7 and 4.8. In addition, a low β value of $10^\circ\text{C}/\text{min}$ is considered to mitigate the impact of the interaction among the reagents, since high values of β can increase the interaction of constituents (Cao et al., 2014). The values of A ranged from 1.63×10^3 to $7.32 \times 10^{25} \text{ s}^{-1}$, 3.22×10^4 to $5.78 \times 10^{26} \text{ s}^{-1}$ and 2.29×10^{03} to $1.13 \times 10^{26} \text{ s}^{-1}$ for SS, 3.77×10^{22} to $6.35 \times 10^{24} \text{ s}^{-1}$, 2.58×10^{23} to $5.09 \times 10^{25} \text{ s}^{-1}$ and 1.03×10^{27} to $4.45 \times 10^{29} \text{ s}^{-1}$ for LDPE and 9.06×10^{07} to $3.98 \times 10^{37} \text{ s}^{-1}$, 1.06×10^{09} to $1.03 \times 10^{39} \text{ s}^{-1}$ and 1.25×10^{08} to $7.60 \times 10^{37} \text{ s}^{-1}$ for the blend of SL-50 as calculated by KAS, FWO and Starink methods, respectively. Normally, A value is an indication of the number of times molecules will hit in the orientation necessary to trigger a reaction (Balasundram et al., 2018). High values of A ($\geq 10^9 \text{ s}^{-1}$) points out a highly complex reaction when the reaction is not dependent on the surface area, contrarily, lower values of A ($\leq 10^9 \text{ s}^{-1}$) indicate a surface reaction (Shahbeig and Nosrati, 2020). Furthermore, A value in the range of 10^{10} to 10^{12} s^{-1} indicates that the activated complex was presumably restrained in rotation compared to the initial reactant (Ahmad et al., 2017a). In this present study, the SS and SL-50 showed that there are complex materials, with multi-phasic decomposition reaction chemistry due to variation in A value.

ΔH is a function of absorbed or released heat at an isobaric process and for pyrolysis, it indicates the total amount of heat exchanged between the reagent and activated complex during the thermal process (Ahmad et al., 2018; Kim et al., 2010). All models revealed positive ΔH which means an external source of energy needs to be provided in order to lift the energy level of the reactants to their transition state (Naqvi et al., 2019). Likewise, it has been stated by Ahmad et al. that a difference of $\sim 6 \text{ kJ/mol}$ between E value and ΔH indicates that negligible potential energy

barrier exists, hence, product formation would be easier to achieve (Ahmad et al., 2017b). ΔH values for SS were computed using KAS (142.61-54.36 kJ/mol), FWO (150.20-70.22 kJ/mol) and Starink (143.91-56.18 kJ/mol), respectively. Positive ΔH change by all free-models reflects the pyrolysis of SS is endothermic. This finding is in accordance with the previous conclusion of (Naqvi et al., 2018). The lower ΔH indicates that SS could be used in co-feeding pyrolysis with various biomasses for thermal conversion into bioenergy. Conversely, it was noticed that the ΔH variation for LDPE was in a steady mode with the average value of 336.06, 348.33 and 338.56 kJ/mol for KAS, FWO and Starink, respectively. For SL-50 the ΔH raised as the conversion rate increased from 10 to 90%. The average value of ΔH for the composting is 194.56, 206.44 and 196.49 kJ/mol for KAS, FWO and Starink, respectively with an acceptable deviation of around 3.2%. In addition, one should note that a small potential energy barrier was created indicating the feasibility of the reaction to appear, due to the formation of an activation complex (Mehmood et al., 2017).

The change in ΔG , also known as Free Enthalpy, shows the overall increase in energy at the approach of the reagents and the formation of the activated complex. Here, the average ΔG values of SS (~87 kJ/mol) were shown that are lower when compared with the average ΔG values of the LDPE (~114 kJ/mol) in all models. The average ΔG for the SL-50 revealed a slight increase (~119 kJ/mol), calculated by KAS, FWO and Starink methods, respectively. The average ΔG of the blend, in contrast to the SS and LDPE, was higher. These values were shown to be lower when compared with the ΔG values of the SS and rice husk (121.82 kJ/mol) (Raza et al., 2019) and SS and sugar cane bagasse (137.91 kJ/mol) (Hameed et al., 2018) mixtures.

Changes in ΔS have both negative and positive values in all materials and methods. The positive values reveal that the “degree of arrangement” of activated complex was higher when compared to the initial reagents, and negative values indicate contrary. The phenomena of negative and positive values are attributed to the complexity of the process into generation of different products, which by use of GC/MS or nuclear magnetic resonance (NMR) may be identified. In addition, the ΔS of SS, LDPE and SL-50 for KAS, FWO and Starink methods are less than <0.5 kJ/mol.K. Low ΔS could be attributed to the fact that the solid material has just faced some kind of physical or chemical process, bringing it to a state near its thermodynamic equilibrium (Xu and Chen, 2013). In this condition, the SS and LDPE showed less reactivity, enhancing the necessary

time to form the activated complex. The changes of ΔS agreed with the A value since it contains entropy member $[\exp (\Delta S/R)]$.

Table 4.6. Thermodynamics parameters of SS, LDPE and SL-50 using KAS method.

| α | SS | | | | LDPE | | | | SL-50 | | | |
|----------|---------------------------------|------------------------|------------------------|------------------------------|---------------------------------|------------------------|------------------------|------------------------------|---------------------------------|------------------------|------------------------|------------------------------|
| | A (s ⁻¹) | ΔH (kJ/mol) | ΔG (kJ/mol) | ΔS (kJ/mol. K) | A (s ⁻¹) | ΔH (kJ/mol) | ΔG (kJ/mol) | ΔS (kJ/mol. K) | A (s ⁻¹) | ΔH (kJ/mol) | ΔG (kJ/mol) | ΔS (kJ/mol. K) |
| 0.1 | 5.98×10^1 ₁ | 142.61 | 87.02 | 0.16 | 3.77×10^2 ₂ | 317.79 | 114.51 | 0.43 | 9.06×10^0 ₇ | 72.20 | 123.04 | -0.11 |
| 0.2 | 1.13×10^2 ₁ | 250.89 | 85.37 | 0.46 | 9.33×10^2 ₂ | 323.15 | 114.44 | 0.44 | 5.61×10^1 ₃ | 122.63 | 121.00 | 0.00 |
| 0.3 | 3.53×10^2 ₃ | 280.06 | 85.04 | 0.55 | 1.80×10^2 ₃ | 327.07 | 114.39 | 0.45 | 5.69×10^1 ₆ | 148.97 | 120.24 | 0.06 |
| 0.4 | 7.22×10^2 ₄ | 295.34 | 84.89 | 0.59 | 7.14×10^2 ₃ | 335.36 | 114.30 | 0.47 | 3.90×10^1 ₇ | 156.29 | 120.06 | 0.08 |
| 0.5 | 7.32×10^2 ₅ | 307.05 | 84.77 | 0.62 | 1.37×10^2 ₄ | 339.28 | 114.25 | 0.48 | 2.51×10^2 ₁ | 190.40 | 119.29 | 0.15 |
| 0.6 | 1.46×10^1 ₀ | 121.98 | 87.43 | 0.10 | 3.28×10^2 ₄ | 344.53 | 114.19 | 0.49 | 2.71×10^2 ₄ | 217.66 | 118.77 | 0.21 |
| 0.7 | 3.92×10^0 ₆ | 80.40 | 88.58 | 0.02 | 2.64×10^2 ₄ | 343.17 | 114.21 | 0.49 | 7.64×10^2 ₆ | 239.73 | 118.40 | 0.25 |
| 0.8 | 1.63×10^0 ₃ | 42.09 | 90.28 | -0.13 | 4.06×10^2 ₄ | 345.76 | 114.18 | 0.49 | 7.02×10^2 ₉ | 266.47 | 117.98 | 0.31 |
| 0.9 | 2.49×10^0 ₄ | 54.36 | 89.58 | -0.10 | 6.35×10^2 ₄ | 348.43 | 114.15 | 0.50 | 3.98×10^3 ₇ | 336.66 | 117.07 | 0.46 |
| Avg | - | 174.98 | 87.00 | - | - | 336.06 | 114.29 | - | - | 194.56 | 119.54 | - |

Table 4.7. Thermodynamics parameters of SS, LDPE and SL-50 using FWO method.

| α | SS | | | | LDPE | | | | SL-50 | | | |
|----------|---------------------------------|------------------------|------------------------|------------------------------|---------------------------------|------------------------|------------------------|------------------------------|---------------------------------|------------------------|------------------------|------------------------------|
| | A (s ⁻¹) | ΔH (kJ/mol) | ΔG (kJ/mol) | ΔS (kJ/mol. K) | A (s ⁻¹) | ΔH (kJ/mol) | ΔG (kJ/mol) | ΔS (kJ/mol. K) | A (s ⁻¹) | ΔH (kJ/mol) | ΔG (kJ/mol) | ΔS (kJ/mol. K) |
| 0.1 | 2.68×10^1 ₂ | 150.20 | 86.87 | 0.18 | 2.58×10^2 ₃ | 329.46 | 114.37 | 0.46 | 1.06×10^0 ₉ | 81.56 | 122.58 | -0.09 |
| 0.2 | 6.46×10^2 ₁ | 259.85 | 85.27 | 0.49 | 6.68×10^2 ₃ | 335.10 | 114.30 | 0.47 | 9.07×10^1 ₄ | 133.40 | 120.68 | 0.03 |
| 0.3 | 2.32×10^2 ₄ | 289.74 | 84.94 | 0.57 | 1.33×10^2 ₄ | 339.19 | 114.26 | 0.48 | 1.22×10^1 ₈ | 160.90 | 119.95 | 0.09 |
| 0.4 | 5.24×10^2 ₅ | 305.55 | 84.79 | 0.62 | 5.36×10^2 ₄ | 347.60 | 114.16 | 0.50 | 8.77×10^1 ₈ | 168.42 | 119.77 | 0.10 |
| 0.5 | 5.78×10^2 ₆ | 317.70 | 84.67 | 0.65 | 1.05×10^2 ₅ | 351.62 | 114.12 | 0.51 | 5.81×10^2 ₂ | 202.70 | 119.05 | 0.17 |
| 0.6 | 1.44×10^1 ₁ | 133.53 | 87.17 | 0.13 | 2.53×10^2 ₅ | 356.95 | 114.06 | 0.52 | 6.44×10^2 ₅ | 230.09 | 118.56 | 0.23 |
| 0.7 | 5.18×10^0 ₇ | 93.21 | 88.17 | 0.01 | 2.07×10^2 ₅ | 355.68 | 114.07 | 0.51 | 1.86×10^2 ₈ | 252.28 | 118.20 | 0.28 |
| 0.8 | 3.22×10^0 ₄ | 56.38 | 89.52 | -0.09 | 3.22×10^2 ₅ | 358.34 | 114.04 | 0.52 | 1.75×10^3 ₁ | 279.12 | 117.80 | 0.34 |
| 0.9 | 6.46×10^0 ₅ | 70.22 | 88.90 | -0.05 | 5.09×10^2 ₅ | 361.08 | 114.01 | 0.53 | 1.03×10^3 ₉ | 349.49 | 116.92 | 0.48 |
| Avg | - | 186.26 | 86.70 | - | - | 348.33 | 114.15 | - | - | 206.44 | 119.28 | - |

Table 4.8. Thermodynamics parameters of SS, LDPE and SL-50 using Starink method.

| α | SS | | | | LDPE | | | | SL-50 | | | |
|----------|---------------------------------|------------------------|------------------------|------------------------------|---------------------------------|------------------------|------------------------|------------------------------|---------------------------------|------------------------|------------------------|------------------------------|
| | A (s ⁻¹) | ΔH (kJ/mol) | ΔG (kJ/mol) | ΔS (kJ/mol. K) | A (s ⁻¹) | ΔH (kJ/mol) | ΔG (kJ/mol) | ΔS (kJ/mol. K) | A (s ⁻¹) | ΔH (kJ/mol) | ΔG (kJ/mol) | ΔS (kJ/mol. K) |
| 0.1 | 7.74×10^1 ₁ | 143.91 | 86.99 | 0.16 | 1.03×10^2 ₇ | 320.16 | 114.48 | 0.44 | 1.25×10^0 ₈ | 73.43 | 122.98 | -0.10 |
| 0.2 | 1.61×10^2 ₁ | 252.72 | 85.35 | 0.47 | 3.01×10^2 ₇ | 325.57 | 114.41 | 0.45 | 8.40×10^1 ₃ | 124.19 | 120.96 | 0.01 |
| 0.3 | 5.23×10^2 ₃ | 282.08 | 85.02 | 0.55 | 6.57×10^2 ₇ | 329.52 | 114.37 | 0.46 | 8.96×10^1 ₆ | 150.73 | 120.20 | 0.06 |
| 0.4 | 1.09×10^2 ₅ | 297.48 | 84.87 | 0.60 | 3.34×10^2 ₈ | 337.85 | 114.27 | 0.48 | 6.22×10^1 ₇ | 158.11 | 120.01 | 0.08 |
| 0.5 | 1.13×10^2 ₆ | 309.28 | 84.75 | 0.63 | 7.24×10^2 ₈ | 341.79 | 114.22 | 0.48 | 4.14×10^2 ₁ | 192.36 | 119.25 | 0.15 |
| 0.6 | 2.02×10^1 ₀ | 123.62 | 87.39 | 0.10 | 2.03×10^2 ₉ | 347.07 | 114.17 | 0.50 | 4.59×10^2 ₄ | 219.73 | 118.74 | 0.21 |
| 0.7 | 5.42×10^0 ₆ | 82.01 | 88.53 | -0.02 | 1.57×10^2 ₉ | 345.72 | 114.18 | 0.49 | 1.33×10^2 ₇ | 241.90 | 118.36 | 0.26 |
| 0.8 | 2.29×10^0 ₃ | 43.71 | 90.19 | -0.13 | 2.62×10^2 ₉ | 348.33 | 114.15 | 0.50 | 1.25×10^3 ₀ | 268.75 | 117.95 | 0.31 |
| 0.9 | 3.63×10^0 ₄ | 56.18 | 89.49 | -0.09 | 4.45×10^2 ₉ | 351.01 | 114.12 | 0.50 | 7.60×10^3 ₇ | 339.21 | 117.04 | 0.46 |
| Avg | - | 176.78 | 86.95 | - | - | 338.56 | 114.26 | - | - | 196.49 | 119.50 | - |

4.4. Conclusion

The co-pyrolysis of SS with LDPE was investigated, for the first time, through TGA. It was found that total decomposition of SS and LDPE mixture takes place in temperature range of 200-600 °C. The mixing ratio of LDPE had a crucial impact on the co-pyrolysis behavior due to hydrogen donation by LDPE in decomposition process. The blend ratio of 1:1 was pronounced as an optimum ratio from the perspective of high index D and shifting T_{max} to lower temperature. Moreover, co-conversion of SS and LDPE lead to lower formation of char from experimental cases in comparison to the calculated cases, indicating a synergic interaction between the materials. Within the scope of this study, kinetic parameters of pyrolysis and co-pyrolysis were calculated using different modeling approaches. The E value based on Coats-Redfern method was 30.01 kJ/mol, 187.40 kJ/mol and 37.2 kJ/mol for SS, LDPE and SL-50, respectively. The Coats-Redfern kinetic study revealed a considerable decrease in E value for SS and LDPE when the samples were co-fed in a 1:1 blend ratio. Subsequently, there was a little variation in the E value energy calculated by KAS (200.37 kJ/mol), FWO (212.25 kJ/mol) and Starink (202.30 kJ/mole) methods. Furthermore, the thermodynamic parameters of ΔH , ΔG and ΔS , as well as the A value, were calculated and discussed for iso-conversional procedures. The ΔH and ΔG values of SL-50 calculated by iso-conversional methods were in the range of (194.56-206.44 kJ/mol) and (119.28-119.54 kJ/mol), indicating available energy to be considered as a feasible blend for bioenergy production. The iso-conversional methods depicted consistency with one another and applicability to simulate the industrial scale of the co-pyrolysis plant. Herein, kinetic and thermodynamic parameters knowledge will provide referential values to describe the pyrolytic and co-pyrolytic of SS and LDPE for bioenergy application.

CHAPTER 5

CATALYTIC PYROLYSIS OF SEWAGE SLUDGE WITH HZSM5 AND SLUDGE-DERIVED ACTIVATED CHAR: A COMPARATIVE STUDY USING TGA-MS AND ARTIFICIAL NEURAL NETWORKS

5.1. Introduction

With the rapid economic development, urbanization and industrialization, SS generation rate has been escalating globally. For instance, SS production in the United States had an average of 17.8 million tons/year in the last decade and Canada produces approximately 4 million tons/year (Fang et al., 2020; Wu et al., 2020). The conventional management routes for disposal such as landfilling, incineration, biological treatments and composting, may have serious adverse effects on the environment linked to the SS intrinsic properties (Chen et al., 2019). Besides, the above-mentioned methods are time-consuming and require high energy to proceed which may have limited their future application (He et al., 2020). Meanwhile, renewable energies are getting increasing attention and are considered eco-friendly alternatives to fossil fuels (Zhang et al., 2016b). Several thermochemical processes have been developed (e.g., incineration, pyrolysis, gasification and hydrothermal treatment) to simultaneously retrieve energy and reduce the SS volume. Each thermochemical process has its own technological and socio-economic pros and cons which have been recently reviewed by (Gao et al., 2020).

Among various potential thermochemical processes, recent efforts include developing pyrolysis as a versatile and promising technology (Raza et al., 2019). Pyrolysis converts the organic compounds present in the feedstock into value-added products in an oxygen-free environment at elevated temperatures. Thus, pyrolysis has been largely investigated to convert SS into bioenergy (Tomasi Morgano et al., 2018). The converted compounds can be valorized for a variety of applications such as energy through industrial chemicals (bio-oil and bio-gas) and agricultural (char) (Ahmad et al., 2017b; Chanaka Udayanga et al., 2018; Wang et al., 2017). The liquid bio-oil is the major substantial product; however, its high oxygen and nitrogen content reduces the energy density and causes immiscibility with hydrocarbon-based fuels making the refining process difficult and costly (Fonts et al., 2012; Mullen et al., 2018). Therefore, considerable efforts have been devoted to the challenging task of enhancing the properties of the

bio-oil and improving the efficiency of the entire process (S. Liu et al., 2017). Commonly, zeolites have demonstrated efficiencies in the petrochemical industry due to the strong acidity for carbon-carbon bond scission and their distinct structural properties (Liu et al., 2010). Therefore, zeolite catalysts have been investigated for upgrading pyrolysis vapors in the production of bio-based compounds through SS pyrolysis, although the number of studies is limited (Zaker et al., 2019). Among the zeolite-based catalysts, HZSM5 outperformed other types because of their narrow pore diameter and shape selectivity for pyrolysis vapors from SS (Persson et al., 2019). Research has focused on the catalytic conversion of SS over HZSM5 to upgrade the bio-oil quality (Yu et al., 2016). Reduction in oxygen and nitrogen heteroatoms (Xie et al., 2014), enhancements in the production of aromatics, olefins, and hydrocarbons are observed (Liu et al., 2016; Wang et al., 2017). However, zeolites are relatively expensive, and the catalyst preparation steps are time and energy-consuming, limiting their application (Shen et al., 2014).

Recently, increasing interest has been devoted to the use of AC as a catalyst in reforming pyrolytic vapors due to their bulky surface area, porosity, and embedded active sites (Daorattanachai et al., 2018; Zhang et al., 2018b). Researchers have studied the performance of ACs to upgrade pyrolytic products (Xiong et al., 2017). Different ACs derived from other biomass such as corn stover (Zhang et al., 2018b) and rice husk (Shen et al., 2014) have been investigated for the production of jet fuel range hydrocarbons (Zhang et al., 2019), phenol rich bio-oil (Guo et al., 2019) and hydrogen rich syngas (Zhang et al., 2018a). The previous studies are mainly engaged in the topics of AC derived from biomasses, and such kinds of catalysts and processes have not been reported for SS extensively to date. The AC can be also derived from SS containing metal oxides for catalytic purposes, and it is widely available and inexpensive (Daorattanachai et al., 2018; Gao et al., 2020; Hu et al., 2018). Subsequently, influence of different range of catalysts such as HZSM5 and AC needs to be studied comparatively for SS pyrolysis for the benefit of process efficiency. Additionally, there has been a lack of studies about evolved gases during pyrolysis of SS. Unlike other biomasses, the nitrogen and sulfur content in SS is high which leads to formation of toxic and/or pollutants during pyrolysis resulting in photochemical smog and acid rain (Tian et al., 2013; J. Zhang et al., 2017a).

Therefore, this study attempts to explore the feasibility of using sludge-derived AC as a low-cost alternative catalyst to commercial HZSM5 in SS pyrolysis for the first time. The aim of using catalyst is to characterize the thermal behavior and to cut the E value. Besides, there are

limited studies to improve understanding of gas emission characteristics of the SS under different catalysts. In this respect, detailed characterization of SS and TGA to clarify the decomposition behavior and pathway of SS with these catalysts was firstly conducted in this study. Pyrolytic gaseous released during the SS decomposition process were identified, and the effects of HZSM5 and AC catalysts were studied comparatively. The kinetic models including Coats-Redfern method were then utilized to examine the E value and reaction order. Furthermore, the chemical composition of bio-oils derived from pyrolysis and catalytic pyrolysis of SS in the presence of AC and HZSM5 with different ratios were explored comparatively. Based on the experimental results, an artificial neural network (ANN) method was developed and trained to further simulate and predict the catalytic thermal degradation process.

5.2. Materials and methods

5.2.1. Materials

In this study, two types of catalysts were explored with SS; a commercially available zeolite catalyst ZSM5 (surface area = 425 m²/g, Si/Al ratio = 50, p = 500 μm) and AC derived from SS. The ZSM5 was purchased from Alfa Aesar (CAS 1318-02-1) and calcined at 550 °C for 5 h in a tubular furnace to activate (HZSM5) before use. Three different SS to catalyst ratios with a fixed SS loading were tested. The ratios of SS to catalysts were 4:1 initiated as SSHZSM5@4-1 and SSAC@4-1; 2:1 initiated as SSHZSM5@2-1 and SSAC@2-1, and for an equal portion of 1:1 labeled as SSHZSM5@1-1 and SSAC@1-1.

5.2.2. Simultaneous TGA/MS analysis

The pyrolysis and catalytic pyrolysis experiments were implemented in a TGA apparatus (TA-Q500) coupled with mass spectrometry (MS) (TA-Discovery MS). In this study, in order to reduce the influence of sample quantity on the intensity of MS and to avoid systematic errors and minimize heat and mass transfer influence, about 2.5 mg of SS was loaded into the ceramic pans for pyrolysis experiment. In the catalytic experiments, a mixture of 2.5 mg SS and 2.5 mg catalysts were placed in the pans, which the mass ratio of SS and mixed catalysts was nearly 1:1. TGA and DTG variations were recorded in the range of 30 to 1000 °C at a constant β of 10 °C/min under the argon atmosphere, to obtain a high conversion rate (Liu et al., 2015). The pyrolytic vapors

were passed through a transfer line continuously heated at 400 °C. Throughout MS analysis, a secondary electron multiplier type detector was employed. The intensities of the evolved gases were screened out by evolution curves during a preliminary scan from mass to charge ratios (m/z) 2 to 100.

Next, the focus was on the ions that correspond to evolution of harmful species in the pyrolysis and catalytic pyrolysis. Baselines with numerous blank trials were first achieved and the selection of target ions was prepared considering results of continuously repeated scanning. Ion currents of the specific ions are recorded using multiple ion detection (MID) mode with the Quedara software's assistance. Accordingly, the accuracy of the TGA instrument was high both for the measurement of mass and for temperature control. To ensure the reproducibility and repeatability of the data; triplicate TGA/MS tests were performed. The maximum variation in the α from sample to sample of the same materials was 0.02, and their mean value was presented in the outcomes. The selected identification of gaseous evolution from MS is shown in Table 5.1.

Table 5.1. Identified pyrolytic gaseous by MS.

| Ion | CH ₄ | HCN | CO ₂ | NO ₂ | CH ₃ SH | SO ₂ |
|-----|-----------------|-----|-----------------|-----------------|--------------------|-----------------|
| m/z | 16 | 27 | 44 | 46 | 48 | 64 |

5.2.3. Kinetic study

To determine the impacts of the HZSM5 and AC on the kinetic parameters throughout the valorization of SS, the weighted average activation energy (E_m , kJ/mol) was computed and applied to analyze samples reactivity (L. Huang et al., 2018).

$$E_m = E_1F_1 + E_2F_2 + \dots + E_nF_n \quad (5.1)$$

here, E_1 to E_n are activation energy at each pyrolysis stage (Eqs. 4.10 and 4.11); and F_1 to F_n are quantities of weight losses.

5.2.4. Artificial neural network development

ANNs are extensively applied to predict the non-linear relationships between input and output data. Recently, ANNs have been used for the prediction of data obtained from

thermogravimetric (Naqvi et al., 2018; Raza et al., 2019; Sunphorka et al., 2017). Herein, an ANN method was developed to predict the SS catalytic pyrolysis behavior. The network architecture of the ANN model was developed via a Feedforward Multiple Layer Perception (FMLP) based on Levenberg-Marquardt (LM) back-propagation, with MATLAB. The back-propagation algorithm utilizes the scheme in which weights are calculated using the output as feedback of input. In FLMP, there is an input layer and an output layer that comprises one or more number of inputs and outputs, respectively. Temperature (°C) and β (°C/min) have been selected as the inputs and the TGA profiles for the production. The hidden layer was used to implement the non-linear function on ANN. The hidden layer comprises different numbers of neurons that were selected based on maximum R^2 value. The number of hidden layers, number of neurons in hidden layers and transfer function were chosen using a trial and error analysis depending on the performance criteria. Model performance was evaluated considering the mean square error (MSE) in Eq. (5.2), root mean square error (RMSE) in Eq. (5.3), mean absolute error (MAE) in Eq. (5.4), mean bias error (MBE) in Eq. (5.5) and R^2 in Eq. (5.6) between predicted and experimental TGA values. Lower MSE, RMSE, MAE, MBE values and higher R^2 values indicate more optimized ANN architecture. The selected network architecture parameters are presented in Table 5.2.

$$\text{MSE} = \frac{1}{n} \left[\sum_{i=1}^n (H_i - H_{i,\text{model}})^2 \right] \quad (5.2)$$

$$\text{RMSE} = \sqrt{\frac{1}{n} \left[\sum_{i=1}^n (H_i - H_{i,\text{model}})^2 \right]} \quad (5.3)$$

$$\text{MAE} = \frac{1}{n} \sum_{i=1}^n |H_i - H_{i,\text{model}}| \quad (5.4)$$

$$\text{MBE} = \frac{1}{n} \sum_{i=1}^n (H_i - H_{i,\text{model}}) \quad (5.5)$$

$$R^2 = 1 - \frac{\sum_{i=1}^n (H_i - H_{i,\text{model}})^2}{\sum_{i=1}^n (H_i - \bar{H}_i)^2} \quad (5.6)$$

where H_i is the target value, $H_{i,\text{model}}$ is the network output of each pattern, and \bar{H}_i is the mean of target values.

Table 5.2. Parameters used for the development of ANN model.

| Parameters | Values |
|--------------------------------|---|
| Number of inputs | “2” 1. Temperature (°C) 2. Heating rate (°C/min) |
| Number of outputs | “1” 1. Weight loss (%) |
| Network type | Feed forward back propagation |
| Training function | Levenberg-Marquardt (LM) |
| Transfer function | Hidden layers: TANSIG (Hyperbolic tangent sigmoid function); Output layer: PURELIN (Linear transfer function) |
| Data division function | Dividerand (70-15-15) |
| Performance function | Mean square error (MSE) |
| Max number of epochs to trains | 1000 epoch |
| Error tolerance | 0.001 |

5.3. Results and discussion

5.3.1. Characteristics of AC catalyst

A preliminary idea about the structure of the AC was elucidated by SEM images. As displayed in Fig. 5.1(a), micropore sizes were observed in the prepared sorbent. AC is composed of agglomerated carbon particles with a size ranging from tens to hundreds of nanometers in diameter. Fig. 5.1(b) shows the EDX result of AC, demonstrating that there are several inorganic elements on the surface of the fabricated catalyst, such as iron, aluminum, titanium potassium, oxygen and silicon. This observation is in line with Table 3.1 data.

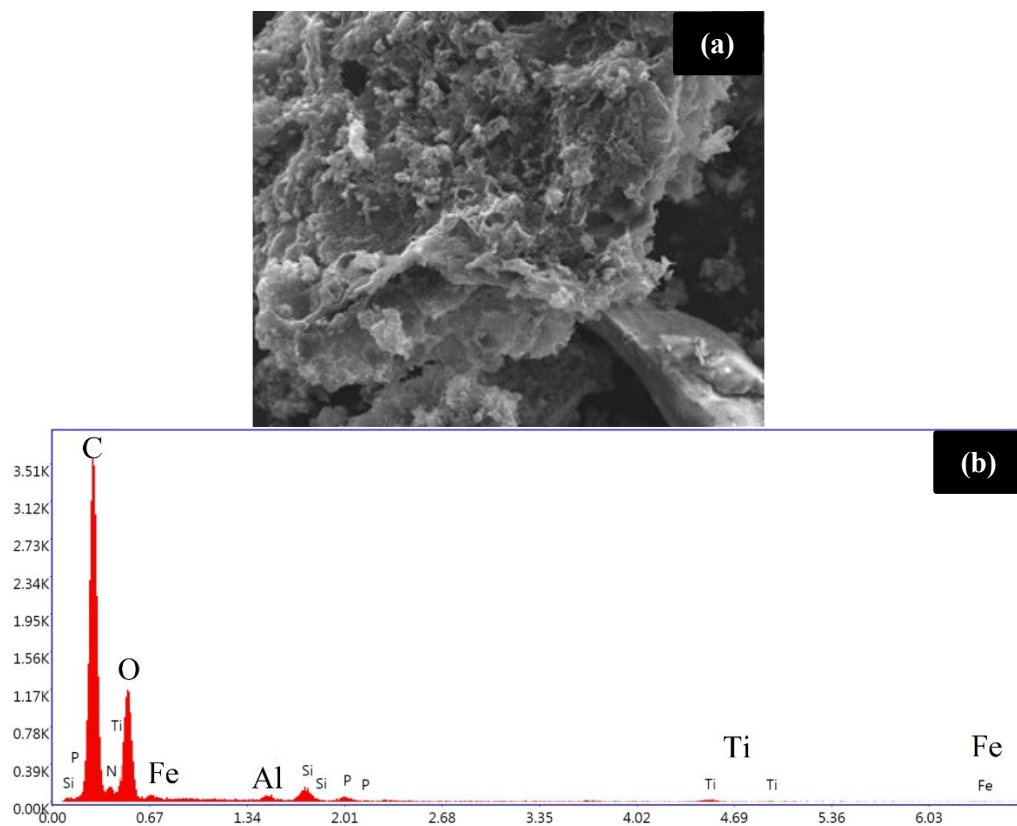


Fig. 5.1. (a) SEM image and (b) EDX of the AC catalyst

To identify the functional groups formed on the surface of AC sample, FT-IR analysis was conducted as represented in Fig. 5.2. The functional groups detectable on the IR spectrum may be responsible for the appearance of multiple bands in a wide range of wavenumbers. In this respect, each band may have a contribution of different functional groups present on the surface of the AC. Moreover, some functional groups like -C=O and -OH are usually formed during the production of AC and have proven to have a substantial influence on catalytic activity (Hadi et al., 2015; Zhang et al., 2019). The spectra of the examined AC exhibited two bands in the $2000\text{-}4000\text{ cm}^{-1}$ range. The broadband centered at about 3400 cm^{-1} can be ascribed to the stretching vibration of hydrogen-bonded hydroxyl groups of water, alcohols, or phenolic C-OH stretching as well as N-H stretching vibration in the amino bond (Zubrik et al., 2017). Likewise, inorganic materials such as sulfates and phosphates are in the approximate range of 3345 and 3440 cm^{-1} (Zielińska et al., 2015) which is in line with the data presented in Table 3.1. The narrow band around 2900 cm^{-1} is ascribed to the C-H symmetric and asymmetric vibration mode of ethyl and methylene groups (Lin et al., 2012). The band at about 1650 cm^{-1} is mainly the stretching vibrations of the carbonyl

groups belonging to various functional groups such as quinones, ketones, lactones, diketones, ketoester and ketoenol (Lin et al., 2012). The C-H stretching found at 1470 cm^{-1} and the phenol O-H bending is identified at 1410 cm^{-1} (Daorattanachai et al., 2018). The strongest peak at around 990 cm^{-1} is assigned to the C-O stretching vibration (Antunes et al., 2017). The peak at near 870 cm^{-1} can be allocated to the aromatic C-H bending vibrations (Shahrokhi-Shahraki et al., 2021). The latter may be confirmed by the presence of the band at 990 cm^{-1} (Zielińska et al., 2015).

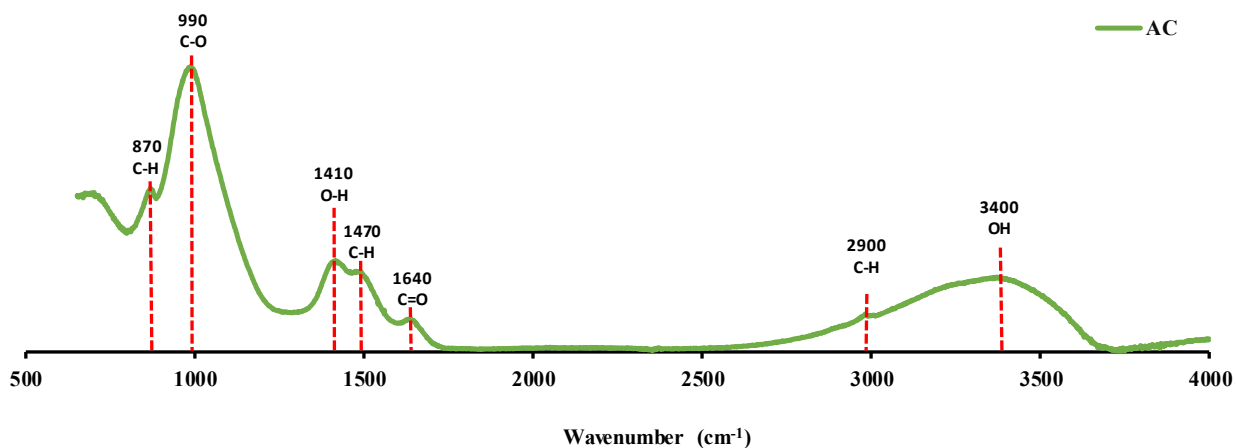


Fig. 5.2. FT-IR spectrum of AC catalyst.

To evaluate the thermal stability of the obtained AC, TGA was performed. Fig. 5.3. shows that the TGA/DTG curves of the AC are in good accordance with the results of a previous study (Saleh et al., 2017). Below $120\text{ }^{\circ}\text{C}$ and due to the desorption of absorbed water, about 8% weight loss is observed. The slight weight loss of 10% recorded above $200\text{ }^{\circ}\text{C}$ is linked to the presence of volatile compounds. The pronounced weight loss observed in the TGA analysis affirmed some functional groups such as amino and carboxyl groups existence on the surface of the AC, which is identified by FT-IR analysis (Saleh et al., 2017). Above $625\text{ }^{\circ}\text{C}$, the AC framework remained unchanged, indicating the high temperature durability of AC.

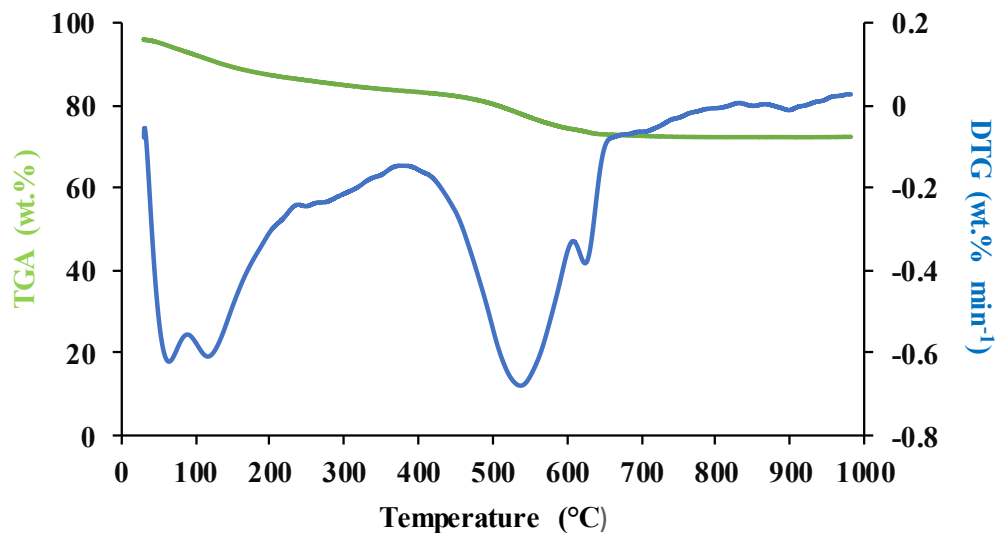


Fig. 5.3. TGA/DTG curves for AC catalyst.

A brief comparison of the surface areas of the prepared AC derived from SS via different chemical treatment methods (see Table 5.3) revealed that the strategy developed herein has higher efficiency in terms of the synthesis of highly porous and efficient catalysts. The obtained AC has a relatively larger BET surface area of 899.33 m²/g compared to previous studies (Zhang et al., 2019). In contrast to the carbonized SS obtained under the same conditions without the activation agent, the surface area has folded more than 10 times. It's worth to mention, among different activation methods available in the literature; chemical modification of SS with metal hydroxide agents such as NaOH and KOH has been investigated (Tan et al., 2017; Xiong et al., 2017). Activation with metal hydroxides not only increases the surface area but also creates several oxygenated functional groups on the surface of the AC (Sizmur et al., 2017). NaOH is more environmentally friendly than KOH and is deemed more economical and less corrosive for carbon activation (Rajapaksha et al., 2016). On the other hand, there are two main chemical preparation routes to activated SS; single-step and two-step procedures. Herein, a single-step chemical activation with NaOH was adapted since it is energetically more suitable compared to other processes (Zubrik et al., 2017).

Table 5.3. Comparison of the BET results of AC derived from SS pyrolysis.

| Activation procedure | Activation condition | | | Chemical treatment | | | BET (m ² /g) | Ref. |
|--|----------------------|---------|----------------|--------------------------------|--------------------------|--------------|-------------------------|--------------------------|
| | T (°C) | t (min) | Atm | Chemical activator | Imp.r ^a (w:w) | Acid washing | | |
| Carbonized SS | 700 | 120 | N ₂ | - | - | - | 69.63 | Present study |
| Dry single-step | 700 | 120 | N ₂ | NaOH | 1:1 | HCl (2M) | 899.33 | |
| Dry single-step | 550 | 60 | Ar | KOH | 1:1 | HCl (6M) | 186.00 | (dos Reis et al., 2016) |
| | | | | ZnCl ₂ | | | 192.00 | |
| Soaked in activator prior to pyrolysis | 500 | n/a | n/a | ZnCl ₂ | 5M | HCl (5M) | 721.00 | (Björklund and Li, 2017) |
| Soaked in activator prior to pyrolysis | 550 | 60 | N ₂ | ZnCl ₂ | 3M | HCl (1M) | 18.30 | (Huang et al., 2017) |
| | | | | H ₂ SO ₄ | | | 51.90 | |
| Dry two-step | 600 | 120 | N ₂ | NaOH | 1:1 | HCl (2M) | 346.49 | (Zou et al., 2013) |

^a Impregnation ratio.

5.3.2. Thermal decomposition behavior analysis

TGA/DTG profiles for SS, SSHZSM5@1-1 and SSAC@1-1 samples at non-isothermal conditions are depicted in Fig. 5.4. the three samples exhibit a relatively similar pattern which are consistent with the results obtained from catalytic pyrolysis of lignin over activated carbon (Bu et al., 2016) and zeolites (Luo et al., 2012) which were also mixed in the ratio of 1:1. The degradation process from the samples occurred over a wide temperature range from 30-1000 °C, and was divided into 4 significant stages based on the decomposition of different components. The first stage of degradation (30-200 °C) is accompanied mostly by dehydration of organic contents by losing both free water and chemically bonded water. One should note that stage one is not well explained in most previous literature. Generally, in the region of 120-200 °C the SS chemical structure starts to depolymerize and soften with the release of a very low quantity of light volatile compounds (Romanovskii and Martsul, 2009). In this stage, the weight loss is 6.01%, 2.67% and 6.87% for SS, SSHZSM5@1-1 and SSAC@1-1, respectively. Stage 2 and 3, commonly named as the active stages, are the main decomposition of reactive organic (Naqvi et al., 2018; Zaker et al., 2019). Seemingly, the mass loss in stage 2 is 31.14%, 13.25%, and 14.53% for SS, SSHZSM5@1-

1 and SSAC@1-1, respectively. This loss is ascribed to the diffusion of biodegradable organic components such as lipids and organic polymers. The DTG profiles of this stage sketched the largest peaks, which represent the maximum rate of mass loss at 352 °C, 357 °C and 358 °C for SS, SSHZSM5@1-1 and SSAC@1-1, respectively. This depicts both catalysts tend to slightly increase the temperature of the thermal degradation process and can be explained by the behavioral similarity of the catalysts (Bu et al., 2016; Luo et al., 2012). The third stage (400-600 °C) is related to the cleavage of higher molecular weight compounds into smaller ones alternative to chars formation by applying continuous heat, for instance, actively-decomposing reactions of proteins (Lin et al., 2016). The mass loss in this stage is lower than the previous stage, with a wide flat DTG profile. The mass loss is 16.25%, 7.51% and 13.44% for SS, SSHZSM5@1-1 and SSAC@1-1, respectively. After the triplets, the degradation process came into the fourth stage, which is the decomposition of inorganic matters, calcium carbonate and microcline decomposition (see Table 3.1), with a DTG peak arising from 600 to 700 °C for all samples. The thermal behavior trend for SSAC@1-1 is close to SS rather than SSHZSM5@1-1 which may be ascribed to AC devolatilization, formed primarily due to the scission of terminal C-C bonds in the structure of AC (Lee et al., 2017; Shen et al., 2014). Also, it can contribute to presence of mineral fractions (e.g., Ca, Mg, K, etc.) in SS and AC. Other authors presented similar trends and observations (Folgueras et al., 2013; Naqvi et al., 2019). After 700 °C, the mass-loss rate became slow and reached a stable steady state at 1000 °C. The total mass loss of SS, SSHZSM5@1-1 and SSAC@1-1 are 61.97%, 29%, and 42.58%, respectively. SSHZSM5@1-1 has a lower mass loss that to SSAC@1-1 and this can be attributed to the better thermal stability of HZSM5 (Xiang et al., 2018a). Although the presence of catalysts has abridged the mass losses, still can be beneficial by promoting selectivity on compounds of bio-oil for further research (Liang et al., 2017).

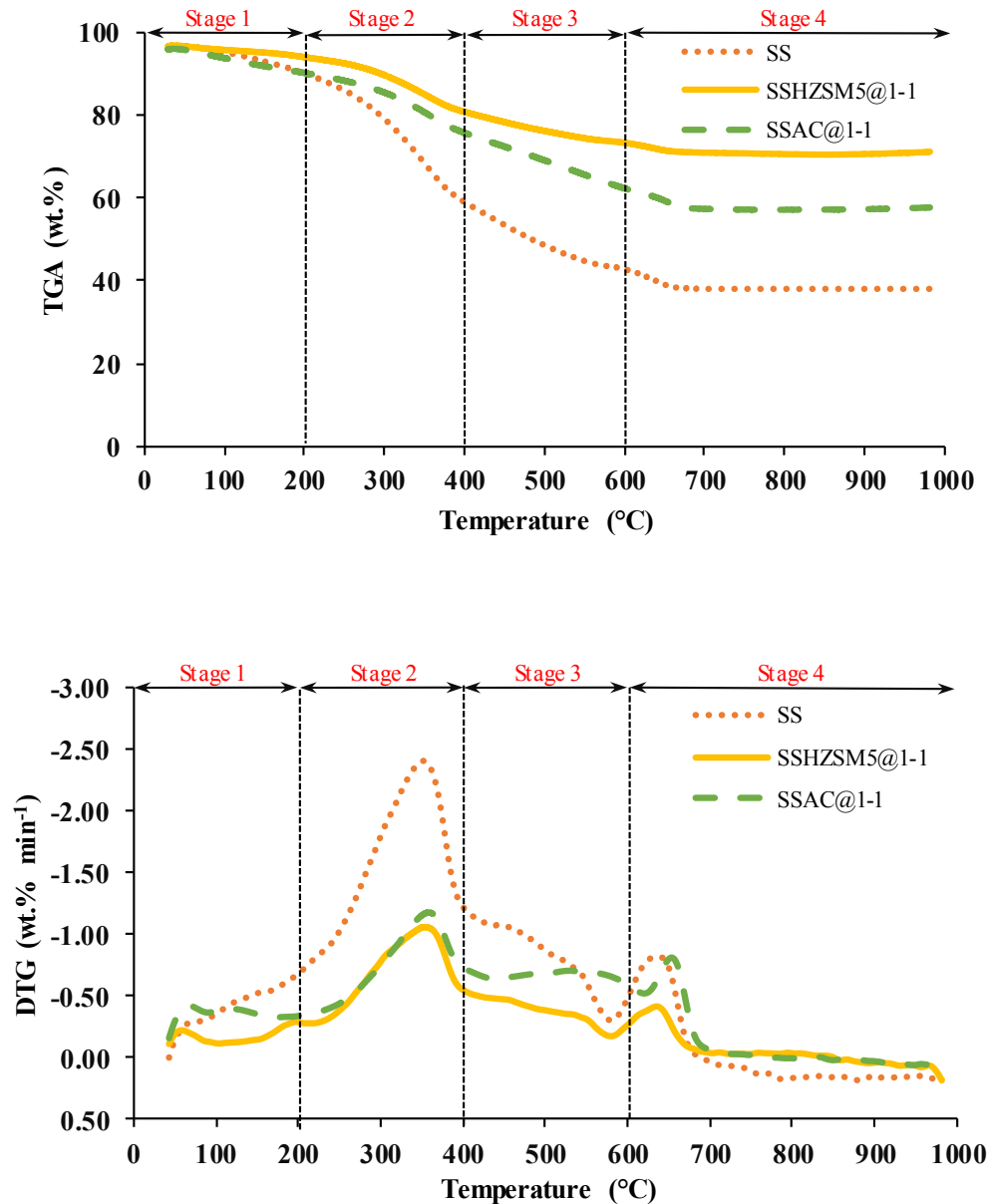


Fig. 5.4. TGA/DTG curves for SS, SSHZSM5@1-1 and SSAC@1-1.

5.3.3. Kinetic evaluation

In order to determine the pyrolysis and catalytic pyrolysis mechanisms, several solid-state mechanisms are computed by the differential methods (Balasundram et al., 2018). However, only Coats–Redfern method adequately described the pyrolysis reaction in each stage for non-isothermal kinetic analysis (Naqvi et al., 2019). Thus, this method is selected to analyze the kinetics of SS pyrolysis and catalytic pyrolysis of SSHZSM5@1-1 and SSAC@1-1. Fig. 5.5

indicates the conversion rate as a function of pyrolysis temperature ($^{\circ}\text{C}$) for SS, SSHZSM5@1-1 and SSAC@1-1. With the tested catalytic and non-catalytic pyrolysis, the samples did not influence the shape of the profiles indicating that the reaction mechanisms could be computed with the same reaction model.

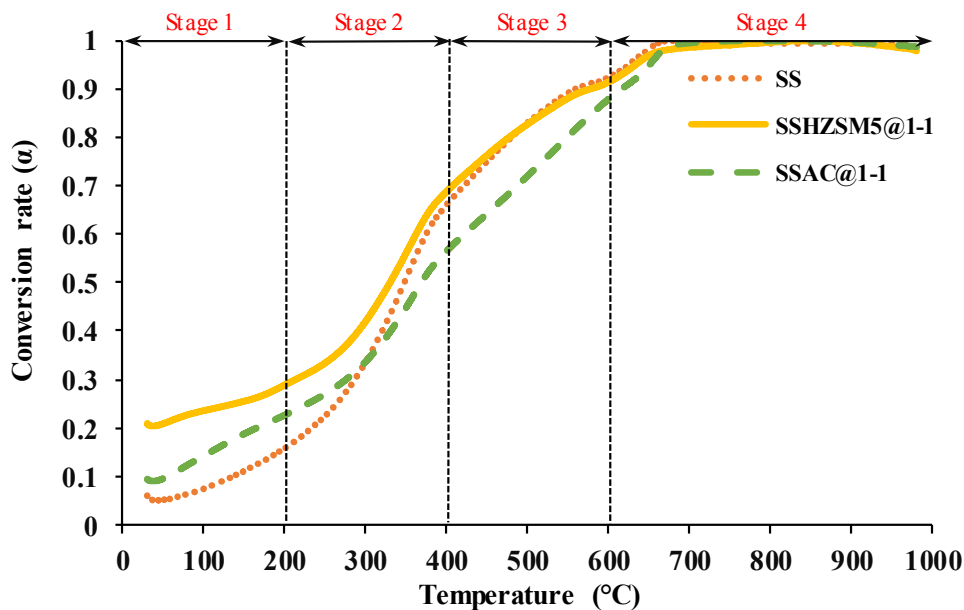


Fig. 5.5. Degree of conversion of SS, SSHZSM5@1-1 and SSAC@1-1 during pyrolysis and catalytic pyrolysis at $\beta=10$ $^{\circ}\text{C}/\text{min}$.

Fig. 5.6 illustrates the E value distribution of pyrolysis and catalytic pyrolysis (with different reaction orders $n=1, 2$ and 3), calculated by Eqs. (4.10) and (4.11) for SS, SSHZSM5@1-1 and SSAC@1-1. The R^2 acknowledged the acceptable accuracy of the outcomes. The obtained results are similar to that of SS pyrolysis found by other authors adapting the same mechanism (Hameed et al., 2018; Naqvi et al., 2019). Since significant weight loss was found between 200-600 $^{\circ}\text{C}$ for SS, the E value was calculated for stages 2 and 3 of degradation, which is also in concurrence with other studies (Xu et al., 2018). Likewise, the E_m value was calculated to observe the catalytic activity throughout the main devolatilization stage of pyrolysis.

In the second stage of pyrolysis, 200-400 $^{\circ}\text{C}$, it is perceived that the SS decomposition is first-order reaction ($R^2=0.964$) while for SSHZSM5@1-1 and SSAC@1-1 is third-order reaction (R^2 values are 0.855 and 0.86 for SSHZSM5@1-1 and SSAC@1-1, respectively). Correspondingly, presence of both catalysts has declined the E value for all three reaction orders

which is in good agreement to that obtained results by other researchers (Bu et al., 2016; Xiang et al., 2018a). This low E value can be ascribed to the trivial amount of energy required to trigger the thermal degradation (Liang et al., 2017). It is clear from Fig. 5.6 that the E value has dropped 10 kJ/mol for the first and second-order reaction and 15 kJ/mol for third-order reaction when AC is used as a catalyst. The decrease in the E value is more pronounced in the case of SSAC@1-1 compared to SSHZSM5@1-1 indicating higher catalytic activity at the second stage of decomposition. This phenomenon can be explained by the fact that SSAC@1-1 possesses a higher surface area. Thus, it is more favorable to the distribution of active sites of AC, which accelerates the degradation process of SS pyrolytic volatiles (Guo et al., 2018; Zhang et al., 2019). Furthermore, the use of an activating agent causes more reactive molecules to become activated molecules. Therefore, an upsurge in the number of reactant molecules per unit volume occurs, which decreases the E value (Hu et al., 2018). Subsequently, the best-fitted value for the order of reaction in temperature range of 400-600 °C is calculated as $n=2$ for SS ($R^2= 0.99$) and $n=1$ for catalytic pyrolysis (R^2 values are 0.992 and 0.952 for SSHZSM5@1-1 and SSAC@1-1, respectively). In this stage of pyrolysis, the E value is lowered by the catalysts and the values for both SSHZSM5@1-1 and SSAC@1-1 are proximate. For instance, when $n=2$ the E value is 26.45 and 27.75 kJ/mol for SSHZSM5@1-1 and SSAC@1-1, respectively, indicating a drop of around 10 kJ/mol in comparison to SS pyrolysis (33.77 kJ/mol). The reaction between AC catalyst and radicals, mainly H^\bullet , produced from the catalytic reaction is the essence of the pyrolytic vapors-AC interaction, and H^\bullet could even penetrate the AC at low temperatures (Yu et al., 2016). This could explain the better catalytic performance of the SSAC@1-1 than SSHZSM5@1-1 at lower temperatures. The mean activation energies obtained from catalytic pyrolysis of SS with SiO_2 , Al_2O_3 , Fe_2O_3 , and red mud are 191.1 kJ/mol, 189.8 kJ/mol, 175.6 kJ/mol, and 169.4 kJ/mol, respectively (Yang et al., 2018). HZSM5 has been modified with Zn and Co and used for rice straw catalytic pyrolysis (Liang et al., 2017; Xiang et al., 2018a). The addition of these modified HZSM5 had an identical reaction order in which the E value is almost the same or higher than the raw material. Compared to metal oxides and modified HZSM5, AC and HZSM5 used in this study proved higher catalytic activity in terms of energy saving.

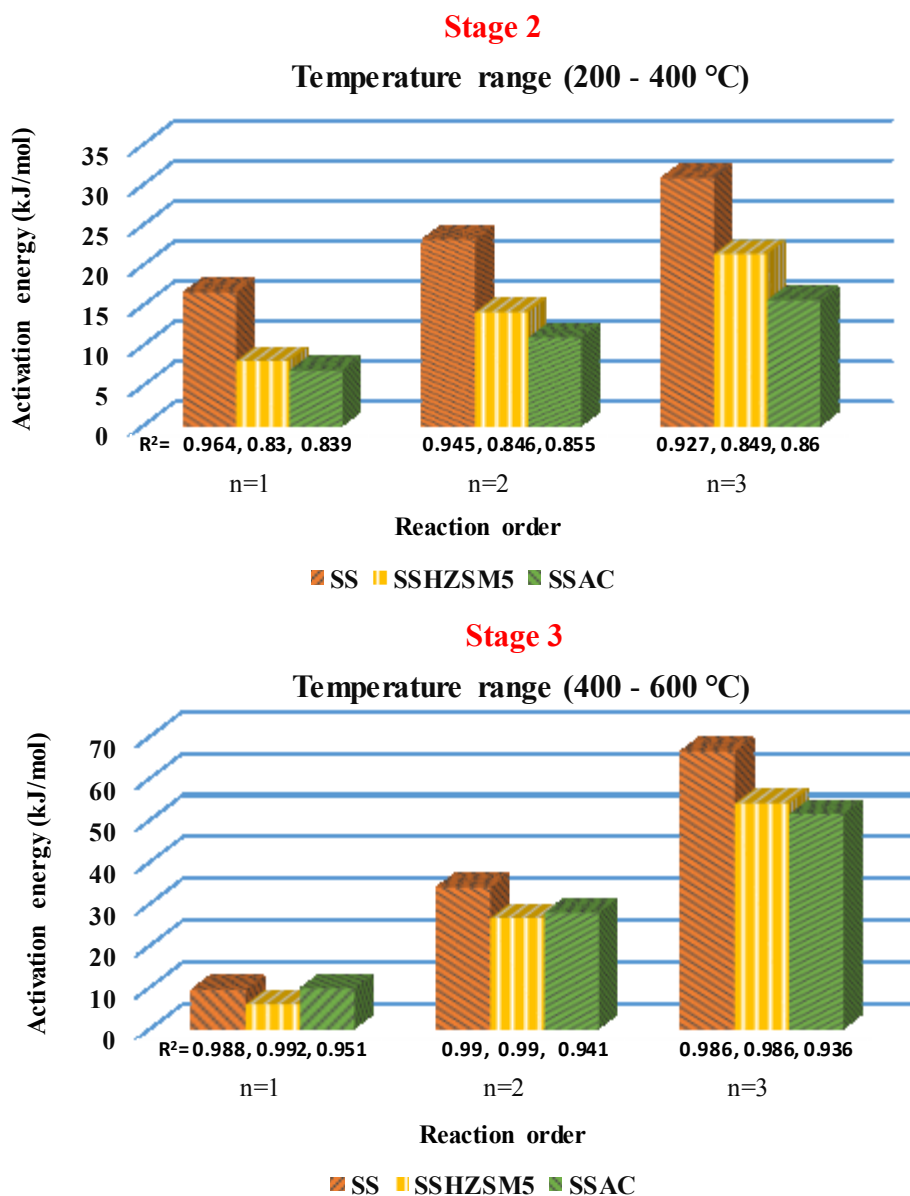


Fig. 5.6. The relation between reaction stages and activation energy for SS, SSHZSM5@1-1 and SSAC@1-1.

E_m values, as indicated in Fig. 5.7, for the three reaction orders, are estimated at 6.67 $\text{kJ}\cdot\text{mol}^{-1}$, 12.7 $\text{kJ}\cdot\text{mol}^{-1}$ and 20.36 $\text{kJ}\cdot\text{mol}^{-1}$ for SS; 1.51 $\text{kJ}\cdot\text{mol}^{-1}$, 3.86 $\text{kJ}\cdot\text{mol}^{-1}$ and 6.87 $\text{kJ}\cdot\text{mol}^{-1}$ for SSHZSM5@1-1; 2.29 $\text{kJ}\cdot\text{mol}^{-1}$, 5.32 $\text{kJ}\cdot\text{mol}^{-1}$ and 9.17 $\text{kJ}\cdot\text{mol}^{-1}$ for SSAC@1-1, respectively. The presence of catalysts increased the reaction activity, and the E_m is significantly reduced. These results confirm that sludge-based AC catalyst has almost the same performance as a commercial HZSM5 catalyst in the main devolatilization stages of SS pyrolysis. It can be attributed to the

presence of metals in the sludge-based AC which can catalyze the pyrolysis vapors passing through the pores, resulting in a decrease in the E_m value (Hu et al., 2018).

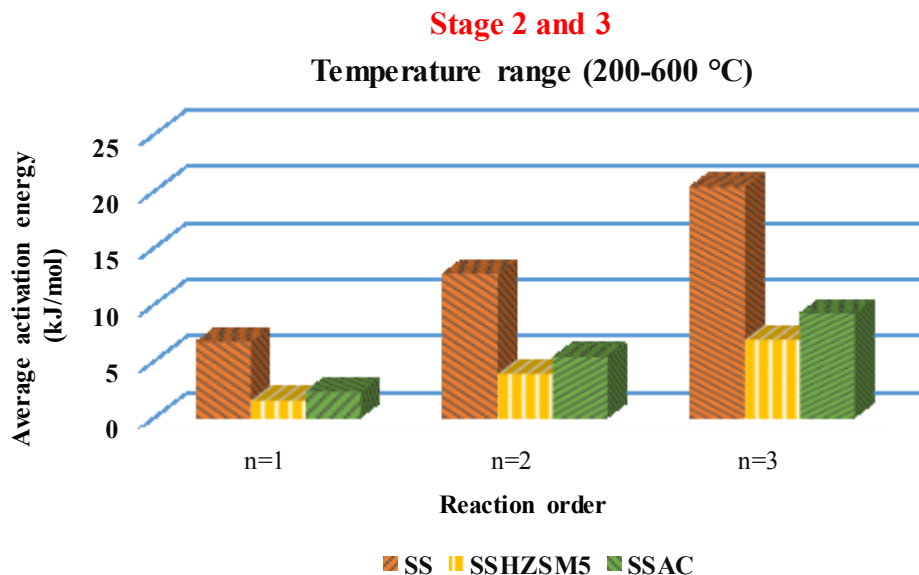


Fig. 5.7. The relation between reaction stages and average activation energy (E_m) for SS, SSHZSM5@1-1 and SSAC@1-1.

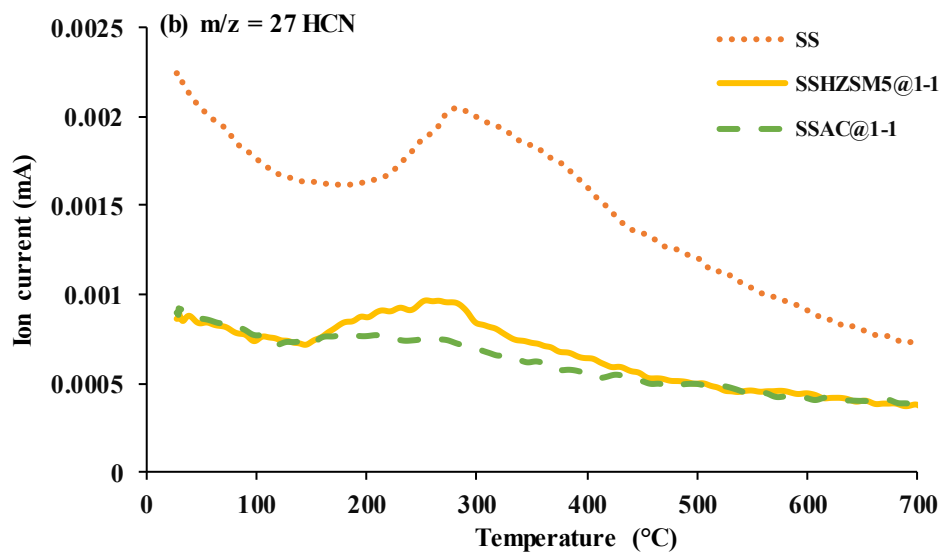
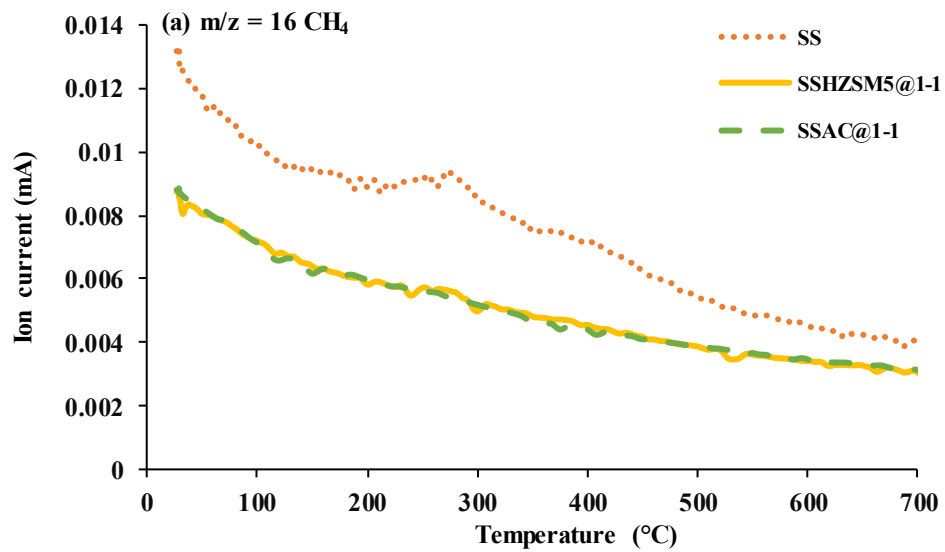
5.3.4. Monitoring pyrolysis gaseous

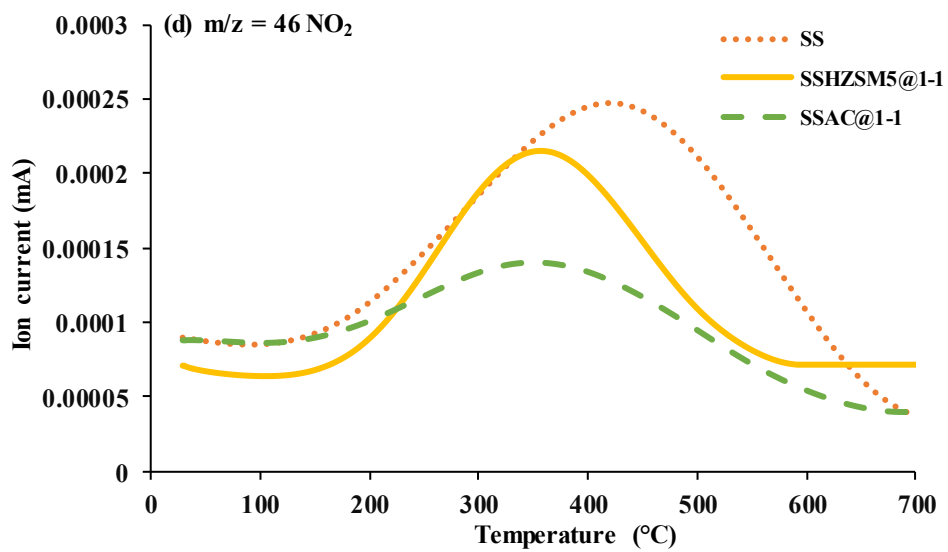
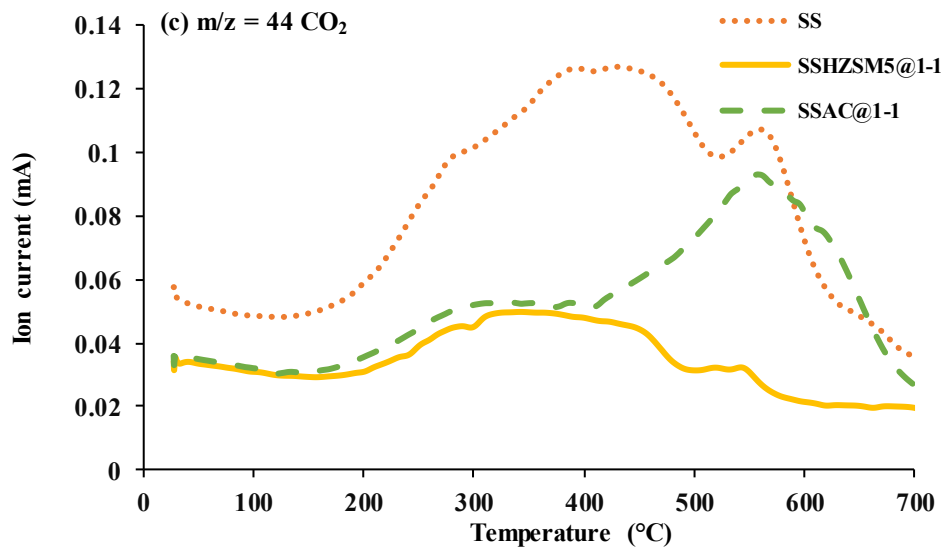
In thermochemical processes, the release of pyrolytic gaseous during SS pyrolysis can be identified with sensitivity due to synchronized measurement of analytical practices with TGA. (Özsin et al., 2019; Özsin and Pütün, 2019). Fig. 5.8 displays single ion curves of volatile compounds including CO_2 , CH_4 and nitrogen/sulfur-containing species evolving during SS non-catalytic and catalytic pyrolysis.

The levels of nitrogen/sulfur-containing volatile products are much lower than CO_2 and CH_4 emissions during the thermal degradation processes which are consistent with the ultimate analysis (Table 3.1). Emission of such compounds during SS pyrolysis can harm residents, accelerate the pace of global warming and reduce the value of the pyrolysis products (e.g., bio-gas). Also, the evolution and emissions pathways of these pyrolytic gaseous are still not well investigated to this date. CH_4 and CO_2 are reported in the literature to be the most abundant air pollutants in the earth's atmosphere (Hernández et al., 2017). CH_4 ($m/z=16$) is formed from

organic compounds containing $-CH_3$ groups and is generated continuously in a wide temperature range with a peak observed at 200-400 °C. The presence of both catalysts has eliminated the peak and shows similar profiles. The decreased amount of CH_4 could be ascribed to the functional groups chelated in the AC such as $-OH$, assisting the bond cleavage of pyrolytic vapors to form smaller compounds during the catalytic processes (Zhang et al., 2018a). The mass spectra of the SS is compared with SSHZSM5@1-1 and SSAC@1-1, and it is found that the catalysts affect the formation of the CO_2 ($m/z=44$), which is well depending on the pyrolysis temperature. SS arises from 200 to 600 °C with two peaks at 400 °C and 550 °C. The first peak is related to biodegradable and organic fractions while the second peak can be directed to secondary reactions of tar cracking and steam gasification in higher temperatures (Özsin and Pütün, 2017). The mixture of SS and catalysts have decreased the intensity at the nearly same rate for both catalysts till around 400 °C. Above 400°C, CO_2 levels decreased in the case of HZSM5 and increased in the case of SSAC@1-1. This observation can be ascribed to the carbonyl functional groups elimination and decarboxylation reactions from the surface of AC.

Additionally, the evolution of nitrogenous volatiles HCN ($m/z=27$) and NO_2 ($m/z=46$) generated during SS pyrolysis is also tracked. HCN is mainly generated from thermal cracking of nitrile-N compounds derived from protein in sludge (Tian et al., 2013). HCN is detected in a temperature range of 200-400 °C with a stronger evolution intensity for SS in comparison with presence of catalysts. The release of HCN is almost absent during SSAC@1-1 pyrolysis. For the case of NO_2 , the release behaviors from SSHZSM5@1-1 and SSAC@1-1 exhibited contribution of catalysts in contrast to pyrolysis of SS. The profiles against temperature revealed a drop in the intensity, especially for SSAC@1-1 catalytic pyrolysis which is in line with the literature (Gao et al., 2020). CH_3SH ($m/z= 48$) and SO_2 ($m/z= 64$) compounds are from thiol compounds during thermal decomposition and are extensively inhibited in both SSAC@1-1 and SSHZSM5@1-1 (Xu et al., 2017). No CH_3SH and SO_2 emissions are detected in case of SS, proposing that sulfur is captured by both catalysts. A similar observation is stated in another work devoted to the catalytic pyrolysis of SS with ACs (Chen et al., 2015). These results revealed that the presence of AC catalyst to some extent benefited the reduction of harmful pyrolytic gaseous during SS pyrolysis.





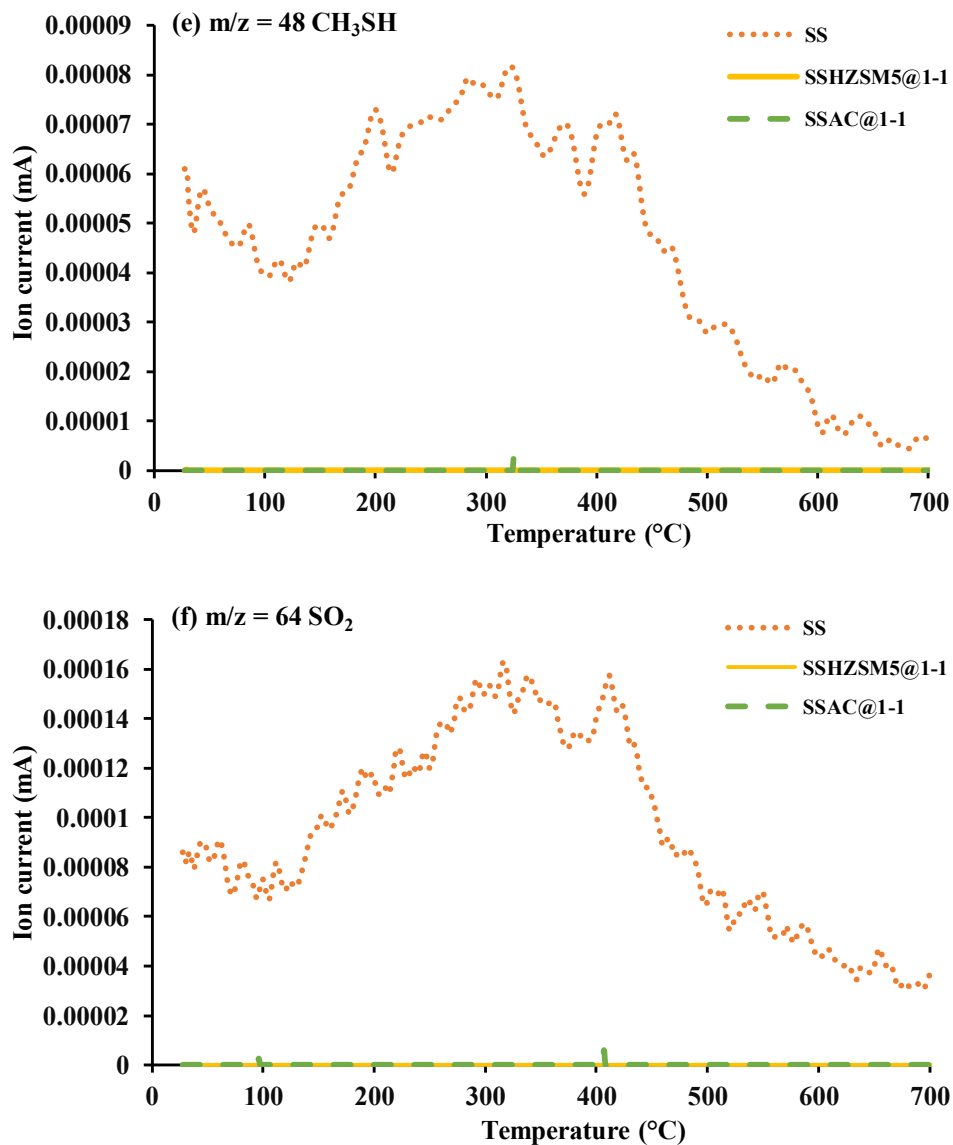


Fig. 5.8. Single ion current profiles monitored using MS during SS, SSHZSM5@1-1, and SSAC@1-1 pyrolysis.

5.3.5. Thermal decomposition prediction by ANN model

The training performance metrics of ANNs topologies with a different number of hidden layers and various numbers of neurons trained with LM are displayed in Table 5.4. The TGA data for catalytic pyrolysis of SSAC@1-1 is divided into three groups with 70% used for training, while the remaining 30% of data has been equally applied for the validation and testing. The total iterations are set to 1000 while the performance goal (MSE) is around 10^{-6} . In this study, the transfer function combination is selected based on the optimization of a variety of possibilities in

each hidden layer based on the computed MSEs, where the best combination is a nonlinear tangent sigmoid function (TANSIG) for the input and hidden layer and output layer follows a linear transfer function (PURELINE) in the network topology.

Table 5.4. Comparison of different ANN structure performances for SSAC@1-1.

| Model | Network topology | MSE | RMSE | MAE | MBE | R ² |
|----------|------------------|--------|--------|--------|---------|----------------|
| ANN3-1 | 3*1 | 0.1276 | 0.3576 | 0.2792 | -0.0016 | 0.9994 |
| ANN5-1 | 5*1 | 0.0134 | 0.1103 | 0.0703 | -0.0019 | 0.9999 |
| ANN7-1 | 7*1 | 0.0008 | 0.0292 | 0.0233 | 0.0000 | 0.9999 |
| ANN9-1 | 9*1 | 0.0012 | 0.0351 | 0.0270 | 0.0001 | 0.9999 |
| ANN3-3-1 | 3*3*1 | 0.1803 | 0.4303 | 0.3353 | 0.0597 | 0.9991 |
| ANN3-5-1 | 3*5*1 | 0.0311 | 0.1821 | 0.1342 | 0.0395 | 0.9998 |
| ANN3-7-1 | 3*7*1 | 0.0316 | 0.1821 | 0.1342 | 0.0395 | 0.9998 |
| ANN3-9-1 | 3*9*1 | 0.0306 | 0.1821 | 0.1340 | 0.0378 | 0.9998 |

The outputs are assessed to predict the TGA curves under the increase of temperature. According to the training performance assessment from Table 5.4, it is determined that ANN7-1 provided the best predictive power with the highest R² = 0.99 and the RMSE, MAE, and MBE values of 0.0292, 0.0233, and 0, respectively. The ANN7-1 incorporates a single hidden layer with 7 neurons. The ANN7-1 accomplished excellently to simulate the TGA (wt.%) curves for SSAC@1-1 and justified the accuracy of ANN calculation between the experimental data and predicted values for all catalytic pyrolysis zones (Fig. 5.9).

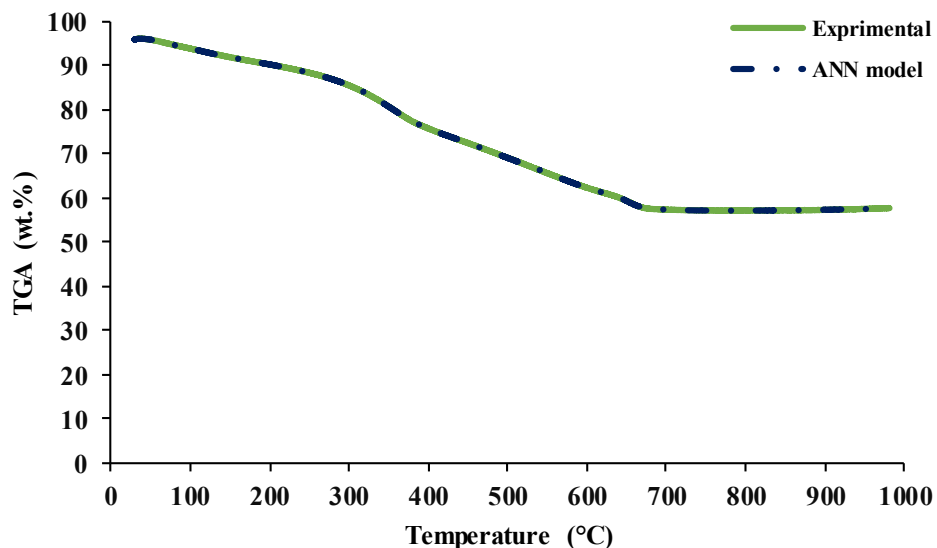


Fig. 5.9. Comparison of experimental and ANN predicted model (ANN7-1) for SSAC@1-1 catalytic pyrolysis.

5.3.6. Bio-oil analysis by GC/MS

Pyrolysis of SS is a very complex practice due to the mixtures in the SS bio-oil leading to a wide range of compounds in the spectrum as displayed in Fig. 5.10. The chemical composition of SS pyrolytic liquid obtained under the optimal condition (final temperature 550 °C, dwell time 60 min and $\beta = 30$ °C/min) from the pyrolyzer setup was analyzed for identification of organic compounds via GC/MS. Based on the spectrum data, 117 different compounds from different functional groups comprising of hydrocarbons (aliphatic or aromatic), oxygenated hydrocarbons (phenols, lipids, alcohols, acids, etc.) and nitrogenated compounds (nitriles, amines, etc.) were recorded. According to the definition of various transportation fuels, identified hydrocarbons were in the range of C4-C27 with 19.63% in the range of C4-C9; 66.21% in the range of C9-C18; and 14.49% in the range of C18-C27. Moreover, the bio-oil oxygen-containing compounds portion was more than 50% which is a detrimental property. It can affect stability and reduce the calorific value, thus, limiting the potential usage of the bio-oil for engine and turbine applications (Arazo et al., 2017; Hassan et al., 2016). Oxygenated compounds are mainly derived from extractives, lipids and polysaccharides in the SS (Alvarez et al., 2016). Besides, the presence of light aliphatic-aromatic compounds was around 0.71% in the derived bio-oil from SS pyrolysis and were mainly organic acids (e.g., butanoic acid, heptanoic acid, pentanoic acid, etc.). In contrast to other studies

in the literature, there is no straightforward conclusion due to the heterogeneity of the SS and the operating conditions selected by the different authors. Seemingly, many authors have also pointed the presence of oxygen- and nitrogen-containing compounds and higher molecular weight hydrocarbons (Tomasi Morgano et al., 2018; Trinh et al., 2013). As a result, the application of pyrolytic liquid as a fuel requires further improvements by cracking the large molecules into lower molecular weight species while reducing O and N-containing compounds.

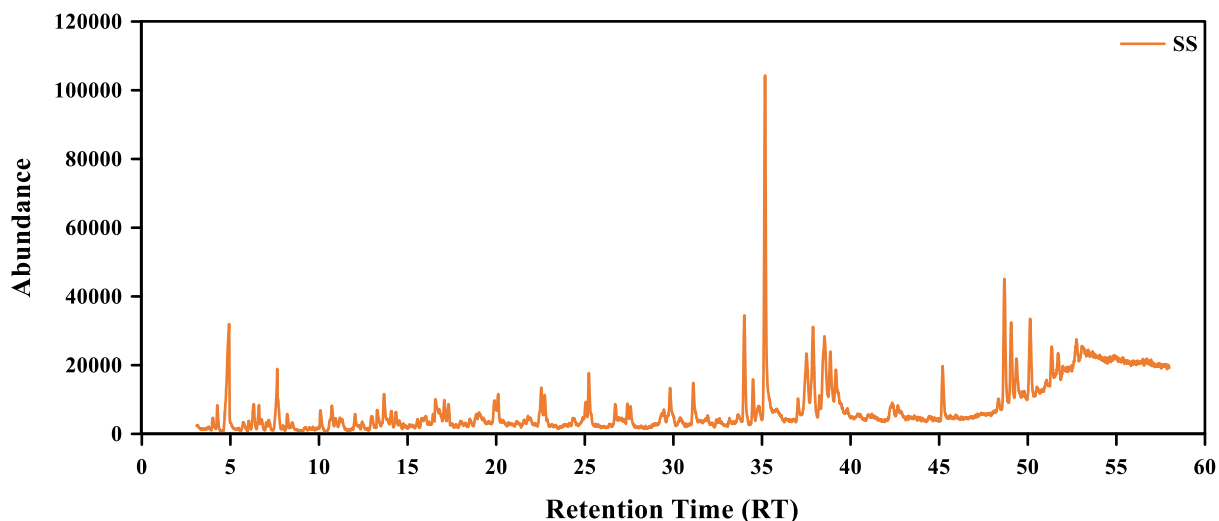


Fig. 5.10. Total ion chromatograms for pyrolysis of SS.

In this regard, to split heavier components into light organic oil and reduce oxygen-containing compounds, catalytic cracking process with different ratios of HZSM5 and AC has been investigated. Catalytic reforming is beneficial compared to the hydrodeoxygenation method since it does not require the addition of hydrogen and can be operated at atmospheric pressure (T. L. Liu et al., 2017). The chemical composition of the SSHZSM5@4-1 and SSAC@4-1 are shown in Fig. 5.11. The results revealed that the hydrocarbons were in the range of C4-C27 with 52.83% in the range of C4-C9; 32.8% in the range of C9-C18; and 14.38% in the range of C18-C27 for SSHZSM5@4-1. For the presence of AC catalyst, 66.26% were in the range of C4-C9; 26.11% in the range of C9-C18; and 5.61% in the range of C18-C27. The oxygenated compounds were 36.69% and 44.65% for SSHZSM5@4-1 and SSAC@4-1, respectively. Also, the proportion of value-added compounds was increased to 11% for both catalysts. The main value-added identified compounds were toluene, ethylbenzene, p-xylene and styrene. Although HZSM5 and AC had

improvements in the quality of bio-oil to some extent, still the amount of oxygen-containing compounds were not acceptable for the application of bio-oil as a fuel.

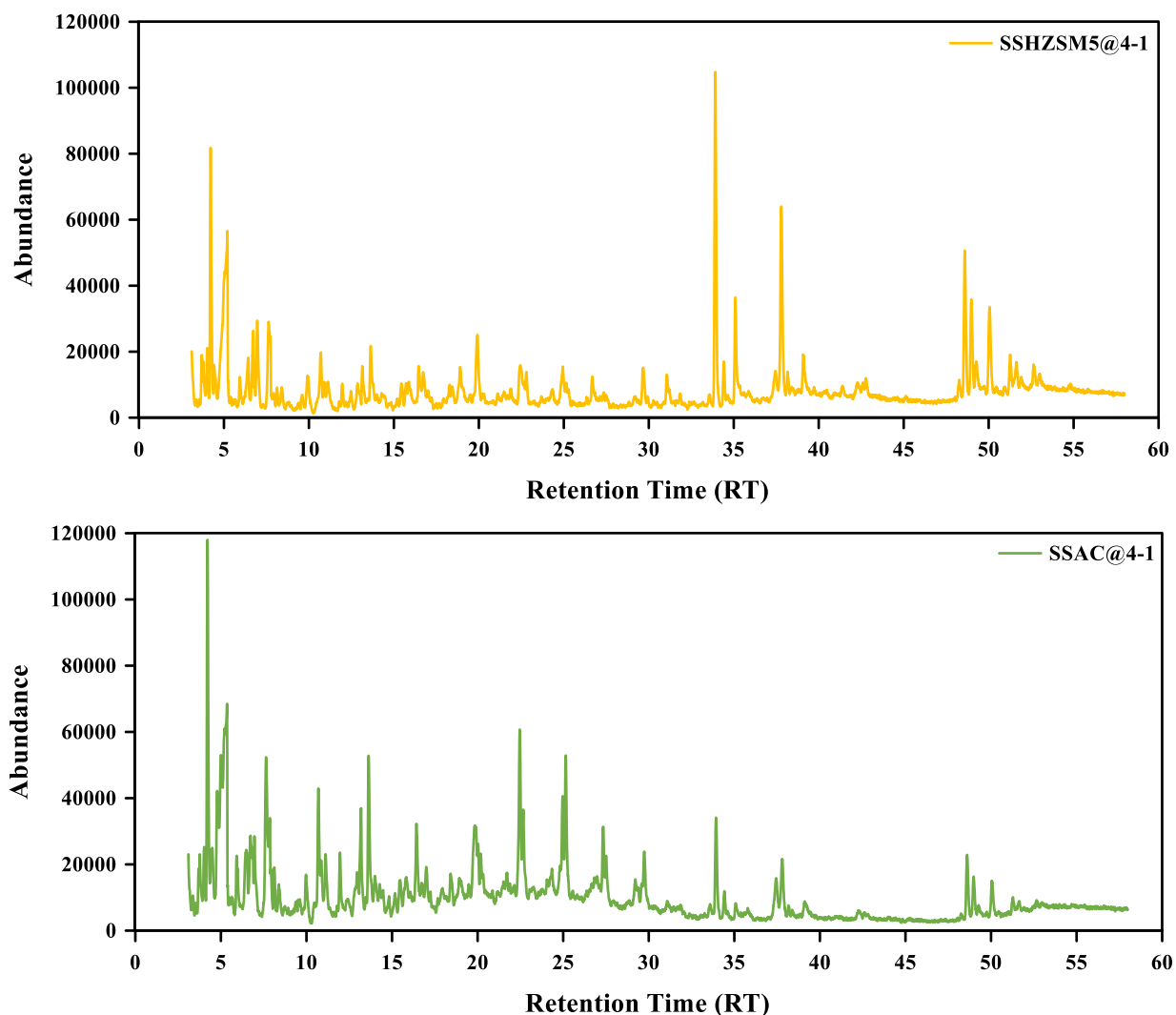


Fig. 5.11. Total ion chromatograms for catalytic pyrolysis of SSHZSM5@4-1 and SSAC@4-1.

With the increase of catalyst to feed ratio from 4:1 to 2:1 a considerable improvement in the number of carbon atoms was not identified, as displayed in Fig 5.12. However, oxygen removal was enhanced. The proportion of oxygenated compounds dropped to 20.51% and 26.76% for SSHZSM5@2-1 and SSAC@2-1, respectively. On the other hand, the production of value-added species increased to around 22% and 14% for SSHZSM5@2-1 and SSAC@2-1, respectively. The major components of bio-oils were toluene, ethylbenzene, p-xylene and benzene, 1-ethyl-2-methyl-. This is in agreement with previous research on microwave-assisted pyrolysis of SS over

HZSM5 presenting that the organics derived in the pyrolysis could be deoxygenated and cracked for the production of aromatics (Xie et al., 2014). The reaction mechanism and pathways can be attributed to several oxygenated compounds produced during the catalytic pyrolysis of SS which are intermediates in the production of aromatics. When the intermediates passed through the pores texture of HZSM-5 and AC catalysts, some of them are altered to single-ring aromatic products through a series of oligomerization, decarboxylation, decarbonylation and dehydration reactions (S. Liu et al., 2017).

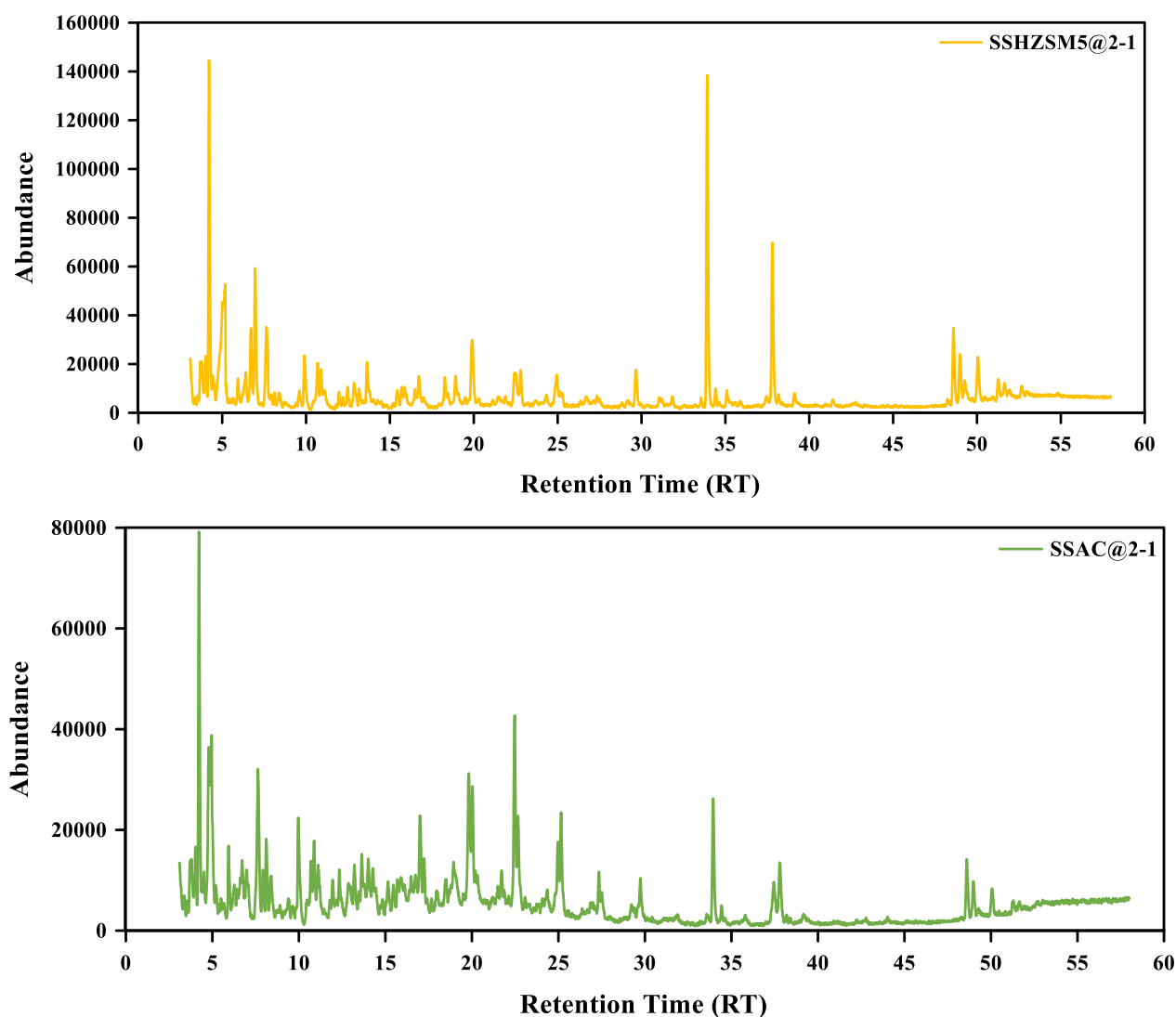


Fig. 5.12. Total ion chromatograms for catalytic pyrolysis of SSHZSM5@2-1 and SSAC@2-1.

The analysis of bio-oil components when the SS and catalyst ratios were in the same portion is shown in Fig. 5.13. For both catalysts, it was noticed that the carbon numbers were in

the range of C4-18 with around 73% in the range of C4-C9 and 27% in the range of C9-C18. This great range of hydrocarbon belongs to the jet fuel components (Zhang et al., 2019). Similarly, we speculated that the O-containing compounds dropped to 7.3% and 13.02% for SSHZSM5@1-1 and SSAC@1-1, respectively. In addition, the proportion of value-added chemicals in the bio-oils significantly increased to approximately 29% after catalytic cracking over HZSM5 and AC catalysts. The effect of catalysts on the formation of light hydrocarbons is related to their pore structure and acid sites (T. L. Liu et al., 2017). The long-chain hydrocarbons (e.g., acids, alcohols, ketones, etc.) were deoxygenated and cracked into C2–C9 olefins. Then, they are converted to benzene through a series of aromatization reactions and can be transformed to other aromatics through alkylation and isomerization reactions (Liu et al., 2019; Ren et al., 2014). The main light hydrocarbons detected in the liquid product of SSHZSM5@1-1 were toluene, ethylbenzene, p-xylene, cyclooctatetraene and benzene, 1-ethyl-2-methyl- and for SSAC@1-1 were toluene, octene, ethylbenzene, p-xylene and styrene. The higher performance of 1:1 ratio compared to 2:1 and 4:1 is probably due to higher surface contact between pyrolysis vapors and active acid sites of catalyst particles (Xie et al., 2015). Based on Fig. 5.1(b) presence of inherent metal species in the sludge-derived AC matrix is obvious. These transition metals on the surface of AC may react with the free radicals and reforming the volatiles (Wu et al., 2002). Moreover, abundant O-containing functional groups (see Fig. 5.2) on the surface of AC can form some acidic centers which bind to the negatively charged π electron system of fused aromatic hydrocarbons and activate the thermal cracking reactions of those compounds in bio-oil (Fu et al., 2018). Interestingly, proportions of nitrogenated components in the bio-oil of SSAC@1-1 were almost eliminated while for SSHZSM5@1-1 the portion was around 30%. This can be attributed to the presence of Ca and Fe elements in the AC which can transform the nitrogenous compounds into N_2 , however, more in-depth studies are required (Gao et al., 2020). Removal of nitrogenous compounds is one of the vital targets during the upgrading of SS-derived bio-oils since they can lead to release of NO_x emissions if burned as a fuel. According to the results, AC catalyst can be considered as an environmentally friendly alternative for HZSM5 substitution. Among the tested catalyst to feed ratios, the 1:1 split ratio can be considered as an optimum.

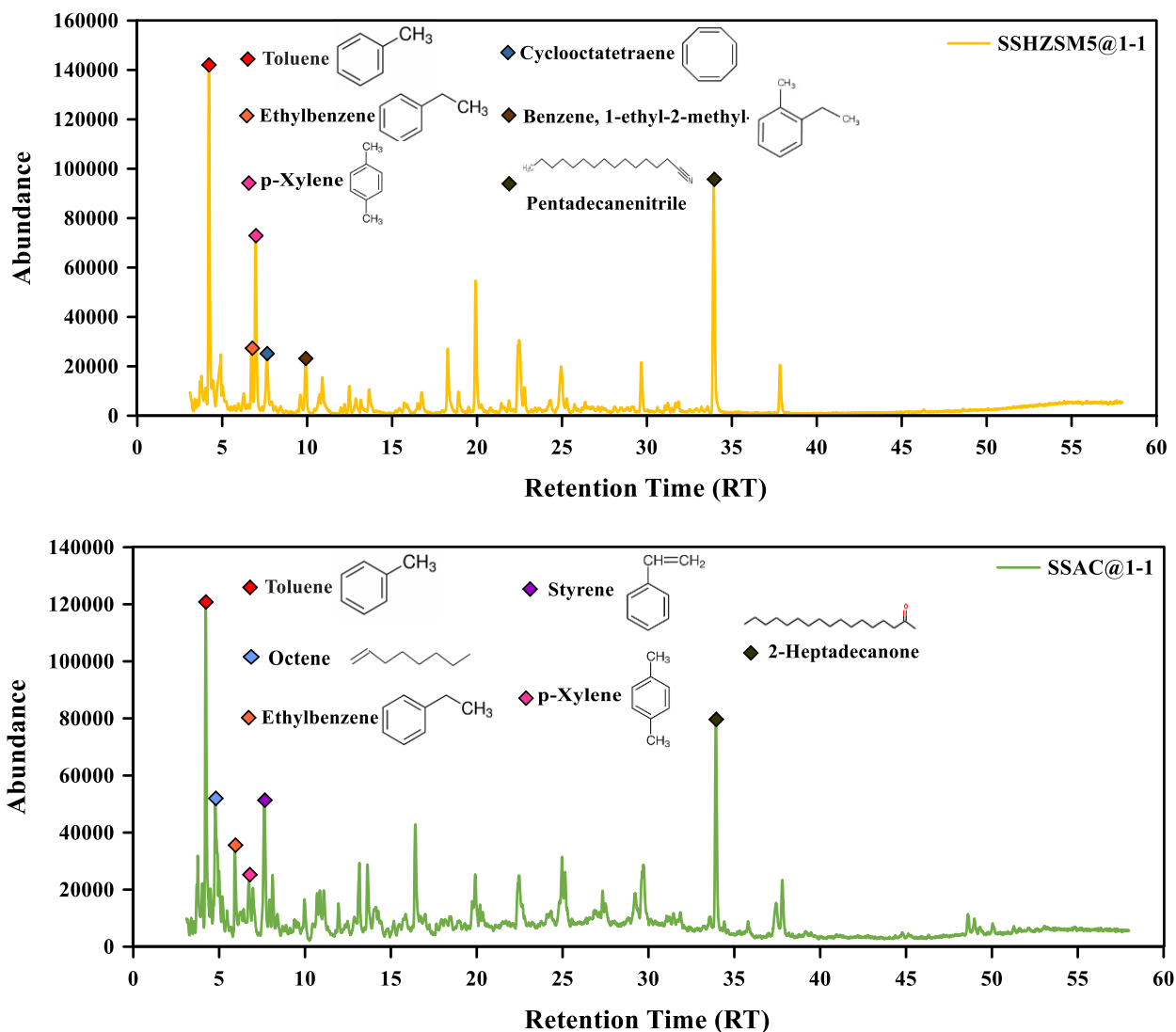


Fig. 5.13. Total ion chromatograms for catalytic pyrolysis of SSHZSM5@1-1 and SSAC@1-1.

5.4. Conclusion

In this study, non-catalytic and catalytic pyrolysis of SS have been analyzed by TGA-MS and GC/MS using commercial HZSM5 and sludge-derived AC catalysts. The novel developed AC catalyst shows promising performance by increasing reaction rate and reducing the energy required for the decomposition process. Also, presence of catalysts reduced the CH₄, HCN, CO₂ and NO₂ while eliminating CH₃SH and SO₂ gaseous evolving during pyrolysis of SS. The optimal catalysts to feed ratio for upgrading bio-oil quality was 1:1. The presence of HZSM5 proved catalytic cracking of high-weight hydrocarbons to lighter species while removing oxygen-containing compounds. Besides the mentioned improvements, the fabricated AC catalyst was able to remove

nitrogenous compounds and showed more selectivity in value-added compounds. The characterization sludge-based AC manifested porous particles in which the presence of inherent metallic minerals and O-containing functional groups plays as active sites in the catalytic upgrading. The synthesis AC had a larger specific surface area and more active sites in contrast to HZSM5 resulting in better catalytic performance. However, further in-depth investigation for exploring the mechanism pathways of the deoxygenation and denitrogenation of the process is recommended. Also, further investigations on the analysis of evolved gaseous during the activation process is recommended prior to the use of SS-based AC as a catalyst. Notably, an ANN method was further developed for the forecast of TGA profiles for catalytic pyrolysis. The results obtained from the ANN model are in good accordance with the experimental outcomes, depicting it as a reliable tool for the prediction of the TGA experimental data. Our findings would serve as a theoretical basis for future scale-up of the catalytic conversion of SS using sludge-based AC as a catalyst.

CHAPTER 6

DEVELOPMENT OF SLUDGE-BASED ACTIVATED CHAR SORBENT WITH ENHANCED HYDROPHOBICITY FOR OIL SPILL CLEANUP

6.1. Introduction

Oil spill incidents have occurred globally during the exploration/production and transportation process, bringing catastrophic environmental impacts on marine ecosystems and coastal areas (Motta et al., 2019). Despite advances in technologies and improved safety guidelines, accidental spills will continue to occur due to human errors, equipment malfunction, etc. Nevertheless, whenever an oil spill happens, it can represent a severe and challenging ecological problem. The environmental pollution of oil spills requires an urgent need to develop advanced material and methods to cleanup oil from the surface of water effectively, fast and affordable while mitigating the negative consequences of spilled oil (Li et al., 2014). To address these challenges, considerable efforts have been made to cleanup oils by employing different techniques, categorized as chemical methods (in situ burning, surfactants, dispersants and solidifiers), mechanical cleanups (barriers, booms, skimmers, synthetic sorbents) and biological or bioremediation (use of micro-organisms to alter, transfer and breakdown the hydrocarbons of oil) (Thakkar et al., 2020).

Among the mentioned technics, physical recovery of spilled oil by the use of sorbents remains a cornerstone in oil spill response, due to its effectiveness and proven ability to remove oil from the environment by absorbing, capturing and recovering the pollutant within a sorbent matrix (Bhardwaj and Bhaskarwar, 2018). The selection of an appropriate sorbent material plays a crucial role in oil/water remediation. In this case, various materials such as organic-inorganic hybrids (da Costa Cunha et al., 2019), polymers (Abirami et al., 2020), nanofibers (Karzar Jeddi et al., 2019), nanocomposites (Ieamviteevanich et al., 2020), silicas (Thakkar et al., 2020) and carbon-based natural materials (Ngaini et al., 2018) have been explored. Among these, natural carbon-based materials have drawn attention due to their biodegradability, approachability, affordability and safe disposal (Kandanelli et al., 2018; Nurliyana Che Mohamed Hussein et al., 2019). Accordingly, a stable carbon (C)-rich by-product, named char, generated through pyrolysis

of agricultural and forestry biomasses in an oxygen-limited environment have been tested in recent studies for oil spill removal (Ahamad et al., 2019; Kandaneli et al., 2018; Silvani et al., 2017). However, their widespread application is limited by poor hydrophobicity and oleophobicity, with unsatisfactory low oil sorption capacities (Tayeb et al., 2020). In addition, they face difficulties during separation and recycle from the aqueous system. Therefore, inexpensive sorbent materials with excellent hydrophobic and oleophilic properties along with facile and fast recovery processes are greatly demanded (Wang and Wang, 2019).

In recent decades, the volume of SS, generated from wastewater treatment plants, has considerably amplified due to the expansion of municipalities and industries. For instance, SS annual production in Canada is now around 4 million tons/year (dry base) (Lin et al., 2019). Management of this waste material has included investigations of its potential use in the production of char as an adsorbent for removing a large range of organic/inorganic contaminants from water and wastewater (Al-Malack and Dauda, 2017; Fan et al., 2017; Sizmur et al., 2017). The adsorption capacity of char was enhanced through chemical activation, due to the improvements in the pore structure, specific surface area and availability of hydroxyl (-OH) groups (Yan et al., 2020). Nonetheless, utilizing AC as a sorbent suffers some main drawbacks for oil spill treatments. The densities of the carbonaceous char and inorganic mineral regions are far more than the water, thus as pores take up water, it sinks quickly when exposed to water. Recently, modification of char with fatty acids (e.g., lauric acid) has drawn interest because it can reduce water penetration and avoiding the filling of AC pore volume with water (Navarathna et al., 2020). Meanwhile, substitution of hydroxyl groups with the alkyl chain from the lauric acid can provide greater sites for higher oil uptake capacity (Sidik et al., 2012). However, lauric acid (GHS classification: toxic to aquatic life, category 2) is toxic to the aquatic environment. In this study, modification with myristic acid (GHS classification: not a hazardous substance) has been considered as an “eco-friendly” option, since it is not toxic for aquatic life and its long chain of hydrocarbons may result in better hydrophobicity and oleophobicity properties.

Separation of sorbents after the oil sorption process from the aquatic system is an energy and time-consuming task. To surpass routine procedures such as filtration or centrifugation, magnetic property has been functionalized to the synthesized sorbents structure to facilitate fast recovery in the presence of a magnet (Ahamad et al., 2019; Raj and Joy, 2015). However, the complex and costly chemically developed magnetic sorbents often induce toxic responses from

aquatic organisms (Ahamad et al., 2019). Iron-based coagulants are widely used in wastewater treatment plants, resulting large amount of Fe-minerals incorporated in SS during wastewater treatment (Gu et al., 2018). The ferric ions within SS can be reduced to form magnetite during pyrolysis reactions in the optimized condition that result in magnetic properties (Cho et al., 2017). That could be beneficial in terms of sorbent recovery by the use of magnets (Ahamad et al., 2019; da Costa Cunha et al., 2019).

Keeping these merits of SS in our mind, in the present study, we aimed to synthesis an efficient and eco-friendly sorbent for oil spill cleanup with excellent hydrophobic and oleophilic properties with inherent magnetic function for the first time. Generally, SS can be directly transformed to AC via pyrolysis reaction with high surface area and abundant hydroxyl groups. The availability of the hydroxyl group permits surface modification with myristic acid to enhance hydrophobicity and sorption properties. Furthermore, Fe-minerals can be reduced to form magnetite during pyrolysis reactions. This process can theoretically produce highly efficient sorbent properties that can be recovered by the use of magnets to remove oil spills from surface waters. The influence of the pyrolysis reaction, surface modification on sorption performance and separation efficiency was examined in the laboratory for the removal of motor oil and light crude oil. The possibility of reusability was also investigated through five cycles. Considering the high performance, inexpensive precursor, green and facile synthetic procedure, the modified AC is believed to be beneficial for the oil spill cleanup.

6.2. Materials and methods

6.2.1. Materials

The SS used in this study is subjected to conditioning with a polyvalent cation (iron and aluminum salts) in the treatment plant. Commercially available motor oil product and light crude oil were employed as probing liquids for oil sorption studies. The chemicals (Fisher Scientific, USA) used in this research were analytical grade and used as received without further purification. De-ionized (DI) water was obtained from Millipore Integral 10 water system (Millipore, Billerica, USA) and used in all experiments. The SS was carbonized in a tubular pyrolysis reactor (Lindberg/Blue M Mini-Mite™ Tube Furnaces, Thermo Scientific, USA) as indicated in Fig 3.1.

6.2.2. Sorbent synthesis

The AC derived from SS was then modified with myristic acid and initiated as MAC-SS (Sidik et al., 2012). Briefly, a 2 g portion of AC was slurried with 1 g myristic acid and dissolved in a warm aqueous methanol solution (70 °C, 10% (v/v)) and stirred for 6 hr. Then, the solution was vacuum-filtered to remove the MAC-SS. Finally, crude MAC-SS was washed several times with n-hexane to remove excess myristic acid before being oven-dried at 105 °C overnight.

6.2.3. Characterization of sorbent

The surface area of MAC-SS was measured from N₂ isotherms at -196.15 °C using a gas sorption analyzer (NOVA-1200; Quantachrome Corp., USA). The MAC-SS was degassed for 12 h under inert conditions at 200 °C before applying adsorption measurements. The N₂ adsorbed per gram of samples schemed versus the relative vapor pressure (P/P₀) of N₂, and the data were fitted to the BET equation to compute surface area. FT-IR spectroscopy (Thermo Scientific, 4700, USA) was employed to evaluate the functional groups of the samples. The infrared spectra were collected in a range of 4000–500 cm⁻¹ with a resolution of 8 cm⁻¹. The samples were characterized by X-ray powder diffraction (XRD) (Bruker AXS D-8 Advance, USA) using Cu K α radiation ($\lambda = 1.54 \text{ \AA}$ X-rays) to inspect the crystalline patterns in the 2 θ range of 5–90°. The morphology of MAC-SS was examined using an FEI Quanta 450 SEM (acquired by Thermo Fisher Scientific, USA), operating at 25 kV in a vacuum. The static water and oil contact angle (CA) data was measured on a VCA optima instrument (AST Products, Inc., Billerica, MA, USA) at ambient temperature, using a sessile water drop method with 2 μ L liquid drop. The optical image used in this paper was taken by a Nikon (D700) digital camera and the surface color was modified for better observation of the droplet. All measurements were performed in triplicate.

6.2.4. Oil sorption capacity

In this research, two parallel well-known analytical procedures were carried out in order to study the sorption capacity of the AC and MAC-SS against motor oil and light crude oil (Ahamad et al., 2019; Li et al., 2014). The properties of the studied oils for sorption capacity are summarized in Table 6.1.

Table 6.1. Characteristics of oil samples studied for sorption.

| Oil Sample | Viscosity (cP, at 25°C) | API (g/mL, at 25 °C) |
|-----------------|-------------------------|----------------------|
| Motor oil | 219.2 | 0.89 |
| Light crude oil | 6.3 | 0.87 |

Both procedures were carried out at an ambient temperature and pH value of 6.5. Noteworthy, the variation in pH, temperature and aqueous condition (i.e., DI or saline water) does not affect the oil sorption process considerably according to different studies (Kandanelli et al., 2018; Navarathna et al., 2020). In this case, no adjustment has been carried out regarding the pH and temperature. Besides, DI water has been used as the simulated water body. In the first procedure, according to ASTM F726-12, 25 mL of deionized water and 2 g of oil was added to a 50 mL glass beaker and a mesh screen basket was depressed at the bottom of the beaker before adding the oil samples in a static condition (Demirel Bayık and Altın, 2017). The mesh size for filtration was less than 150 μ . Then, 0.15 g of sorbent was sprinkled onto the surface oil layer and allowed to equilibrate for 60 s, without agitation or swirling, collected by the mesh screen and the sorbent was left to drain for 30 ± 3 s. The sorption capacity was determined as the ratio of the adsorbed amount of oil to the initial dry weight of the sorbent with the following equation (g oil/g dry sorbent):

$$\text{Oil-sorption capacity (g/g)} = M_t - M_s / M_s \quad (6.1)$$

where M_s and M_t are the mass of the initial dry sorbent material and total mass of the sorbent samples after oil adsorption, respectively.

Naturally, char derived from SS has a magnetic property to ensure the easy recovery of the sorbent via the application of an external magnetic field. This property is based on the presence of a high amount of Fe in raw SS (see Table 3.1) making the AC magnetic during the pyrolysis process (Komlev et al., 2018). Thus, in the second procedure after sprinkling the sorbent on top of the oil after 60 s the sorbent with adsorbed oil was recovered using an external magnet and weighted under the static condition as depicted in Fig. 6.1(a-d). The sorption capacity was measured using Eq. 6.1. The maximum variation in the oil uptake capacity between the two procedures from the same type of oil was 0.5 and their mean values were presented in the outcomes

in this research. Modification with myristic acid prevented water to occupy the AC pore volume, thus, the MAC-SS floated on the water surface as illustrated in Fig. 6.1(e).

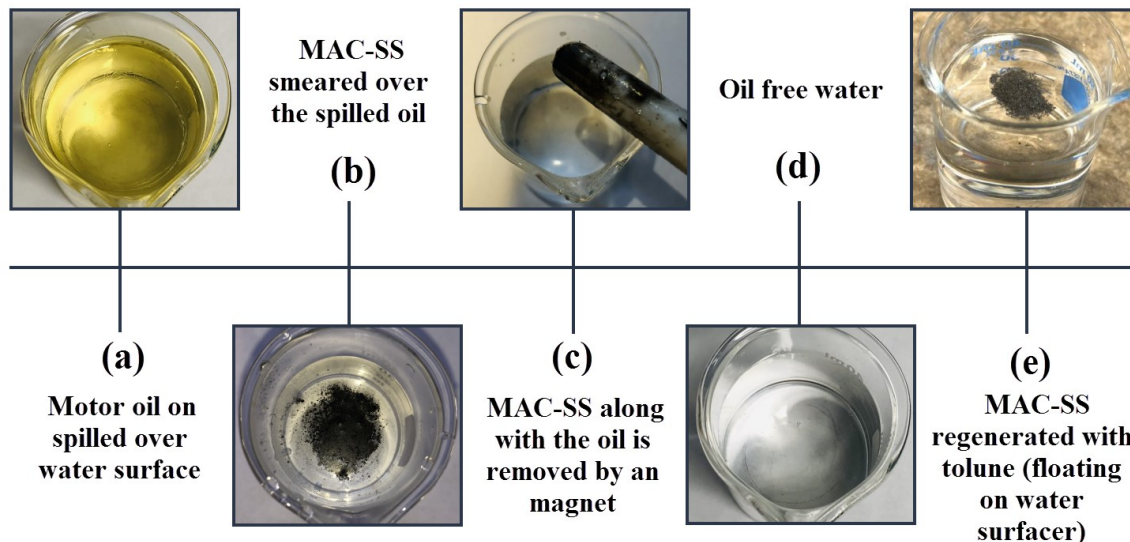


Fig. 6.1(a-e). Schematic depiction of oil removal from the water surface with MAC-SS sorbent via magnet bar.

6.2.5. Reusability

The reusability of sorbents plays a crucial role in pollution control and environmental protection (Bhardwaj and Bhaskarwar, 2018; Ieamviteevanich et al., 2020). Accordingly, repeated absorption–desorption cycles of oils were performed to evaluate the reusability of fabricated MAC-SS based on solvent extraction. This approach is previously conducted as an efficient technique for oil adsorbed coconut shell-based activated carbon-iron oxide magnetic nanocomposite (Raj and Joy, 2015). In this technique, the oil forms the sorbent was desorbed using ethanol and when all the oil was desorbed, the sorbent was dried in an oven at 120 °C to remove adsorbed ethanol and reuse for further sorption tests. In this study, we have repeated the absorption–desorption process 5 times for both types of oils. Weight gains were noted after each sorption cycle, and the recovered oil weights were documented.

6.3. Results and discussion

6.3.1. Detailed characterization of sorbent

6.3.1.1. FT-IR analysis

The functional groups detectable on the IR spectrum could verify the possible functional groups involved in bonding interaction between AC and myristic acid. Therefore, to identify the functional groups formed on the surface of both samples, FT-IR analyses have been conducted and represented in Fig. 6.2. The spectra of the examined AC exhibited two bands in the 2000-4000 cm^{-1} range. The broadband centered at about 3400 cm^{-1} can be ascribed to the stretching vibration of intra- and inter-molecular hydrogen-bonded (O-H) stretching (Zielińska et al., 2015; Zubrik et al., 2017). The small band at about 2900 cm^{-1} is ascribed to the C-H symmetric and asymmetric vibration mode of ethyl and methylene groups (Lin et al., 2012). However, two intense peaks have appeared between 2800-2900 cm^{-1} for MAC-SS. The double-peak phenomenon is attributed to the C-H asymmetric stretching of carboxylic and carboxylate groups, indicating the successful decoration of AC with myristic acid (Sidik et al., 2012). Between 1400-1700 cm^{-1} for MAC-SS two intense peaks can be observed in comparison to AC. The peak at 1410 cm^{-1} represents the C-H bending vibration mode and 1610 cm^{-1} is attributed to the C=O stretching of the carbonyl group (Yang et al., 2019). Both peaks are linked to myristic acid structure. The strongest peaks for both samples are around 1000 cm^{-1} assigned to the C-O stretching vibration (Antunes et al., 2017). The peaks near 870 cm^{-1} can be allocated to the alkene -C=C group for both AC and MAC-SS (Zhang et al., 2018a).

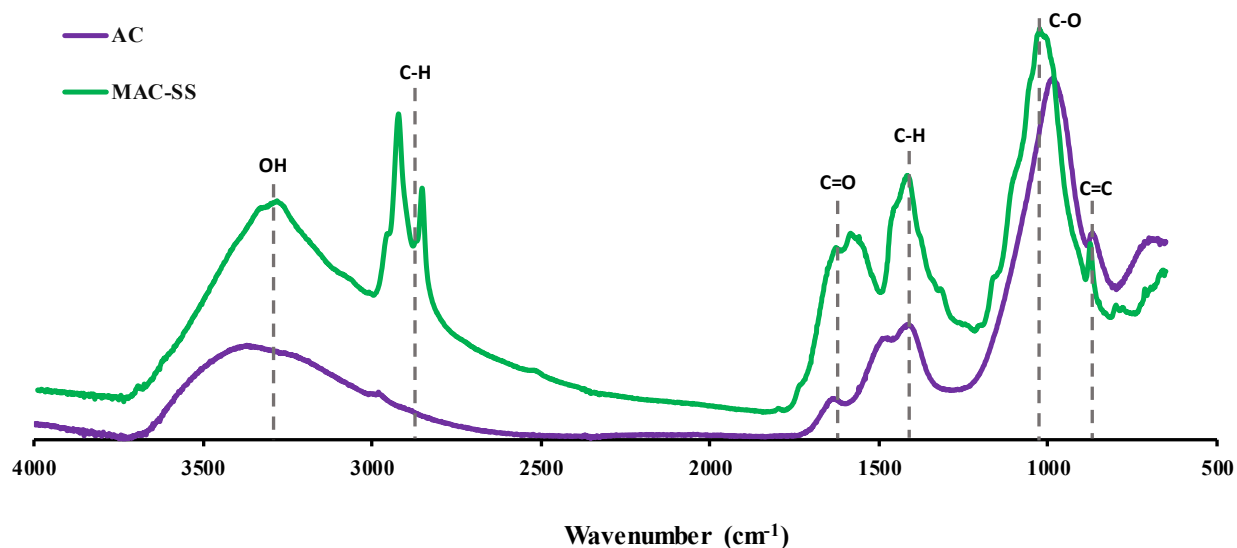


Fig. 6.2. FT-IR analysis of AC and MAC-SS.

6.3.1.2. X-ray diffraction

The sharp diffraction peaks illustrated in Fig. 6.3, indicated good crystallinity of the AC and MAC-SS particles. The expected sharp peak of myristic acid at 2Θ of 7.66° was observed for MAC-SS, confirming the success in modification of AC with myristic acid (Navarathna et al., 2020). The XRD pattern of AC and MAC-SS shows a broad and low-intensity Bragg diffraction peak between $2\Theta = 20\text{-}35^\circ$ which is ascribed to amorphous carbon matrix (002) orientation (Ahamad et al., 2019; Shokry et al., 2020). The low intensity with a broad peak is evidence of nanoscale carbon particles which is in agreement with the results of (Beshkar et al., 2017). Correspondingly, at $2\Theta = 44.65^\circ$ an overlapped peak was observed for the materials indicating graphite (101) planes (Kandanelli et al., 2018). Higher intensity of (002) compared to the (101) plane can be an indicator of the porous structure of the materials (Komlev et al., 2018). As evidenced by Zhu and coworkers, high pyrolytic temperatures (above 600°C) are beneficial for spinal Fe_3O_4 crystalline evolution (Zhu et al., 2019). The XRD pattern certifies the presence of cubic phase of Fe_3O_4 in the materials based on the observed peaks at approximately $2\Theta = 30.97, 35.04, 43.7$ and 65 which are attributed to the (220), (311), (400) and (440) lattice planes, respectively (Cho et al., 2017; Di Iorio et al., 2019). These outcomes are evident that the ferric hydroxides are decomposed to form magnetic Fe_3O_4 particles during the activation pyrolysis reaction and are in line with (Gu et al., 2018) investigation.

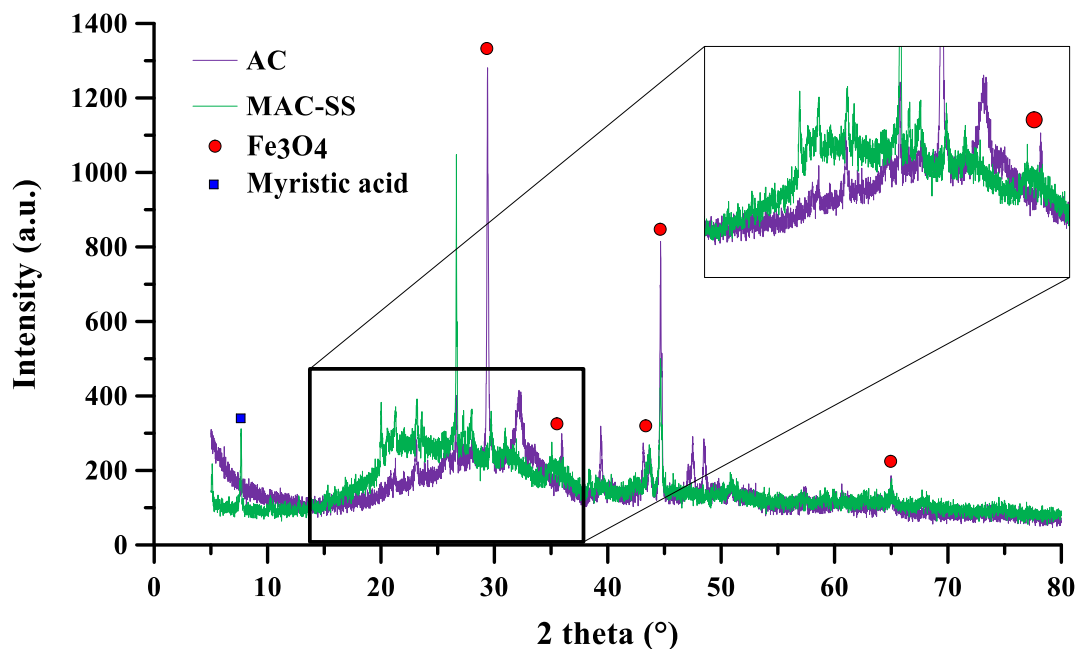


Fig. 6.3. XRD patterns of AC and MAC-SS.

6.3.1.3. Morphology and textural studies

A preliminary idea about the structure of the sorbent surface was elucidated by SEM images. As displayed in Fig. 6.4, micropore sizes were observed in the prepared sorbent. MAC-SS is composed of agglomerated carbon particles with a size ranging from tens to hundreds of nanometers in diameter. Moreover, the BET surface area was found as 899.33 m²/g for AC which is comparable to the values of other organic-based sorbents used for oil recovery in literature such as date palm pits (Ahamad et al., 2019), Douglas fir (Navarathna et al., 2020) and coconut shell (Raj and Joy, 2015).

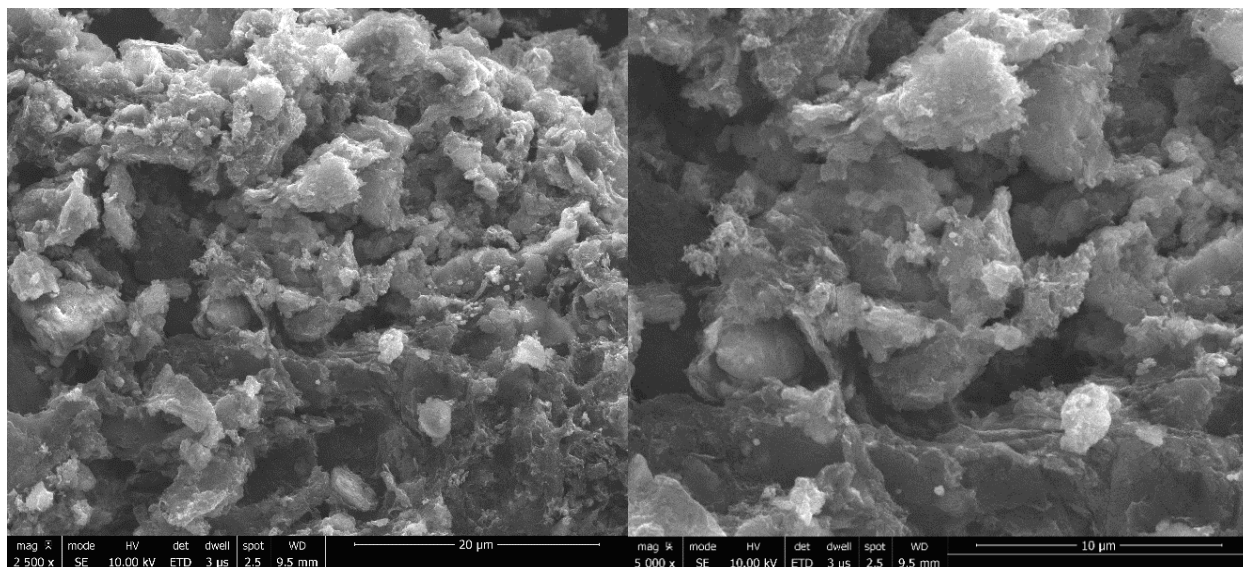


Fig. 6.4. SEM spectra of MAC-SS.

6.3.1.4. Contact angle measurements

The intrinsic hydrophobicity of a sorbent is critical for water/oil separation. Basically, a hydrophobic surface has a strong ability to repel water. Naturally, a water drop can easily roll off from lotus leaves without wetting them due to its no adhesive properties. This phenomenon must be addressed for developing sorbents with the purpose of oil spill recovery applications. The water CA values for AC and MAC-SS are displayed in Table 6.2. Surfaces with a water CA in the range of 90-150° are considered hydrophobic and over 150° superhydrophobic (Beshkar et al., 2017). There is evidence that the production of char at higher temperatures has fewer polar functional groups and greater hydrophobicity (Zhang et al., 2020). Consistent with that, AC had a hydrophobic CA value of around 122.4°. Despite its hydrophobicity, AC sinks rapidly when it's placed on the water surface.

Table 6.2. CA measurement for MAC-SS and reference data.

| Base sample | Preparation process | CA | Ref. |
|-------------------|---|--------------------------|---------------------------|
| Douglas fir chips | Char from gasification; Lauric acid modification; Magnetite with Fe ₂ O ₃ . | 135.9 ± 5.5 ^a | (Navarathna et al., 2020) |
| Date palm pits | Char from pyrolysis; Magnetite with Fe ₂ O ₃ . | 148° | (Ahamad et al., 2019) |
| Winter melon | Char from hydrothermal and post- pyrolysis. | 135° | (Li et al., 2014) |
| Sewage sludge | Activated char from pyrolysis. | 122.4°± 3.8 ^a | Present study |
| | Activated char from pyrolysis; Myristic acid modification. | 152.2°± 3.2 ^b | |

^a CA is based on the average of 5 measurements with a standard deviation of 3.8.

^b CA is based on the average of 5 measurements with a standard deviation of 3.2.

Interestingly, the water droplet takes a spherical shape when deposited on the MAC-SS sorbent and instantly bounces off the surface, indicating disfavor towards the water as pictorial representation is indicated in Fig. 6.5(a). The CA image of MAC-SS is shown in Fig. 6.5(b) inset, where a water droplet (size 2 mm) deposited on the MAC-SS surface, is almost perfectly spherical with a CA of about 152.2° verifying superhydrophobicity property. To further confirm the superhydrophobicity of MAC-SS, once it was introduced on the water surface it remained buoyant and did not sink (see Fig. 6.1(e)). The MAC-SS continued floating for at least 4 weeks before some of the sorbent particles started descending. The phenomena can be explained due to the carboxylic acid groups attracted to hydroxyl functions on AC surface. This makes the hydrocarbon chains of myristic acid (CH₃(CH₂)₁₂COOH) bulging from the surface where it would block water access to the surface and into the AC pore structure. The CA measurements of AC and MAC-SS have been compared with other biomass-derived sorbents in the literature (see Table 6.2). It's clear from Table 6.2 that MAC-SS has higher CA in contrast to other materials due to the modification process.

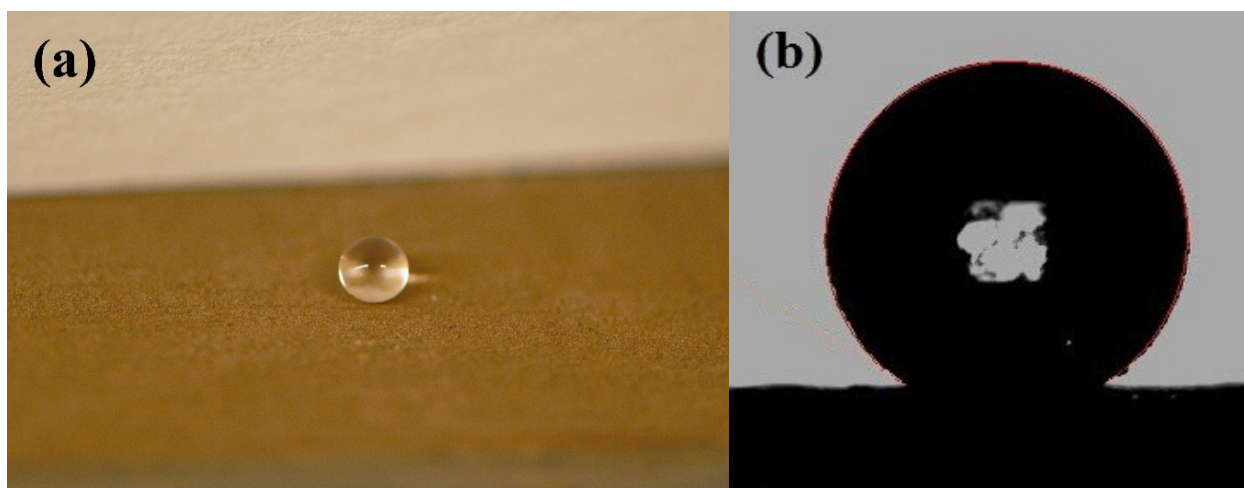


Fig. 6.5. (a) Optical image of a water droplet with spherical shape on MAC-SS surface, (b) CA of $152.2^{\circ} \pm 3.2$. h

By contrast, when oil droplet was deposited on the MAC-SS surface, they spread quickly on the surface and permeated it thoroughly, exhibiting MAC-SS excellent oleophilic property. Fig. 6.6 shows the CA 0° of using motor oil, resulting in a high sorption capacity. It should be noted that CA measurement time was within 10 s of contact of motor oil with the surface of sorbent which proves the hasty sorption process of the MAC-SS.

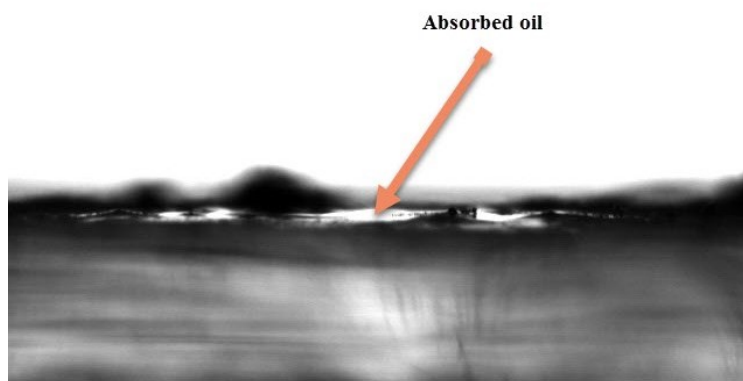


Fig. 6.6. The oleophilic surface of MAC-SS which the motor oil spread has penetrated the inner pores of the MAC-SS with a CA of 0° .

6.3.2. Sorption capacity studies

To study the sorption efficiency of AC and MAC-SS quantitatively, motor oil and light crude oil were selected. These materials are common pollutants in our daily lives as well as from

industry. As displayed in Table 6.3, the sorption capacity in DI water under static condition indicated uptake capacity of 6.3 g motor oil/g and 8.4 crude oil/g for AC and 8.5 g motor oil/g and 10.7 g crude oil/g for MAC-SS based on an average of 6 uptake experiment, 3 experiments with screen and 3 experiments with magnet removal. The difference in sorption capacities of the oils can be accredited to their API gravity which results in a higher pore diffusion for crude oil. In general, AC and MAC-SS can remove oils at approximately 8–10 times their initial weights. The sorption capacity of MAC-SS has been enhanced by myristic acid decoration on the surface. It is greater than those of biomass-derived char sorbents, such as maple, coconut shell, pinewood rice husk and wood chips as compared in Table 6.3. The explanation can be contributed to the effectiveness of myristic acid by enhancing the affinity of MAC-SS to adsorb oil (Sidik et al., 2012). The deposition of myristic acid on the surface of the AC leads to a rich alkyl chain that promotes the non-polar layer on the AC surface. These hydrophobic tails grant more contact areas and sites for oil adsorption. It must be mentioned, the sorption capacity of MAC-SS for motor and crude oil is not the highest ever reported such as polymers (Ieamviteevanich et al., 2020) and zeolites (Zhao et al., 2020). However, it has the benefit of the low-cost and eco-friendly synthetic procedure.

Table 6.3. Oil sorption capacity of AC and MAC-SS in comparison to other char-based sorbents.

| Sorbent | Type of oil | Sorption capacity (g/g) | Ref. |
|--------------------|-----------------|-------------------------|-------------------------------|
| Maple char | Crude oil | 3.80 | (Nguyen and Pignatello, 2013) |
| Coconut-shell char | Motor oil | 3.01 | (Raj and Joy, 2015) |
| Raw wheat char | Motor oil | 5.64 | (Tijani et al., 2016) |
| Pinewood char | - | 0.70 | (Silvani et al., 2017) |
| Wood chips char | Crude oil | 6.87 | (Navarathna et al., 2020) |
| Rice husk char | Motor oil | 7.50 | (Angelova et al., 2011) |
| AC | Light crude oil | 6.00 | Present study |
| | Motor oil | 6.30 | |
| | Light crude oil | 8.40 | |
| MAC-SS | Motor oil | 8.50 | |
| | Light crude oil | 10.70 | |

6.3.3. Sorbent reusability

Recovery of the adsorbed oil and reuse of the sorbent must be taken into account after uptake and removal from water for MAC-SS. The results of sorption capacity for 5 repeating cycles to study the reusability of MAC-SS for motor oil and light crude oil are displayed in Fig. 6.7. The recyclable sorption behavior of MAC-SS for both oils is similar. A slight decrease in the oil uptake was observed in the first three cycles, then no obvious change in the sorption capacity of MAC-SS can be noted. The same behavior has also been reported for other organic-based sorbents such as esterified cellulosic sago waste (Ngaini et al., 2018), banana peel (Alaa El-Din et al., 2018), coconut shell based AC (Raj and Joy, 2015), carbon aerogel from winter melon (Li et al., 2014) and commercial char (Navarathna et al., 2020). MAC-SS motor oil uptake for the first three cycles was 8.5, 7.53 and 7.1 g/g, respectively, and for light crude oil was 10.7, 9.8 and 9.1 g/g, respectively. The oil sorption capacity goes down with recycling cycles which can be attributed to a partial loss of myristic acid during ethanol stripping. In addition, charring of oil molecules and/or ethanol trapped on surfaces and pores structure of the sorbent may result in a decrease in the porosity after the first cycle (Raj and Joy, 2015). Although the sorption capacity lessened after the first cycle, it remains almost constant from the third cycle onwards and the rate is still promising in contrast to the previously reported sorbents (Demirel Bayık and Altın, 2017; Ieamviteevanich et al., 2020). Overall, a minor difference was observed in both sorption capacities of the motor oil and light crude oil onto the MAC-SS. Alternative methods such as distillation also can be carried out for the regeneration of sorbent with the advantage of harvesting the oil.

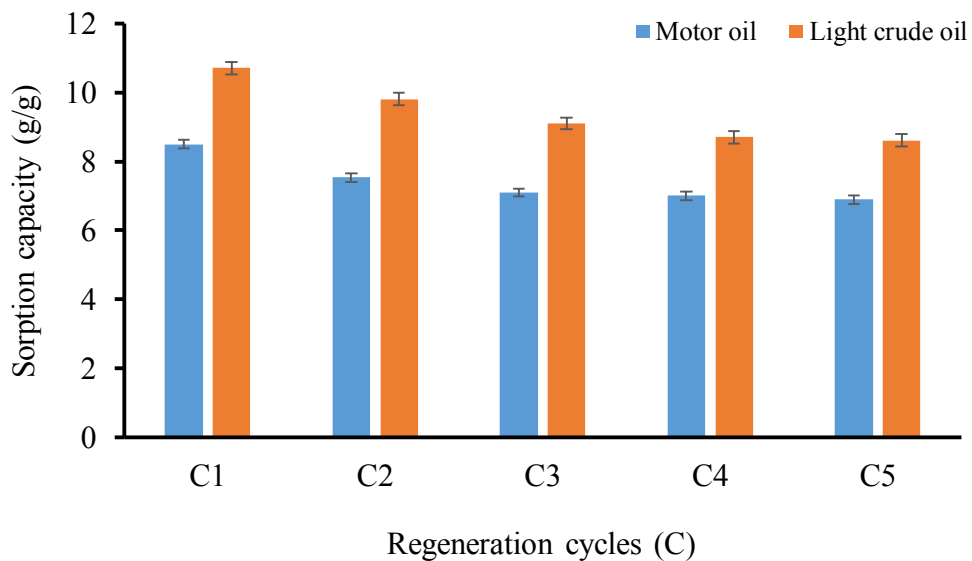


Fig. 6.7. Variation in the sorption capacity of MAC-SS (g/g) on recycling of motor oil and light crude oil.

6.4. Conclusions

This work explores, for the first time, the potential of utilizing SS waste as a precursor for sorbent synthesis through pyrolysis reaction and surface modification with myristic acid as an integrated approach from the perspective of environmental sustainability and oil spill cleanup. The magnetic AC production was successfully carried out and was supported by XRD analysis. Meanwhile, the presence of hydroxyl groups on the surface of AC was confirmed by FT-IR making surface modification with myristic acid applicable. The developed MAC-SS sorbent revealed a superhydrophobic and superoleophobic property affirmed by water CA of 152.2 and oil CA of 0°. The oleophilic property resulted in high sorption capacity for spill oils 8.5 and 10.7 g/g for motor oil and light crude oil, respectively, from water solution. The recycling and recovery studies with ethanol stripping supported the reuse of the sorbent up to at least 5 cycles. The innovative strategy of this work can further be extended to the broader development of sorbents by coating the material on stainless mesh or creation of three-dimensional network structured biocomposites

CHAPTER 7

CONCLUSION AND FUTURE WORK

7.1. Overall conclusion

The main purpose of the research work presented in this dissertation is to provide scientific reference and technical support for the research and further development of pyrolysis technology for SS waste processing for different applications that can combat environmental problems. Using pyrolysis reaction, SS waste resources with low value can be converted into clean and high energy density value-added products including bio-oil and char as a sustainable approach. To examine the objectives of this research, a pyrolysis reactor was designed and built for the experiments. Also, the thermal behaviors and reaction kinetics of co-pyrolysis and catalytic pyrolysis were investigated using TGA to elucidate their reaction mechanisms. As to co-pyrolysis, for the first time, SS was mixed with LDPE to increase the overall EHI value of the feedstock. LDPE proved to be a good hydrogen supplier to increase the overall efficiency of the process. The reaction resulted in a significant synergistic effect between the materials. In addition, kinetic and thermodynamic parameters were evaluated which their knowledge will provide referential values to describe the co-pyrolytic of SS and LDPE for bioenergy application.

Besides its low cost and availability, the major advantage of SS over other sources of biomasses is its high inherent metallic containing. This feature has been considered to extend the application of sludge-based char for the synthesis of highly performant catalysts and advanced sorbents for oil spill cleanup applications. In this thesis, several pyrolysis pathways for non-catalytic and catalytic pyrolysis of SS over sludge-derived AC were postulated by analysis and identification of pyrolysis products. Also, a comparison between HZSM5 and sludge-derived AC catalyst, as a green and efficient alternative, demonstrated high performance, especially for upgrading bio-oil composition and removing harmful gases. We have also investigated the potential conversion of the Fe-minerals via pyrolysis to magnetic sorbents that can be easily recovered from the contaminated media by application of an external magnetic field. Further modification of the sludge-based AC with myristic acid enhanced the sorption capacity and allowed the material to float on the water surface. Overall, the solid residue from pyrolysis of SS

showed to be an eco-friendly and efficient material with various applications which can be developed as an alternative to energy-intensive materials investigated in previous studies.

7.2. Contribution of research

The research work presented in this dissertation offers preliminary insight into the extension of SS pyrolysis application. The general contributions of the present work are either published or submitted and can be pointed out as:

- The pyrolysis setup was designed, built and optimized for the related experiments on converting biomass to value-added products.
- The co-pyrolysis of SS and LDPE was investigated for the first time. The process efficiency based on thermo-kinetics and thermodynamic parameters showed a positive synergic effect and proved the feasibility of the reaction (Zaker et al., 2020).
- The practice of catalytic pyrolysis over sludge-derived AC as an alternative to HZSM5 catalyst was investigated for the first time. As a result, the use of sludge-derived AC as an eco-friendly catalyst is promising for the production of bio-fuel (Zaker et al., 2021; Zaker and Chen, 2021).
- The evolution of a sludge-based AC for oil spill cleanup was explored as a green attempt to tackle environmental pollution.

7.3. Recommendations for future work

Based on the studies of this dissertation, the future research directions that should be undertaken are briefly presented as follows:

1. Long-chain wax (>C₂₃) is the main product in the bio-oil produced from the pyrolysis of plastics such as LDPE (Zhang et al., 2019). To fill this research gap, co-pyrolysis of SS with LDPE for biofuel production requires further investigations, especially, for the bio-oil quality and yield. Also, it is an interesting practice to integrate co-pyrolysis and catalytic pyrolysis processes with the aim of cracking the long-chain wax hydrocarbons to diesel (C₉–C₂₃) and jet fuel range (C₈–C₁₆).

2. Catalysts play a critical role in SS thermochemical conversion technology. The catalytic experiments in this research and most similar literature studies were examined in a bench-scale batch reactor. A detailed cost-benefit analysis, energy and mass balance needs to be performed to assess the feasibility of the process for scale-upping. Moreover, to realize the economical and efficient use of the SS catalytic pyrolysis technology a cost-effective and intelligent operation mode should be further studied. For instance, microwave heating can be considered as a practical approach based on our survey (Zaker et al., 2019) and similitude theory could be applied.

3. A challenge facing commercializing catalytic pyrolysis is deactivation and regeneration of the catalysts. The process is commonly plagued by the formation of coke on the catalyst surface. The coke could rapidly deactivate the catalyst and reduce its lifetime. Further studies concerning the deactivation and regeneration of AC catalysts are highly recommended. In addition, ex-situ catalytic pyrolysis, where catalysts are in a separated catalyst bed downstream of the pyrolysis reactor, requires auxiliary investigation. The benefit of this type of procedure is the ability to remove the catalyst to avoid contamination and to be easily separated and collected as a valuable byproduct. The catalyst lifetime can be prolonged and can be recycled and regenerated more easily, resulting in a reduction in costs.

4. In oil spill remediation, sorbents with modified properties have emerged. Many types of sorbents have been developed that performed well at laboratory scale, however, their durability in long-term applications has not been established yet. Considering the issue of applying sorbents in larger-scale aquatic environments the material can be easily diminished by harsh conditions such as the blow of wind. Therefore, larger and robust sorbents are required. In this context, coating the fabricated AC on a three-dimensional network structured nanocellulose sponge can be feasible practice. Nanocellulose is a natural fiber that can be extracted from the plant cell wall. Besides its physical advantages such as high surface area, lightweight, high porosity, and biodegradability; it has a large number of hydroxyl groups. These functional groups are favorable for surface modification with AC. Then, the as-prepared sponge can be fixed onto stainless steel mesh and applied to larger-scale applications.

References

- Abirami, A.L.A., Kumar, P.S., Prakash, D.G., Ravirajan, A., Umasankaran, A., Narayanan, P., Ravishankar, K., Kumar, C.S., Nagaraju, S., Reddy, K.P.J., 2020. Synthesis and application of porous oil-sorbent microspheres: Characterization, retention capacity and sorption kinetics. *Separation and Purification Technology* 234, 116095. <https://doi.org/10.1016/j.seppur.2019.116095>
- Adar, E., Karatop, B., Ince, M., Bilgili, M.S., 2016. Comparison of methods for sustainable energy management with sewage sludge in Turkey based on SWOT-FAHP analysis. *Renewable and Sustainable Energy Reviews* 62, 429–440. <https://doi.org/10.1016/j.rser.2016.05.007>
- Ahamad, T., Naushad, M., Ruksana, Alshehri, S.M., 2019. Ultra-fast spill oil recovery using a mesoporous lignin based nanocomposite prepared from date palm pits. *International Journal of Biological Macromolecules* 130, 139–147. <https://doi.org/10.1016/j.ijbiomac.2019.02.038>
- Ahmad, M.S., Mehmood, M.A., Al Ayed, O.S., Ye, G., Luo, H., Ibrahim, M., Rashid, U., Arbi Nehdi, I., Qadir, G., 2017a. Kinetic analyses and pyrolytic behavior of Para grass (*Urochloa mutica*) for its bioenergy potential. *Bioresource Technology* 224, 708–713. <https://doi.org/10.1016/j.biortech.2016.10.090>
- Ahmad, M.S., Mehmood, M.A., Liu, C.G., Tawab, A., Bai, F.W., Sakdaronnarong, C., Xu, J., Rahimuddin, S.A., Gull, M., 2018. Bioenergy potential of *Wolffia arrhiza* appraised through pyrolysis, kinetics, thermodynamics parameters and TG-FTIR-MS study of the evolved gases. *Bioresource Technology* 253, 297–303. <https://doi.org/10.1016/j.biortech.2018.01.033>
- Ahmad, M.S., Mehmood, M.A., Taqvi, S.T.H., Elkamel, A., Liu, C.G., Xu, J., Rahimuddin, S.A., Gull, M., 2017b. Pyrolysis, kinetics analysis, thermodynamics parameters and reaction mechanism of *Typha latifolia* to evaluate its bioenergy potential. *Bioresource Technology* 245, 491–501. <https://doi.org/10.1016/j.biortech.2017.08.162>
- Al-Malack, M.H., Dauda, M., 2017. Competitive adsorption of cadmium and phenol on activated carbon produced from municipal sludge. *Journal of Environmental Chemical Engineering* 5, 2718–2729. <https://doi.org/10.1016/j.jece.2017.05.027>
- Al Arni, S., 2018. Comparison of slow and fast pyrolysis for converting biomass into fuel. *Renewable Energy* 124, 197–201. <https://doi.org/10.1016/j.renene.2017.04.060>
- Alaa El-Din, G., Amer, A.A., Malsh, G., Hussein, M., 2018. Study on the use of banana peels for oil spill removal. *Alexandria Engineering Journal*. <https://doi.org/10.1016/j.aej.2017.05.020>
- Alvarez, J., Amutio, M., Lopez, G., Barbarias, I., Bilbao, J., Olazar, M., 2015a. Sewage sludge valorization by flash pyrolysis in a conical spouted bed reactor. *Chemical Engineering Journal* 273, 173–183. <https://doi.org/10.1016/j.cej.2015.03.047>
- Alvarez, J., Amutio, M., Lopez, G., Bilbao, J., Olazar, M., 2015b. Fast co-pyrolysis of sewage sludge and lignocellulosic biomass in a conical spouted bed reactor. *Fuel* 159, 810–818.

<https://doi.org/10.1016/j.fuel.2015.07.039>

- Alvarez, J., Lopez, G., Amutio, M., Artetxe, M., Barbarias, I., Arregi, A., Bilbao, J., Olazar, M., 2016. Characterization of the bio-oil obtained by fast pyrolysis of sewage sludge in a conical spouted bed reactor. *Fuel Processing Technology* 149, 169–175. <https://doi.org/10.1016/j.fuproc.2016.04.015>
- Angelova, D., Uzunov, I., Uzunova, S., Gigova, A., Minchev, L., 2011. Kinetics of oil and oil products adsorption by carbonized rice husks. *Chemical Engineering Journal* 172, 306–311. <https://doi.org/10.1016/j.cej.2011.05.114>
- Antunes, E., Schumann, J., Brodie, G., Jacob, M. V., Schneider, P.A., 2017. Biochar produced from biosolids using a single-mode microwave: Characterisation and its potential for phosphorus removal. *Journal of Environmental Management* 196, 119–126. <https://doi.org/10.1016/j.jenvman.2017.02.080>
- Arazo, R.O., Genuino, D.A.D., de Luna, M.D.G., Capareda, S.C., 2017. Bio-oil production from dry sewage sludge by fast pyrolysis in an electrically-heated fluidized bed reactor. *Sustainable Environment Research* 27, 7–14. <https://doi.org/10.1016/j.serj.2016.11.010>
- Azizi, K., Keshavarz Moraveji, M., Abedini Najafabadi, H., 2017. Characteristics and kinetics study of simultaneous pyrolysis of microalgae *Chlorella vulgaris*, wood and polypropylene through TGA. *Bioresource Technology* 243, 481–491. <https://doi.org/10.1016/j.biortech.2017.06.155>
- Azuara, M., Fonts, I., Bimbela, F., Murillo, M.B., Gea, G., 2015. Catalytic post-treatment of the vapors from sewage sludge pyrolysis by means of γ -Al₂O₃: Effect on the liquid product properties. *Fuel Processing Technology*. <https://doi.org/10.1016/j.fuproc.2014.10.014>
- Balasundram, V., Ibrahim, N., Kasmani, R.M., Hamid, M.K.A., Isha, R., Hasbullah, H., Ali, R.R., 2018. Thermogravimetric catalytic pyrolysis and kinetic studies of coconut copra and rice husk for possible maximum production of pyrolysis oil. *Journal of Cleaner Production* 167, 218–228. <https://doi.org/10.1016/j.jclepro.2017.08.173>
- Barakat, A.O., Khairy, M.A., Mahmoud, M.R., 2017. Organochlorine pesticides and polychlorinated biphenyls in sewage sludge from Egypt. *Journal of Environmental Science and Health - Part A Toxic/Hazardous Substances and Environmental Engineering* 52, 750–756. <https://doi.org/10.1080/10934529.2017.1303313>
- Beshkar, F., Khojasteh, H., Salavati-Niasari, M., 2017. Recyclable magnetic superhydrophobic straw soot sponge for highly efficient oil/water separation. *Journal of Colloid and Interface Science* 497, 57–65. <https://doi.org/10.1016/j.jcis.2017.02.016>
- Bhardwaj, N., Bhaskarwar, A.N., 2018. A review on sorbent devices for oil-spill control. *Environmental Pollution* 243, 1758–1771. <https://doi.org/10.1016/j.envpol.2018.09.141>
- Björklund, K., Li, L.Y., 2017. Adsorption of organic stormwater pollutants onto activated carbon from sewage sludge. *Journal of Environmental Management* 197, 490–497.

<https://doi.org/10.1016/j.jenvman.2017.04.011>

- Brachi, P., Miccio, F., Miccio, M., Ruoppolo, G., 2015. Isoconversional kinetic analysis of olive pomace decomposition under torrefaction operating conditions. *Fuel Processing Technology* 130, 147–154. <https://doi.org/10.1016/j.fuproc.2014.09.043>
- Bridgwater, A. V., 2012. Review of fast pyrolysis of biomass and product upgrading. *Biomass and Bioenergy* 38, 68–94. <https://doi.org/10.1016/j.biombioe.2011.01.048>
- Bu, Q., Lei, H., Qian, M., Yadavalli, G., 2016. A thermal behavior and kinetics study of the catalytic pyrolysis of lignin. *RSC Advances* 6, 100700–100707. <https://doi.org/10.1039/c6ra22967k>
- Can Montreal turn its sewage into black gold? | Montreal Gazette [WWW Document], n.d. URL <https://montrealgazette.com/news/local-news/a-rosier-future-for-montreals-sewage> (accessed 12.25.19).
- Cao, H., Xin, Y., Wang, D., Yuan, Q., 2014. Pyrolysis characteristics of cattle manures using a discrete distributed activation energy model. *Bioresource Technology* 172, 219–225. <https://doi.org/10.1016/j.biortech.2014.09.049>
- Çepelioğullar, Ö., Mutlu, İ., Yaman, S., Haykiri-Acma, H., 2018. Activation energy prediction of biomass wastes based on different neural network topologies. *Fuel* 220, 535–545. <https://doi.org/10.1016/j.fuel.2018.02.045>
- Chanaka Udayanga, W.D., Veksha, A., Giannis, A., Lisak, G., Chang, V.W.C., Lim, T.T., 2018. Fate and distribution of heavy metals during thermal processing of sewage sludge. *Fuel* 226, 721–744. <https://doi.org/10.1016/j.fuel.2018.04.045>
- Chen, H., Chen, D., Hong, L., 2015. Influences of activation agent impregnated sewage sludge pyrolysis on emission characteristics of volatile combustion and De-NO_x performance of activated char. *Applied Energy* 156, 767–775. <https://doi.org/10.1016/j.apenergy.2015.05.098>
- Chen, P., Xie, Q., Addy, M., Zhou, W., Liu, Y., Wang, Y., Cheng, Y., Li, K., Ruan, R., 2016. Utilization of municipal solid and liquid wastes for bioenergy and bioproducts production. *Bioresource Technology* 215, 163–172. <https://doi.org/10.1016/j.biortech.2016.02.094>
- Chen, Q., Liu, H., Ko, J.H., Wu, H., Xu, Q., 2019. Structure characteristics of bio-char generated from co-pyrolysis of wooden waste and wet municipal sewage sludge. *Fuel Processing Technology* 183, 48–54. <https://doi.org/10.1016/j.fuproc.2018.11.005>
- Cheng, S., Qiao, Y., Huang, J., Wang, W., Wang, Z., Yu, Y., Xu, M., 2018. Effects of Ca and Na acetates on nitrogen transformation during sewage sludge pyrolysis. *Proceedings of the Combustion Institute* 1–8. <https://doi.org/10.1016/j.proci.2018.08.018>
- Cho, D.W., Kwon, G., Yoon, K., Tsang, Y.F., Ok, Y.S., Kwon, E.E., Song, H., 2017. Simultaneous production of syngas and magnetic biochar via pyrolysis of paper mill sludge using CO₂ as

- reaction medium. *Energy Conversion and Management* 145, 1–9. <https://doi.org/10.1016/j.enconman.2017.04.095>
- da Costa Cunha, G., Pinho, N.C., Alves Silva, I.A., Santana Costa, J.A., da Silva, C.M.P., Romão, L.P.C., 2019. Removal of heavy crude oil from water surfaces using a magnetic inorganic-organic hybrid powder and membrane system. *Journal of Environmental Management* 247, 9–18. <https://doi.org/10.1016/j.jenvman.2019.06.050>
- Dai, L., Zeng, Z., Tian, X., Jiang, L., Yu, Z., Wu, Q., Wang, Y., Liu, Y., Ruan, R., 2019. Microwave-assisted catalytic pyrolysis of torrefied corn cob for phenol-rich bio-oil production over Fe modified bio-char catalyst. *Journal of Analytical and Applied Pyrolysis* 143, 104691. <https://doi.org/10.1016/j.jaap.2019.104691>
- Dai, Q., Jiang, X., Jiang, Y., Jin, Y., Wang, F., Chi, Y., Yan, J., Xu, A., 2014. Temperature influence and distribution in three phases of pahs in wet sewage sludge pyrolysis using conventional and microwave heating. *Energy and Fuels* 28, 3317–3325. <https://doi.org/10.1021/ef5003638>
- Dai, Q., Jiang, X., Lv, G., Ma, X., Jin, Y., Wang, F., Chi, Y., Yan, J., 2015. Investigation into particle size influence on PAH formation during dry sewage sludge pyrolysis: TG-FTIR analysis and batch scale research. *Journal of Analytical and Applied Pyrolysis* 112, 388–393. <https://doi.org/10.1016/j.jaap.2014.09.015>
- Dai, Q., Ren, N., Ma, L., Ning, P., Qu, G., Guo, Z., Xie, L., 2018. Research on dewaterability and properties of sewage sludge under modified phosphogypsum and acetic acid pretreatments. *Bioresource Technology* 264, 268–276. <https://doi.org/10.1016/j.biortech.2018.05.078>
- Daorattanachai, P., Laosiripojana, W., Laobuthee, A., Laosiripojana, N., 2018. Type of contribution: Research article catalytic activity of sewage sludge char supported Re-Ni bimetallic catalyst toward cracking/reforming of biomass tar. *Renewable Energy* 121, 644–651. <https://doi.org/10.1016/j.renene.2018.01.096>
- Demirel Bayık, G., Altın, A., 2017. Production of sorbent from paper industry solid waste for oil spill cleanup. *Marine Pollution Bulletin* 125, 341–349. <https://doi.org/10.1016/j.marpolbul.2017.09.040>
- Di Iorio, E., Colombo, C., Cheng, Z., Capitani, G., Mele, D., Ventruti, G., Angelico, R., 2019. Characterization of magnetite nanoparticles synthesized from Fe(II)/nitrate solutions for arsenic removal from water. *Journal of Environmental Chemical Engineering* 7, 102986. <https://doi.org/10.1016/j.jece.2019.102986>
- Dong, T., Gao, D., Miao, C., Yu, X., Degan, C., Garcia-Pérez, M., Rasco, B., Sablani, S.S., Chen, S., 2015. Two-step microalgal biodiesel production using acidic catalyst generated from pyrolysis-derived bio-char. *Energy Conversion and Management* 105, 1389–1396. <https://doi.org/10.1016/j.enconman.2015.06.072>
- dos Reis, G.S., Adebayo, M.A., Lima, E.C., Sampaio, C.H., Prola, L.D.T., 2016. Activated Carbon from Sewage Sludge for Preconcentration of Copper. *Analytical Letters* 49, 541–555.

<https://doi.org/10.1080/00032719.2015.1076833>

- El-Sayed, S.A., Mostafa, M.E., 2015. Kinetic Parameters Determination of Biomass Pyrolysis Fuels Using TGA and DTA Techniques. *Waste and Biomass Valorization* 6, 401–415. <https://doi.org/10.1007/s12649-015-9354-7>
- Fan, S., Wang, Y., Wang, Z., Tang, Jie, Tang, Jun, Li, X., 2017. Removal of methylene blue from aqueous solution by sewage sludge-derived biochar: Adsorption kinetics, equilibrium, thermodynamics and mechanism. *Journal of Environmental Chemical Engineering* 5, 601–611. <https://doi.org/10.1016/j.jece.2016.12.019>
- Fang, W., Zhang, X., Zhang, P., Wan, J., Guo, H., Ghasimi, D.S.M., Morera, X.C., Zhang, T., 2020. Overview of key operation factors and strategies for improving fermentative volatile fatty acid production and product regulation from sewage sludge. *Journal of Environmental Sciences (China)* 87, 93–111. <https://doi.org/10.1016/j.jes.2019.05.027>
- Fernandez-Anez, N., Slatter, D.J.F., Saeed, M.A., Phylaktou, H.N., Andrews, G.E., Garcia-Torrent, J., 2018. Ignition sensitivity of solid fuel mixtures. *Fuel* 223, 451–461. <https://doi.org/10.1016/j.fuel.2018.02.106>
- Fijalkowski, K.L., Kacprzak, M.J., Rorat, A., 2014. Occurrence changes of *Escherichia coli* (including O157:H7 serotype) in wastewater and sewage sludge by quantitation method of (EMA) real time-PCR. *Desalination and Water Treatment* 52, 3965–3972. <https://doi.org/10.1080/19443994.2014.887499>
- Folgueras, M.B., Alonso, M., Díaz, R.M., 2013. Influence of sewage sludge treatment on pyrolysis and combustion of dry sludge. *Energy* 55, 426–435. <https://doi.org/10.1016/j.energy.2013.03.063>
- Fonts, I., Gea, G., Azuara, M., Ábrego, J., Arauzo, J., 2012. Sewage sludge pyrolysis for liquid production: A review. *Renewable and Sustainable Energy Reviews* 16, 2781–2805. <https://doi.org/10.1016/j.rser.2012.02.070>
- Fu, D. qing, Li, X. hong, Li, W. ying, Feng, J., 2018. Catalytic upgrading of coal pyrolysis products over bio-char. *Fuel Processing Technology* 176, 240–248. <https://doi.org/10.1016/j.fuproc.2018.04.001>
- Gamliel, D.P., Bollas, G.M., Valla, J.A., 2018. Two-stage catalytic fast hydrolysis of biomass for the production of drop-in biofuel. *Fuel* 216, 160–170. <https://doi.org/10.1016/j.fuel.2017.12.017>
- Gao, N., Kamran, K., Quan, C., Williams, P.T., 2020. Thermochemical conversion of sewage sludge: A critical review. *Progress in Energy and Combustion Science*. <https://doi.org/10.1016/j.pecs.2020.100843>
- Gao, N., Quan, C., Liu, B., Li, Z., Wu, C., Li, A., 2017. Continuous Pyrolysis of Sewage Sludge in a Screw-Feeding Reactor: Products Characterization and Ecological Risk Assessment of Heavy Metals. *Energy and Fuels* 31, 5063–5072.

<https://doi.org/10.1021/acs.energyfuels.6b03112>

- Garba, M.U., Inalegwu, A., Musa, U., Aboje, A.A., Kovo, A.S., Adeniyi, D.O., 2018. Thermogravimetric characteristic and kinetic of catalytic co-pyrolysis of biomass with low- and high-density polyethylenes. *Biomass Conversion and Biorefinery* 8, 143–150. <https://doi.org/10.1007/s13399-017-0261-y>
- Gu, L., Li, B., Wen, H., Zhang, X., Wang, L., Ye, J., 2018. Co-hydrothermal treatment of fallen leaves with iron sludge to prepare magnetic iron product and solid fuel. *Bioresource Technology* 257, 229–237. <https://doi.org/10.1016/j.biortech.2018.02.113>
- Gunasee, S.D., Danon, B., Görgens, J.F., Mohee, R., 2017. Co-pyrolysis of LDPE and cellulose: Synergies during devolatilization and condensation. *Journal of Analytical and Applied Pyrolysis* 126, 307–314. <https://doi.org/10.1016/j.jaap.2017.05.016>
- Guo, F., Li, X., Liu, Y., Peng, K., Guo, C., Rao, Z., 2018. Catalytic cracking of biomass pyrolysis tar over char-supported catalysts. *Energy Conversion and Management* 167, 81–90. <https://doi.org/10.1016/j.enconman.2018.04.094>
- Guo, F., Peng, K., Liang, S., Jia, X., Jiang, X., Qian, L., 2019. Evaluation of the catalytic performance of different activated biochar catalysts for removal of tar from biomass pyrolysis. *Fuel* 258, 116204. <https://doi.org/10.1016/j.fuel.2019.116204>
- Hadi, P., Xu, M., Ning, C., Sze Ki Lin, C., McKay, G., 2015. A critical review on preparation, characterization and utilization of sludge-derived activated carbons for wastewater treatment. *Chemical Engineering Journal* 260, 895–906. <https://doi.org/10.1016/j.cej.2014.08.088>
- Hameed, Z., Aman, Z., Naqvi, S.R., Tariq, R., Ali, I., Makki, A.A., 2018. Kinetic and Thermodynamic Analyses of Sugar Cane Bagasse and Sewage Sludge Co-pyrolysis Process. *Energy and Fuels* 32, 9551–9558. <https://doi.org/10.1021/acs.energyfuels.8b01972>
- Hassan, H., Lim, J.K., Hameed, B.H., 2016. Recent progress on biomass co-pyrolysis conversion into high-quality bio-oil. *Bioresource Technology* 221, 645–655. <https://doi.org/10.1016/j.biortech.2016.09.026>
- He, C., Tang, C., Liu, W., Dai, L., Qiu, R., 2020. Co-pyrolysis of sewage sludge and hydrochar with coals: Pyrolytic behaviors and kinetics analysis using TG-FTIR and a discrete distributed activation energy model. *Energy Conversion and Management* 203, 112226. <https://doi.org/10.1016/j.enconman.2019.112226>
- He, Q., Ding, L., Gong, Y., Li, W., Wei, J., Yu, G., 2019. Effect of torrefaction on pinewood pyrolysis kinetics and thermal behavior using thermogravimetric analysis. *Bioresource Technology* 280, 104–111. <https://doi.org/10.1016/j.biortech.2019.01.138>
- Hernández, A.B., Okonta, F., Freeman, N., 2017. Thermal decomposition of sewage sludge under N₂, CO₂ and air: Gas characterization and kinetic analysis. *Journal of Environmental Management* 196, 560–568. <https://doi.org/10.1016/j.jenvman.2017.03.036>

- Hossain, M.K., Strezov Vladimir, V., Chan, K.Y., Ziolkowski, A., Nelson, P.F., 2011. Influence of pyrolysis temperature on production and nutrient properties of wastewater sludge biochar. *Journal of Environmental Management* 92, 223–228. <https://doi.org/10.1016/j.jenvman.2010.09.008>
- Hu, G., Li, J., Zhang, X., Li, Y., 2017. Investigation of waste biomass co-pyrolysis with petroleum sludge using a response surface methodology. *Journal of Environmental Management* 192, 234–242. <https://doi.org/10.1016/j.jenvman.2017.01.069>
- Hu, J., Danish, M., Lou, Z., Zhou, P., Zhu, N., Yuan, H., Qian, P., 2018. Effectiveness of wind turbine blades waste combined with the sewage sludge for enriched carbon preparation through the co-pyrolysis processes. *Journal of Cleaner Production* 174, 780–787. <https://doi.org/10.1016/j.jclepro.2017.10.166>
- Huang, F., Yu, Y., Huang, H., 2018. Temperature influence and distribution of bio-oil from pyrolysis of granular sewage sludge. *Journal of Analytical and Applied Pyrolysis* 130, 249–255. <https://doi.org/10.1016/j.jaap.2018.01.030>
- Huang, L., Xie, C., Liu, J., Zhang, X., Chang, K.L., Kuo, J., Sun, J., Xie, W., Zheng, L., Sun, S., Buyukada, M., Evrendilek, F., 2018. Influence of catalysts on co-combustion of sewage sludge and water hyacinth blends as determined by TG-MS analysis. *Bioresource Technology* 247, 217–225. <https://doi.org/10.1016/j.biortech.2017.09.039>
- Huang, X., Cao, J.P., Shi, P., Zhao, X.Y., Feng, X.B., Zhao, Y.P., Fan, X., Wei, X.Y., Takarada, T., 2014. Influences of pyrolysis conditions in the production and chemical composition of the bio-oils from fast pyrolysis of sewage sludge. *Journal of Analytical and Applied Pyrolysis* 110, 353–362. <https://doi.org/10.1016/j.jaap.2014.10.003>
- Huang, Y., Sun, Y., Xu, Z., Luo, M., Zhu, C., Li, L., 2017. Removal of aqueous oxalic acid by heterogeneous catalytic ozonation with MnOx/sewage sludge-derived activated carbon as catalysts. *Science of the Total Environment* 575, 50–57. <https://doi.org/10.1016/j.scitotenv.2016.10.026>
- Huang, Y.F., Shih, C.H., Chiueh, P. Te, Lo, S.L., 2015. Microwave co-pyrolysis of sewage sludge and rice straw. *Energy* 87, 638–644. <https://doi.org/10.1016/j.energy.2015.05.039>
- Ieamviteevanich, P., Palaporn, D., Chanlek, N., Poo-Arporn, Y., Mongkolthanaruk, W., Eichhorn, S.J., Pinitsoontorn, S., 2020. Carbon Nanofiber Aerogel/Magnetic Core-Shell Nanoparticle Composites as Recyclable Oil Sorbents. *ACS Applied Nano Materials* 3, 3939–3950. <https://doi.org/10.1021/acsanm.0c00818>
- Ifelebuegu, A.O., Johnson, A., 2017. Nonconventional low-cost cellulose- and keratin-based biopolymeric sorbents for oil/water separation and spill cleanup: A review. *Critical Reviews in Environmental Science and Technology*. <https://doi.org/10.1080/10643389.2017.1318620>
- Ignatowicz, K., 2017. The impact of sewage sludge treatment on the content of selected heavy metals and their fractions. *Environmental Research* 156, 19–22. <https://doi.org/10.1016/j.envres.2017.02.035>

- Ji, A., Zhang, S., Lu, X., Liu, Y., 2010. A new method for evaluating the sewage sludge pyrolysis kinetics. *Waste Management* 30, 1225–1229. <https://doi.org/10.1016/j.wasman.2009.10.003>
- Jin, W., Shen, D., Liu, Q., Xiao, R., 2016. Evaluation of the co-pyrolysis of lignin with plastic polymers by TG-FTIR and Py-GC/MS. *Polymer Degradation and Stability* 133, 65–74. <https://doi.org/10.1016/j.polyimdeggradstab.2016.08.001>
- Kan, T., Strezov, V., Evans, T., 2016. Effect of the Heating Rate on the Thermochemical Behavior and Biofuel Properties of Sewage Sludge Pyrolysis. *Energy and Fuels* 30, 1564–1570. <https://doi.org/10.1021/acs.energyfuels.5b02232>
- Kandanelli, R., Meesala, L., Kumar, J., Raju, C.S.K., Peddy, V.C.R., Gandham, S., Kumar, P., 2018. Being buoyant, the sorbent floats on the water surface. *Marine Pollution Bulletin* 128, 32–40. <https://doi.org/10.1016/j.marpolbul.2018.01.010>
- Karzar Jeddi, M., Laitinen, O., Liimatainen, H., 2019. Magnetic superabsorbents based on nanocellulose aerobeads for selective removal of oils and organic solvents. *Materials and Design* 183, 108115. <https://doi.org/10.1016/j.matdes.2019.108115>
- Kim, Y., Parker, W., 2008. A technical and economic evaluation of the pyrolysis of sewage sludge for the production of bio-oil. *Bioresource Technology* 99, 1409–1416. <https://doi.org/10.1016/j.biortech.2007.01.056>
- Kim, Yong Sang, Kim, Young Seok, Kim, S.H., 2010. Investigation of Thermodynamic Parameters in the Thermal Decomposition of Plastic Waste–Waste Lube Oil Compounds. *Environmental Science & Technology* 44, 5313–5317. <https://doi.org/10.1021/es101163e>
- Komlev, A., Lähderanta, E., Shevchenko, E., Vorob'ev-Desyatovskii, N., 2018. Magnetism of purified amorphous carbon. *EPJ Web of Conferences* 185, 8–11. <https://doi.org/10.1051/epjconf/201818504012>
- Lee, J., Kim, K.H., Kwon, E.E., 2017. Biochar as a Catalyst. *Renewable and Sustainable Energy Reviews* 77, 70–79. <https://doi.org/10.1016/j.rser.2017.04.002>
- Li, X., Zhang, H., Li, J., Su, L., Zuo, J., Komarneni, S., Wang, Y., 2013. Improving the aromatic production in catalytic fast pyrolysis of cellulose by co-feeding low-density polyethylene. *Applied Catalysis A: General* 455, 114–121. <https://doi.org/10.1016/j.apcata.2013.01.038>
- Li, Y.Q., Samad, Y.A., Polychronopoulou, K., Alhassan, S.M., Liao, K., 2014. Carbon aerogel from winter melon for highly efficient and recyclable oils and organic solvents absorption. *ACS Sustainable Chemistry and Engineering* 2, 1492–1497. <https://doi.org/10.1021/sc500161b>
- Liang, J., Morgan, H.M., Liu, Y., Shi, A., Lei, H., Mao, H., Bu, Q., 2017. Enhancement of bio-oil yield and selectivity and kinetic study of catalytic pyrolysis of rice straw over transition metal modified ZSM-5 catalyst. *Journal of Analytical and Applied Pyrolysis* 128, 324–334. <https://doi.org/10.1016/j.jaap.2017.09.018>

- Lin, Q.H., Cheng, H., Chen, G.Y., 2012. Preparation and characterization of carbonaceous adsorbents from sewage sludge using a pilot-scale microwave heating equipment. *Journal of Analytical and Applied Pyrolysis* 93, 113–119. <https://doi.org/10.1016/j.jaap.2011.10.006>
- Lin, Y., Tian, Y., Xia, Y., Fang, S., Liao, Y., Yu, Z., Ma, X., 2019. General distributed activation energy model (G-DAEM) on co-pyrolysis kinetics of bagasse and sewage sludge. *Bioresource Technology* 273, 545–555. <https://doi.org/10.1016/j.biortech.2018.11.051>
- Lin, Yan, Liao, Y., Yu, Z., Fang, S., Lin, Yousheng, Fan, Y., Peng, X., Ma, X., 2016. Co-pyrolysis kinetics of sewage sludge and oil shale thermal decomposition using TGA-FTIR analysis. *Energy Conversion and Management* 118, 345–352. <https://doi.org/10.1016/j.enconman.2016.04.004>
- Liu, G., Song, H., Wu, J., 2015. Thermogravimetric study and kinetic analysis of dried industrial sludge pyrolysis. *Waste Management* 41, 128–133. <https://doi.org/10.1016/j.wasman.2015.03.042>
- Liu, G., Wright, M.M., Zhao, Q., Brown, R.C., 2016. Hydrocarbon and Ammonia Production from Catalytic Pyrolysis of Sewage Sludge with Acid Pretreatment. *ACS Sustainable Chemistry and Engineering* 4, 1819–1826. <https://doi.org/10.1021/acssuschemeng.6b00016>
- Liu, Q., Xiong, Z., Syed-Hassan, S.S.A., Deng, Z., Zhao, X., Su, S., Xiang, J., Wang, Y., Hu, S., 2019. Effect of the pre-reforming by Fe/bio-char catalyst on a two-stage catalytic steam reforming of bio-oil. *Fuel* 239, 282–289. <https://doi.org/10.1016/j.fuel.2018.11.029>
- Liu, S., Zhang, Y., Fan, L., Zhou, N., Tian, G., Zhu, X., Cheng, Y., Wang, Y., Liu, Y., Chen, P., Ruan, R., 2017. Bio-oil production from sequential two-step catalytic fast microwave-assisted biomass pyrolysis. *Fuel* 196, 261–268. <https://doi.org/10.1016/j.fuel.2017.01.116>
- Liu, T.L., Cao, J.P., Zhao, X.Y., Wang, J.X., Ren, X.Y., Fan, X., Zhao, Y.P., Wei, X.Y., 2017. In situ upgrading of Shengli lignite pyrolysis vapors over metal-loaded HZSM-5 catalyst. *Fuel Processing Technology* 160, 19–26. <https://doi.org/10.1016/j.fuproc.2017.02.012>
- Liu, W., Hu, C., Yang, Y., Tong, D., Li, G., Zhu, L., 2010. Influence of ZSM-5 zeolite on the pyrolytic intermediates from the co-pyrolysis of pubescens and LDPE. *Energy Conversion and Management* 51, 1025–1032. <https://doi.org/10.1016/j.enconman.2009.12.005>
- Liu, X., Chang, F., Wang, C., Jin, Z., Wu, J., Zuo, J., Wang, K., 2018. Pyrolysis and subsequent direct combustion of pyrolytic gases for sewage sludge treatment in China. *Applied Thermal Engineering* 128, 464–470. <https://doi.org/10.1016/j.applthermaleng.2017.08.091>
- Lu, P., Huang, Q., (Thanos) Bourtsalas, A.C., Chi, Y., Yan, J., 2018. Synergistic effects on char and oil produced by the co-pyrolysis of pine wood, polyethylene and polyvinyl chloride. *Fuel* 230, 359–367. <https://doi.org/10.1016/j.fuel.2018.05.072>
- Luo, Z., Wang, S., Guo, X., 2012. Selective pyrolysis of Organosolv lignin over zeolites with product analysis by TG-FTIR. *Journal of Analytical and Applied Pyrolysis* 95, 112–117. <https://doi.org/10.1016/j.jaap.2012.01.014>

- M. Inguanzo, A. Dominguez, J.A. Mene'ndez, C.G. Blanco, J.J.P., 2002. On the pyrolysis of sewage sludge: The influence of pyrolysis temperature on biochar, liquid and gas fractions. *Journal of Analytical and Applied Pyrolysis* 518–523, 209–222. [https://doi.org/https://doi.org/10.1016/S0165-2370\(01\)00155-3](https://doi.org/https://doi.org/10.1016/S0165-2370(01)00155-3)
- Mahmood, A.S.N., Brammer, J.G., Hornung, A., Steele, A., Poulston, S., 2013. The intermediate pyrolysis and catalytic steam reforming of Brewers spent grain. *Journal of Analytical and Applied Pyrolysis* 103, 328–342. <https://doi.org/10.1016/j.jaap.2012.09.009>
- Mastral, J.F., Javier, A., Gea, G., 2015. Sewage Sludge Torrefaction in an Auger Reactor. <https://doi.org/10.1021/ef501425h>
- Mehmood, M.A., Ye, G., Luo, H., Liu, C., Malik, S., Afzal, I., Xu, J., Ahmad, M.S., 2017. Pyrolysis and kinetic analyses of Camel grass (*Cymbopogon schoenanthus*) for bioenergy. *Bioresource Technology* 228, 18–24. <https://doi.org/10.1016/j.biortech.2016.12.096>
- Mishra, R.K., Mohanty, K., 2018. Pyrolysis kinetics and thermal behavior of waste sawdust biomass using thermogravimetric analysis. *Bioresource Technology* 251, 63–74. <https://doi.org/10.1016/j.biortech.2017.12.029>
- Morgan, H.M., Bu, Q., Liang, J., Liu, Y., Mao, H., Shi, A., Lei, H., Ruan, R., 2017. A review of catalytic microwave pyrolysis of lignocellulosic biomass for value-added fuel and chemicals. *Bioresource Technology* 230, 112–121. <https://doi.org/10.1016/j.biortech.2017.01.059>
- Motta, F.L., Stoyanov, S.R., Soares, J.B.P., 2019. Development and application of an amylopectin-graft-poly(methyl acrylate) solidifier for rapid and efficient containment and recovery of heavy oil spills in aqueous environments. *Chemosphere* 236. <https://doi.org/10.1016/j.chemosphere.2019.124352>
- Mullen, C.A., Dorado, C., Boateng, A.A., 2018. Catalytic co-pyrolysis of switchgrass and polyethylene over HZSM-5: Catalyst deactivation and coke formation. *Journal of Analytical and Applied Pyrolysis* 129, 195–203. <https://doi.org/10.1016/j.jaap.2017.11.012>
- Naqvi, S.R., Tariq, R., Hameed, Z., Ali, I., Naqvi, M., Chen, W.H., Ceylan, S., Rashid, H., Ahmad, J., Taqvi, S.A., Shahbaz, M., 2019. Pyrolysis of high ash sewage sludge: Kinetics and thermodynamic analysis using Coats-Redfern method. *Renewable Energy* 131, 854–860. <https://doi.org/10.1016/j.renene.2018.07.094>
- Naqvi, S.R., Tariq, R., Hameed, Z., Ali, I., Taqvi, S.A., Naqvi, M., Niazi, M.B.K., Noor, T., Farooq, W., 2018. Pyrolysis of high-ash sewage sludge: Thermo-kinetic study using TGA and artificial neural networks. *Fuel* 233, 529–538. <https://doi.org/10.1016/j.fuel.2018.06.089>
- Navarathna, C.M., Bombuwala Dewage, N., Keeton, C., Pennisson, J., Henderson, R., Lashley, B., Zhang, X., Hassan, E.B., Perez, F., Mohan, D., Pittman, C.U., Mlsna, T., 2020. Biochar Adsorbents with Enhanced Hydrophobicity for Oil Spill Removal. *ACS Applied Materials and Interfaces* 12, 9248–9260. <https://doi.org/10.1021/acsami.9b20924>
- Ngaini, Z., Noh, F., Wahi, R., 2018. Facile sorbent from esterified cellulosic sago waste for engine

- oil removal in marine environment. *International Journal of Environmental Science and Technology* 15, 341–348. <https://doi.org/10.1007/s13762-017-1389-9>
- Nguyen, H.N., Pignatello, J.J., 2013. Laboratory tests of biochars as absorbents for use in recovery or containment of marine crude oil spills. *Environmental Engineering Science* 30, 374–380.
- Nhuchhen, D.R., Abdul Salam, P., 2012. Estimation of higher heating value of biomass from proximate analysis: A new approach. *Fuel* 99, 55–63. <https://doi.org/10.1016/j.fuel.2012.04.015>
- Nurliyana Che Mohamed Hussein, S., Hidayati Othman, N., Dollah, A., Nazihah Che Abdul Rahim, A., Shuhadah Japperi, N., Syamimi Mohd Asymawi Ramakrishnan, N., 2019. Study of Acid Treated Mixed Sawdust as Natural Oil Sorbent for Oil Spill. *Materials Today: Proceedings* 19, 1382–1389. <https://doi.org/10.1016/j.matpr.2019.11.156>
- Oleszczuk, P., Hale, S.E., Lehmann, J., Cornelissen, G., 2012. Activated carbon and biochar amendments decrease pore-water concentrations of polycyclic aromatic hydrocarbons (PAHs) in sewage sludge. *Bioresource Technology* 111, 84–91. <https://doi.org/10.1016/j.biortech.2012.02.030>
- Oyedun, A.O., Tee, C.Z., Hanson, S., Hui, C.W., 2014. Thermogravimetric analysis of the pyrolysis characteristics and kinetics of plastics and biomass blends. *Fuel Processing Technology* 128, 471–481. <https://doi.org/10.1016/j.fuproc.2014.08.010>
- Özsin, G., Pütün, A.E., 2019. TGA/MS/FT-IR study for kinetic evaluation and evolved gas analysis of a biomass/PVC co-pyrolysis process. *Energy Conversion and Management* 182, 143–153. <https://doi.org/10.1016/j.enconman.2018.12.060>
- Özsin, G., Pütün, A.E., 2017. Kinetics and evolved gas analysis for pyrolysis of food processing wastes using TGA/MS/FT-IR. *Waste Management* 64, 315–326. <https://doi.org/10.1016/j.wasman.2017.03.020>
- Özsin, G., Pütün, A.E., Pütün, E., 2019. Investigating the interactions between lignocellulosic biomass and synthetic polymers during co-pyrolysis by simultaneous thermal and spectroscopic methods. *Biomass Conversion and Biorefinery*. <https://doi.org/10.1007/s13399-019-00390-9>
- Park, H.J., Heo, H.S., Park, Y.K., Yim, J.H., Jeon, J.K., Park, J., Ryu, C., Kim, S.S., 2010. Clean bio-oil production from fast pyrolysis of sewage sludge: Effects of reaction conditions and metal oxide catalysts. *Bioresource Technology* 101, S83–S85. <https://doi.org/10.1016/j.biortech.2009.06.103>
- Patil, V., Adhikari, S., Cross, P., 2018. Co-pyrolysis of lignin and plastics using red clay as catalyst in a micro-pyrolyzer. *Bioresource Technology* 270, 311–319. <https://doi.org/10.1016/j.biortech.2018.09.034>
- Persson, H., Duman, I., Wang, S., Pettersson, L.J., Yang, W., 2019. Catalytic pyrolysis over transition metal-modified zeolites: A comparative study between catalyst activity and

- deactivation. *Journal of Analytical and Applied Pyrolysis* 138, 54–61. <https://doi.org/10.1016/j.jaap.2018.12.005>
- Phanthong, P., Reubroycharoen, P., Kongparakul, S., Samart, C., Wang, Z., Hao, X., Abudula, A., Guan, G., 2018. Fabrication and evaluation of nanocellulose sponge for oil/water separation. *Carbohydrate Polymers* 190, 184–189. <https://doi.org/https://doi.org/10.1016/j.carbpol.2018.02.066>
- Praspaliauskas, M., Pedišius, N., 2017. A review of sludge characteristics in Lithuania's wastewater treatment plants and perspectives of its usage in thermal processes. *Renewable and Sustainable Energy Reviews* 67, 899–907. <https://doi.org/10.1016/j.rser.2016.09.041>
- Praspaliauskas, M., Pedišius, N., Striuigas, N., 2018. Elemental Migration and Transformation from Sewage Sludge to Residual Products during the Pyrolysis Process. *Energy and Fuels* 32, 5199–5208. <https://doi.org/10.1021/acs.energyfuels.8b00196>
- Raj, K.G., Joy, P.A., 2015. Coconut shell based activated carbon-iron oxide magnetic nanocomposite for fast and efficient removal of oil spills. *Journal of Environmental Chemical Engineering* 3, 2068–2075. <https://doi.org/10.1016/j.jece.2015.04.028>
- Rajapaksha, A.U., Chen, S.S., Tsang, D.C.W., Zhang, M., Vithanage, M., Mandal, S., Gao, B., Bolan, N.S., Ok, Y.S., 2016. Engineered/designer biochar for contaminant removal/immobilization from soil and water: Potential and implication of biochar modification. *Chemosphere* 148, 276–291. <https://doi.org/10.1016/j.chemosphere.2016.01.043>
- Raza, S., Hameed, Z., Tariq, R., Taqvi, S.A., Ali, I., Khan, M.B., Noor, T., Hussain, A., Iqbal, N., Shahbaz, M., 2019. Synergistic effect on co-pyrolysis of rice husk and sewage sludge by thermal behavior, kinetics, thermodynamic parameters and artificial neural network. *Waste Management* 85, 131–140. <https://doi.org/10.1016/j.wasman.2018.12.031>
- Ren, S., Lei, H., Wang, L., Bu, Q., Chen, S., Wu, J., 2014. Hydrocarbon and hydrogen-rich syngas production by biomass catalytic pyrolysis and bio-oil upgrading over biochar catalysts. *RSC Advances* 4, 10731–10737. <https://doi.org/10.1039/c4ra00122b>
- Resende, F.L.P., 2016. Recent advances on fast hydrolysis of biomass. *Catalysis Today* 269, 148–155. <https://doi.org/10.1016/j.cattod.2016.01.004>
- Romanovskii, V.I., Martsul, V.N., 2009. Distribution of heteroatoms of synthetic ion exchangers in pyrolysis products. *Russian Journal of Applied Chemistry* 82, 836–839. <https://doi.org/10.1134/S1070427209050164>
- Ruiz-Gómez, N., Quispe, V., Ábrego, J., Atienza-Martínez, M., Murillo, M.B., Gea, G., 2017. Co-pyrolysis of sewage sludge and manure. *Waste Management* 59, 211–221. <https://doi.org/10.1016/j.wasman.2016.11.013>
- Saleem, J., Adil Riaz, M., Gordon, M., 2018. Oil sorbents from plastic wastes and polymers: A review. *Journal of Hazardous Materials*. <https://doi.org/10.1016/j.jhazmat.2017.07.072>

- Saleh, T.A., Naeemullah, Tuzen, M., Sari, A., 2017. Polyethylenimine modified activated carbon as novel magnetic adsorbent for the removal of uranium from aqueous solution. *Chemical Engineering Research and Design* 117, 218–227. <https://doi.org/10.1016/j.cherd.2016.10.030>
- Salema, A.A., Ting, R.M.W., Shang, Y.K., 2019. Pyrolysis of blend (oil palm biomass and sawdust) biomass using TG-MS. *Bioresource Technology* 274, 439–446. <https://doi.org/10.1016/j.biortech.2018.12.014>
- Samanya, J., Hornung, A., Apfelbacher, A., Vale, P., 2012. Characteristics of the upper phase of bio-oil obtained from co-pyrolysis of sewage sludge with wood, rapeseed and straw. *Journal of Analytical and Applied Pyrolysis* 94, 120–125. <https://doi.org/10.1016/j.jaap.2011.11.017>
- Samolada, M.C., Zabaniotou, A.A., 2014. Comparative assessment of municipal sewage sludge incineration, gasification and pyrolysis for a sustainable sludge-to-energy management in Greece. *Waste Management* 34, 411–420. <https://doi.org/10.1016/j.wasman.2013.11.003>
- Sánchez, M.E., Menéndez, J.A., Domínguez, A., Pis, J.J., Martínez, O., Calvo, L.F., Bernad, P.L., 2009. Effect of pyrolysis temperature on the composition of the oils obtained from sewage sludge. *Biomass and Bioenergy* 33, 933–940. <https://doi.org/10.1016/j.biombioe.2009.02.002>
- Sfakiotakis, S., Vamvuka, D., 2018. Study of co-pyrolysis of olive kernel with waste biomass using TGA/DTG/MS. *Thermochimica Acta* 670, 44–54. <https://doi.org/10.1016/j.tca.2018.10.006>
- Shahbeig, H., Nosrati, M., 2020. Pyrolysis of municipal sewage sludge for bioenergy production: Thermo-kinetic studies, evolved gas analysis, and techno-socio-economic assessment. *Renewable and Sustainable Energy Reviews* 119, 109567. <https://doi.org/10.1016/j.rser.2019.109567>
- Shahrokhi-Shahraki, R., Benally, C., El-Din, M.G., Park, J., 2021. High efficiency removal of heavy metals using tire-derived activated carbon vs commercial activated carbon: Insights into the adsorption mechanisms. *Chemosphere* 264, 128455. <https://doi.org/10.1016/j.chemosphere.2020.128455>
- Shao, J., Yan, R., Chen, H., Wang, B., Lee, D.H., Liang, D.T., 2008. Pyrolysis characteristics and kinetics of sewage sludge by thermogravimetry Fourier transform infrared analysis. *Energy and Fuels* 22, 38–45. <https://doi.org/10.1021/ef700287p>
- Shao, J., Yan, R., Chen, H., Yang, H., Lee, D.H., 2010. Catalytic effect of metal oxides on pyrolysis of sewage sludge. *Fuel Processing Technology* 91, 1113–1118. <https://doi.org/10.1016/j.fuproc.2010.03.023>
- Shen, L., Zhang, D.K., 2005. Low-temperature pyrolysis of sewage sludge and putrescible garbage for fuel oil production. *Fuel* 84, 809–815. <https://doi.org/10.1016/j.fuel.2004.11.024>
- Shen, Y., Zhao, P., Shao, Q., Ma, D., Takahashi, F., Yoshikawa, K., 2014. In-situ catalytic conversion of tar using rice husk char-supported nickel-iron catalysts for biomass

- pyrolysis/gasification. *Applied Catalysis B: Environmental* 152–153, 140–151. <https://doi.org/10.1016/j.apcatb.2014.01.032>
- Shiba, N.C., Ntuli, F., 2017. Extraction and precipitation of phosphorus from sewage sludge. *Waste Management* 60, 191–200. <https://doi.org/10.1016/j.wasman.2016.07.031>
- Shokry, H., Elkady, M., Salama, E., 2020. Eco-friendly magnetic activated carbon nano-hybrid for facile oil spills separation. *Scientific Reports* 10, 1–17. <https://doi.org/10.1038/s41598-020-67231-y>
- Sidik, S.M., Jalil, A.A., Triwahyono, S., Adam, S.H., Satar, M.A.H., Hameed, B.H., 2012. Modified oil palm leaves adsorbent with enhanced hydrophobicity for crude oil removal. *Chemical Engineering Journal* 203, 9–18. <https://doi.org/10.1016/j.cej.2012.06.132>
- Silvani, L., Vrchotova, B., Kastanek, P., Demnerova, K., Pettiti, I., Papini, M.P., 2017. Characterizing Biochar as Alternative Sorbent for Oil Spill Remediation. *Scientific Reports* 7, 1–10. <https://doi.org/10.1038/srep43912>
- Sizmur, T., Fresno, T., Akgül, G., Frost, H., Moreno-Jiménez, E., 2017. Biochar modification to enhance sorption of inorganics from water. *Bioresource Technology* 246, 34–47. <https://doi.org/10.1016/j.biortech.2017.07.082>
- Sunphorka, S., Chalermssinsuwan, B., Piumsomboon, P., 2017. Artificial neural network model for the prediction of kinetic parameters of biomass pyrolysis from its constituents. *Fuel* 193, 142–158. <https://doi.org/10.1016/j.fuel.2016.12.046>
- Suriapparao, D. V., Batchu, S.P., Jayasurya, S., Vinu, R., 2018a. Selective production of phenolics from waste printed circuit boards via microwave assisted pyrolysis. *Journal of Cleaner Production* 197, 525–533. <https://doi.org/10.1016/j.jclepro.2018.06.203>
- Suriapparao, D. V., Boruah, B., Raja, D., Vinu, R., 2018b. Microwave assisted co-pyrolysis of biomasses with polypropylene and polystyrene for high quality bio-oil production. *Fuel Processing Technology* 175, 64–75. <https://doi.org/10.1016/j.fuproc.2018.02.019>
- Syed-Hassan, S.S.A., Wang, Y., Hu, S., Su, S., Xiang, J., 2017. Thermochemical processing of sewage sludge to energy and fuel: Fundamentals, challenges and considerations. *Renewable and Sustainable Energy Reviews* 80, 888–913. <https://doi.org/10.1016/j.rser.2017.05.262>
- Tan, X. fei, Liu, S. bo, Liu, Y. guo, Gu, Y. ling, Zeng, G. ming, Hu, X. jiang, Wang, X., Liu, S. heng, Jiang, L. hua, 2017. Biochar as potential sustainable precursors for activated carbon production: Multiple applications in environmental protection and energy storage. *Bioresource Technology* 227, 359–372. <https://doi.org/10.1016/j.biortech.2016.12.083>
- Tayeb, A.M., Farouq, R., Mohamed, O.A., Tony, M.A., 2020. Oil spill clean-up using combined sorbents: a comparative investigation and design aspects. *International Journal of Environmental Analytical Chemistry* 100, 311–323. <https://doi.org/10.1080/03067319.2019.1636976>

- Thakkar, S.V., Pinna, A., Carbonaro, C.M., Malfatti, L., Guardia, P., Cabot, A., Casula, M.F., 2020. Performance of oil sorbents based on reduced graphene oxide-silica composite aerogels. *Journal of Environmental Chemical Engineering* 8, 103632. <https://doi.org/10.1016/j.jece.2019.103632>
- Tian, Y., Zhang, J., Zuo, W., Chen, L., Cui, Y., Tan, T., 2013. Nitrogen conversion in relation to NH₃ and HCN during microwave pyrolysis of sewage sludge. *Environmental Science and Technology* 47, 3498–3505. <https://doi.org/10.1021/es304248j>
- Tijani, M.M., Aqsha, A., Mahinpey, N., 2016. Development of oil-spill sorbent from straw biomass waste: Experiments and modeling studies. *Journal of Environmental Management* 171, 166–176. <https://doi.org/10.1016/j.jenvman.2016.02.010>
- Tomasi Morgano, M., Leibold, H., Richter, F., Stapf, D., Seifert, H., 2018. Screw pyrolysis technology for sewage sludge treatment. *Waste Management* 73, 487–495. <https://doi.org/10.1016/j.wasman.2017.05.049>
- Trinh, T.N., Jensen, P.A., Kim, D.J., Knudsen, N.O., Sørensen, H.R., 2013. Influence of the pyrolysis temperature on sewage sludge product distribution, bio-oil, and char properties. *Energy and Fuels* 27, 1419–1427. <https://doi.org/10.1021/ef301944r>
- Tripathi, M., Sahu, J.N., Ganesan, P., 2016. Effect of process parameters on production of biochar from biomass waste through pyrolysis: A review. *Renewable and Sustainable Energy Reviews* 55, 467–481. <https://doi.org/10.1016/j.rser.2015.10.122>
- Tsai, W.T., Chang, J.H., Hsien, K.J., Chang, Y.M., 2009. Production of pyrolytic liquids from industrial sewage sludges in an induction-heating reactor. *Bioresource Technology* 100, 406–412. <https://doi.org/10.1016/j.biortech.2008.06.013>
- Vyazovkin, S., Chrissafis, K., Di Lorenzo, M.L., Koga, N., Pijolat, M., Roduit, B., Sbirrazzuoli, N., Suñol, J.J., 2014. ICTAC Kinetics Committee recommendations for collecting experimental thermal analysis data for kinetic computations. *Thermochimica Acta* 590, 1–23. <https://doi.org/10.1016/j.tca.2014.05.036>
- Wang, K., Zheng, Y., Zhu, X., Brewer, C.E., Brown, R.C., 2017. Ex-situ catalytic pyrolysis of wastewater sewage sludge – A micro-pyrolysis study. *Bioresource Technology* 232, 229–234. <https://doi.org/10.1016/j.biortech.2017.02.015>
- Wang, S., Wang, J., 2019. Activation of peroxymonosulfate by sludge-derived biochar for the degradation of triclosan in water and wastewater. *Chemical Engineering Journal* 356, 350–358.
- Wang, X., Deng, S., Tan, H., Adeosun, A., Vujanović, M., Yang, F., Duić, N., 2016. Synergetic effect of sewage sludge and biomass co-pyrolysis: A combined study in thermogravimetric analyzer and a fixed bed reactor. *Energy Conversion and Management* 118, 399–405. <https://doi.org/10.1016/j.enconman.2016.04.014>
- Wu, B., Dai, X., Chai, X., 2020. Critical review on dewatering of sewage sludge: Influential

- mechanism, conditioning technologies and implications to sludge re-utilizations. *Water Research* 180, 115912. <https://doi.org/https://doi.org/10.1016/j.watres.2020.115912>
- Wu, H., Quyn, D.M., Li, C.-Z., 2002. Volatilisation and catalytic effects of alkali and alkaline earth metallic species during the pyrolysis and gasification of Victorian brown coal. Part III. The importance of the interactions between volatiles and char at high temperature. *Fuel* 81, 1033–1039. [https://doi.org/https://doi.org/10.1016/S0016-2361\(02\)00011-X](https://doi.org/https://doi.org/10.1016/S0016-2361(02)00011-X)
- Wu, Z., Wang, S., Zhao, J., Chen, L., Meng, H., 2016. Thermochemical behavior and char morphology analysis of blended bituminous coal and lignocellulosic biomass model compound co-pyrolysis: Effects of cellulose and carboxymethylcellulose sodium. *Fuel* 171, 65–73. <https://doi.org/10.1016/j.fuel.2015.12.057>
- Wzorek, M., 2012. Characterisation of the properties of alternative fuels containing sewage sludge. *Fuel Processing Technology* 104, 80–89. <https://doi.org/10.1016/j.fuproc.2012.04.023>
- Xiang, Z., Liang, J., Morgan, H.M., Liu, Y., Mao, H., Bu, Q., 2018a. Thermal behavior and kinetic study for co-pyrolysis of lignocellulosic biomass with polyethylene over Cobalt modified ZSM-5 catalyst by thermogravimetric analysis. *Bioresource Technology* 247, 804–811. <https://doi.org/https://doi.org/10.1016/j.biortech.2017.09.178>
- Xiang, Z., Liang, J., Morgan Jr, H.M., Liu, Y., Mao, H., Bu, Q., 2018b. Thermal behavior and kinetic study for co-pyrolysis of lignocellulosic biomass with polyethylene over Cobalt modified ZSM-5 catalyst by thermogravimetric analysis. *Bioresource Technology* 247, 804–811.
- Xie, Q., Addy, M., Liu, S., Zhang, B., Cheng, Y., Wan, Y., Li, Y., Liu, Y., Lin, X., Chen, P., Ruan, R., 2015. Fast microwave-assisted catalytic co-pyrolysis of microalgae and scum for bio-oil production. *Fuel* 160, 577–582. <https://doi.org/10.1016/j.fuel.2015.08.020>
- Xie, Q.L., Peng, P., Liu, S.Y., Min, M., Cheng, Y.L., Wan, Y.Q., Li, Y., Lin, X.Y., Liu, Y.H., Chen, P., Ruan, R., 2014. Fast microwave-assisted catalytic pyrolysis of sewage sludge for bio-oil production. *Bioresource Technology* 172, 162–168. <https://doi.org/10.1016/j.biortech.2014.09.006>
- Xiong, X., Yu, I.K.M., Cao, L., Tsang, D.C.W., Zhang, S., Ok, Y.S., 2017. A review of biochar-based catalysts for chemical synthesis, biofuel production, and pollution control. *Bioresource Technology* 246, 254–270. <https://doi.org/10.1016/j.biortech.2017.06.163>
- Xu, Q., Tang, S., Wang, J., Ko, J.H., 2018. Pyrolysis kinetics of sewage sludge and its biochar characteristics. *Process Safety and Environmental Protection* 115, 49–56. <https://doi.org/10.1016/j.psep.2017.10.014>
- Xu, X., Zhao, B., Sun, M., Chen, X., Zhang, M., Li, H., Xu, S., 2017. Co-pyrolysis characteristics of municipal sewage sludge and hazelnut shell by TG-DTG-MS and residue analysis. *Waste Management* 62, 91–100. <https://doi.org/10.1016/j.wasman.2017.02.012>
- Xu, Y., Chen, B., 2013. Investigation of thermodynamic parameters in the pyrolysis conversion of

- biomass and manure to biochars using thermogravimetric analysis. *Bioresource Technology* 146, 485–493. <https://doi.org/10.1016/j.biortech.2013.07.086>
- Yan, L., Liu, Y., Zhang, Yudan, Liu, S., Wang, C., Chen, W., Liu, C., Chen, Z., Zhang, Ying, 2020. ZnCl₂ modified biochar derived from aerobic granular sludge for developed microporosity and enhanced adsorption to tetracycline. *Bioresource Technology* 297, 122381. <https://doi.org/10.1016/j.biortech.2019.122381>
- Yang, B., Liu, Y., Liang, Q., Chen, M., Ma, L., Li, L., Liu, Q., Tu, W., Lan, D., Chen, Y., 2019. Evaluation of activated carbon synthesized by one-stage and two-stage co-pyrolysis from sludge and coconut shell. *Ecotoxicology and Environmental Safety* 170, 722–731. <https://doi.org/10.1016/j.ecoenv.2018.11.130>
- Yang, J., Xu, X., Liang, S., Guan, R., Li, H., Chen, Y., Liu, B., Song, J., Yu, W., Xiao, K., Hou, H., Hu, J., Yao, H., Xiao, B., 2018. Enhanced hydrogen production in catalytic pyrolysis of sewage sludge by red mud: Thermogravimetric kinetic analysis and pyrolysis characteristics. *International Journal of Hydrogen Energy* 43, 7795–7807. <https://doi.org/10.1016/j.ijhydene.2018.03.018>
- Yang, Y., Brammer, J.G., Mahmood, A.S.N., Hornung, A., 2014. Intermediate pyrolysis of biomass energy pellets for producing sustainable liquid, gaseous and solid fuels. *Bioresource Technology* 169, 794–799. <https://doi.org/10.1016/j.biortech.2014.07.044>
- Yao, Z., Ma, X., Wu, Z., Yao, T., 2017. TGA–FTIR analysis of co-pyrolysis characteristics of hydrochar and paper sludge. *Journal of Analytical and Applied Pyrolysis* 123, 40–48. <https://doi.org/10.1016/j.jaap.2016.12.031>
- Yu, G., Feng, Y., Chen, D., Yang, M., Yu, T., Dai, X., 2016. In Situ Reforming of the Volatile by Char during Sewage Sludge Pyrolysis. *Energy and Fuels* 30, 10396–10403. <https://doi.org/10.1021/acs.energyfuels.6b01226>
- Zaker, A., Chen, Z., 2021. Catalytic Pyrolysis of Sewage Sludge for Upgrading Bio-Oil Quality Using Sludge-Based Activated Char as an Alternative to HZSM5. *International Journal of Environmental and Ecological Engineering* 8, 194–204.
- Zaker, A., Chen, Z., Wang, X., Zhang, Q., 2019. Microwave-assisted pyrolysis of sewage sludge : A review. *Fuel Processing Technology* 187, 84–104. <https://doi.org/10.1016/j.fuproc.2018.12.011>
- Zaker, A., Chen, Z., Zaheer-Uddin, M., 2021. Catalytic pyrolysis of sewage sludge with HZSM5 and sludge-derived activated char: A comparative study using TGA-MS and artificial neural networks. *Journal of Environmental Chemical Engineering* 9, 105891. <https://doi.org/10.1016/j.jece.2021.105891>
- Zaker, A., Chen, Z., Zaheer-Uddin, M., Guo, J., 2020. Co-pyrolysis of sewage sludge and low-density polyethylene – A thermogravimetric study of thermo-kinetics and thermodynamic parameters. *Journal of Environmental Chemical Engineering* 104554. <https://doi.org/10.1016/j.jece.2020.104554>

- Zhang, B., Xiong, S., Xiao, B., Yu, D., Jia, X., 2011. Mechanism of wet sewage sludge pyrolysis in a tubular furnace. *International Journal of Hydrogen Energy* 36, 355–363. <https://doi.org/10.1016/j.ijhydene.2010.05.100>
- Zhang, H., Gao, Z., Ao, W., Li, J., Liu, G., Fu, J., Ran, C., Liu, Y., Kang, Q., Mao, X., Dai, J., 2017. Microwave pyrolysis of textile dyeing sludge in a continuously operated auger reactor. *Fuel Processing Technology* 166, 174–185. <https://doi.org/10.1016/j.fuproc.2017.05.031>
- Zhang, J., Zuo, W., Tian, Y., Chen, L., Yin, L., Zhang, Jie, 2017a. Sulfur Transformation during Microwave and Conventional Pyrolysis of Sewage Sludge. *Environmental Science and Technology* 51, 709–717. <https://doi.org/10.1021/acs.est.6b03784>
- Zhang, J., Zuo, W., Tian, Y., Yin, L., Gong, Z., Zhang, Jie, 2017b. Release of hydrogen sulfide during microwave pyrolysis of sewage sludge: Effect of operating parameters and mechanism. *Journal of Hazardous Materials* 331, 117–122. <https://doi.org/10.1016/j.jhazmat.2017.02.040>
- Zhang, X., Lei, H., Chen, S., Wu, J., 2016a. Catalytic co-pyrolysis of lignocellulosic biomass with polymers: A critical review. *Green Chemistry* 18, 4145–4169. <https://doi.org/10.1039/c6gc00911e>
- Zhang, X., Lei, H., Zhu, L., Qian, M., Zhu, X., Wu, J., Chen, S., 2016b. Enhancement of jet fuel range alkanes from co-feeding of lignocellulosic biomass with plastics via tandem catalytic conversions. *Applied Energy* 173, 418–430. <https://doi.org/10.1016/j.apenergy.2016.04.071>
- Zhang, X., Lei, H., Zhu, L., Zhu, X., Qian, M., Yadavalli, G., Wu, J., Chen, S., 2016c. Thermal behavior and kinetic study for catalytic co-pyrolysis of biomass with plastics. *Bioresource Technology* 220, 233–238. <https://doi.org/10.1016/j.biortech.2016.08.068>
- Zhang, X., Zhang, P., Yuan, X., Li, Y., Han, L., 2020. Effect of pyrolysis temperature and correlation analysis on the yield and physicochemical properties of crop residue biochar. *Bioresource Technology* 296, 122318. <https://doi.org/https://doi.org/10.1016/j.biortech.2019.122318>
- Zhang, Y., Duan, D., Lei, H., Villota, E., Ruan, R., 2019. Jet fuel production from waste plastics via catalytic pyrolysis with activated carbons. *Applied Energy* 251, 113337. <https://doi.org/10.1016/j.apenergy.2019.113337>
- Zhang, Y., Lei, H., Yang, Z., Duan, D., Villota, E., Ruan, R., 2018a. From glucose-based carbohydrates to phenol-rich bio-oils integrated with syngas production via catalytic pyrolysis over an activated carbon catalyst. *Green Chemistry* 20, 3346–3358. <https://doi.org/10.1039/c8gc00593a>
- Zhang, Y., Lei, H., Yang, Z., Qian, K., Villota, E., 2018b. Renewable High-Purity Mono-Phenol Production from Catalytic Microwave-Induced Pyrolysis of Cellulose over Biomass-Derived Activated Carbon Catalyst. *ACS Sustainable Chemistry and Engineering* 6, 5349–5357. <https://doi.org/10.1021/acssuschemeng.8b00129>

- Zhao, B., Xu, X., Li, H., Chen, X., Zeng, F., 2018. Kinetics evaluation and thermal decomposition characteristics of co-pyrolysis of municipal sewage sludge and hazelnut shell. *Bioresource Technology* 247, 21–29. <https://doi.org/10.1016/j.biortech.2017.09.008>
- Zhao, S., Yin, L., Zhou, Q., Liu, C., Zhou, K., 2020. In situ self-assembly of zeolitic imidazolate frameworks on the surface of flexible polyurethane foam: Towards for highly efficient oil spill cleanup and fire safety. *Applied Surface Science* 506, 144700. <https://doi.org/10.1016/j.apsusc.2019.144700>
- Zheng, Y., Tao, L., Yang, X., Huang, Y., Liu, C., Zheng, Z., 2018. Study of the thermal behavior, kinetics, and product characterization of biomass and low-density polyethylene co-pyrolysis by thermogravimetric analysis and pyrolysis-GC/MS. *Journal of Analytical and Applied Pyrolysis* 133, 185–197. <https://doi.org/10.1016/j.jaap.2018.04.001>
- Zhou, J., Liu, S., Zhou, N., Fan, L., Zhang, Y., Peng, P., Anderson, E., Ding, K., Wang, Y., Liu, Y., Chen, P., Ruan, R., 2018. Development and application of a continuous fast microwave pyrolysis system for sewage sludge utilization. *Bioresource Technology* 256, 295–301. <https://doi.org/10.1016/j.biortech.2018.02.034>
- Zhu, S., Wang, W., Xu, Y., Zhu, Z., Liu, Z., Cui, F., 2019. Iron sludge-derived magnetic Fe⁰/Fe₃C catalyst for oxidation of ciprofloxacin via peroxy monosulfate activation. *Chemical Engineering Journal* 365, 99–110. <https://doi.org/10.1016/j.cej.2019.02.011>
- Zhu, X., Chen, Z., Xiao, B., Hu, Z., Hu, M., Liu, C., Zhang, Q., 2015. Co-pyrolysis behaviors and kinetics of sewage sludge and pine sawdust blends under non-isothermal conditions. *Journal of Thermal Analysis and Calorimetry* 119, 2269–2279. <https://doi.org/10.1007/s10973-014-4321-2>
- Zielińska, A., Oleszczuk, P., Charnas, B., Skubiszewska-Zięba, J., Pasieczna-Patkowska, S., 2015. Effect of sewage sludge properties on the biochar characteristic. *Journal of Analytical and Applied Pyrolysis* 112, 201–213. <https://doi.org/10.1016/j.jaap.2015.01.025>
- Zou, J., Dai, Y., Wang, X., Ren, Z., Tian, C., Pan, K., Li, S., Abuobaidah, M., Fu, H., 2013. Structure and adsorption properties of sewage sludge-derived carbon with removal of inorganic impurities and high porosity. *Bioresource Technology* 142, 209–217. <https://doi.org/10.1016/j.biortech.2013.04.064>
- Zubrik, A., Matik, M., Hredzák, S., Lovás, M., Danková, Z., Kováčová, M., Briančin, J., 2017. Preparation of chemically activated carbon from waste biomass by single-stage and two-stage pyrolysis. *Journal of Cleaner Production* 143, 643–653. <https://doi.org/10.1016/j.jclepro.2016.12.061>

Appendix A: Compounds of bio-oil detected by GC/MS

Table A.1. Major chemical compounds present in pyrolytic bio-oil of SS.

| No. | RT (min) | Compound | MW | CAS Number | Relative Content % |
|-----|----------|--------------------------------|---------|-------------|--------------------|
| 1 | 3.838 | Pyridine | 79.042 | 000110-86-1 | 0.15 |
| 2 | 4.283 | Toluene | 92.063 | 000108-88-3 | 0.33 |
| 3 | 4.843 | Ethanimidic acid, ethyl ester | 87.068 | 001000-84-6 | 0.22 |
| 4 | 5.066 | Diglycolic acid | 134.022 | 000110-99-6 | 0.20 |
| 5 | 5.912 | Butanoic acid | 88.052 | 000107-92-6 | 2.34 |
| 6 | 6.923 | Pyridine, 3-methyl- | 93.058 | 000108-99-6 | 0.77 |
| 7 | 7.14 | 2-Propanone, 1-(acetyloxy)- | 116.047 | 000592-20-1 | 0.26 |
| 8 | 7.413 | Butanoic acid, 2-methyl- | 102.068 | 000116-53-0 | 0.32 |
| 9 | 7.718 | Styrene | 104.063 | 000100-42-5 | 0.42 |
| 10 | 8.024 | Heptanoic acid | 130.099 | 000111-14-8 | 0.17 |
| 11 | 8.208 | 2-Cyclopenten-1-one, 2-methyl- | 96.058 | 001120-73-6 | 0.48 |
| 12 | 8.425 | Pentanoic acid | 102.068 | 000109-52-4 | 0.51 |
| 13 | 9.061 | Pyridine, 2,5-dimethyl- | 107.073 | 000589-93-5 | 0.10 |
| 14 | 9.474 | Pyridine, 2,5-dimethyl- | 107.073 | 000589-93-5 | 0.21 |
| 15 | 9.761 | Hexanamide | 115.1 | 000628-02-4 | 0.13 |
| 16 | 9.901 | Pyridine, 3-ethyl- | 107.073 | 000536-78-7 | 0.10 |
| 17 | 10.072 | 2-Cyclopenten-1-one, 3-methyl- | 96.058 | 002758-18-1 | 0.42 |
| 18 | 10.632 | .alpha.-Methylstyrene | 118.078 | 000098-83-9 | 0.20 |
| 19 | 10.957 | Phenol | 94.042 | 000108-95-2 | 0.53 |

| | | | | | |
|----|--------|--|---------|-------------|------|
| 20 | 11.313 | Butyl aldoxime, 3-methyl-, syn- | 101.084 | 005780-40-5 | 0.72 |
| 21 | 12.121 | 2-Cyclopenten-1-one, 2-hydroxy-3-methyl- (Cyclotene) | 112.052 | 000080-71-7 | 0.46 |
| 22 | 12.439 | 2-Cyclopenten-1-one, 2,3-dimethyl- | 110.073 | 001121-05-7 | 0.25 |
| 23 | 12.986 | Benzene, butyl- | 134.11 | 000104-51-8 | 0.24 |
| 24 | 13.196 | Phenol, 2-methyl- | 108.058 | 000095-48-7 | 0.16 |
| 25 | 13.603 | 2-Pyrrolidinone | 85.053 | 000616-45-5 | 0.70 |
| 26 | 13.877 | Phenol, 4-methyl- | 108.058 | 000106-44-5 | 0.65 |
| 27 | 14.106 | 1-Undecene | 154.172 | 000821-95-4 | 0.28 |
| 28 | 14.367 | Undecane | 156.188 | 001120-21-4 | 0.28 |
| 29 | 14.545 | 1-Nonene | 126.141 | 000124-11-8 | 0.19 |
| 30 | 14.971 | 1H-Imidazole-4-carboxylic acid, methyl ester | 126.043 | 017325-26-7 | 0.11 |
| 31 | 15.563 | Benzyl nitrile | 117.058 | 000140-29-4 | 0.27 |
| 32 | 15.824 | 1,4-Dihydronaphthalene | 130.078 | 000612-17-9 | 0.16 |
| 33 | 16.04 | 1H-Indene, 1-methyl- | 130.078 | 000767-59-9 | 0.38 |
| 34 | 16.466 | Acetamide, N-(4-hydroxyphenyl)- | 151.063 | 000103-90-2 | 0.13 |
| 35 | 16.848 | 2-Piperidinone | 99.068 | 000675-20-7 | 1.22 |
| 36 | 17.102 | Cyclododecane | 168.188 | 000294-62-2 | 0.42 |
| 37 | 17.338 | Dodecane | 170.203 | 000112-40-3 | 0.37 |
| 38 | 18.076 | 4-Ethoxystyrene | 148.089 | 005459-40-5 | 0.13 |
| 39 | 18.547 | Benzenepropanenitrile | 131.073 | 000645-59-0 | 0.15 |
| 40 | 19.208 | Benzeneacetic acid | 136.052 | 000103-82-2 | 0.77 |
| 41 | 19.609 | 1H-Inden-1-one, 2,3-dihydro- | 132.058 | 000083-33-0 | 0.23 |

| | | | | | |
|----|--------|---|---------|--------------|------|
| 42 | 19.921 | 1-Tridecene | 182.203 | 002437-56-1 | 0.49 |
| 43 | 20.131 | Tridecane | 184.219 | 000629-50-5 | 0.51 |
| 44 | 20.442 | Naphthalene, 2-methyl- | 142.078 | 000091-57-6 | 0.07 |
| 45 | 21.46 | 4-Nitrosophenyl-.beta.-phenylpropionate | 255.09 | 1000129-40-0 | 0.37 |
| 46 | 21.823 | Benzene, heptyl- | 176.157 | 001078-71-3 | 0.14 |
| 47 | 22.154 | n-Decanoic acid | 172.146 | 000334-48-5 | 0.29 |
| 48 | 22.567 | 1-Tetradecene | 196.219 | 001120-36-1 | 0.76 |
| 49 | 22.771 | Tetradecane | 198.235 | 000629-59-4 | 0.51 |
| 50 | 24.177 | Prefox | 161.087 | 002941-55-1 | 0.12 |
| 51 | 24.393 | 1H-Isoindole-1,3(2H)-dione, 2-(hydroxymethyl)- | 177.043 | 000118-29-6 | 0.32 |
| 52 | 24.692 | Cyclododecane | 168.188 | 000294-62-2 | 0.12 |
| 53 | 25.074 | 1-Pentadecene | 210.235 | 013360-61-7 | 0.60 |
| 54 | 25.265 | Pentadecane | 212.25 | 000629-62-9 | 0.88 |
| 55 | 26.951 | Dodecanoic acid | 200.178 | 000143-07-7 | 1.61 |
| 56 | 27.447 | 1-Hexadecene | 224.25 | 000629-73-2 | 0.38 |
| 57 | 27.612 | Hexadecane | 226.266 | 000544-76-3 | 0.35 |
| 58 | 29.095 | (1R-(1Alpha,3beta,4beta))-1-isopropenyl-4-methyl-1,3-cyclohexanediol 3-acetate | 212.141 | 057211-60-6 | 0.29 |
| 59 | 29.476 | 8-Heptadecene | 238.266 | 002579-04-6 | 0.64 |
| 60 | 29.852 | Heptadecane | 240.282 | 000629-78-7 | 1.06 |
| 61 | 30.463 | Thiirane, octyl- | 172.129 | 013748-26-0 | 0.15 |
| 62 | 30.908 | Cyclohexanone, 2,2-dimethyl-5-(3-methyloxiranyl)-, [2.alpha.(R*),3.alpha.]-(.+.)- | 182.131 | 141033-65-0 | 0.16 |

| | | | | | |
|----|--------|---|---------|--------------|-------|
| 63 | 31.328 | Tetradecanoic acid | 228.209 | 000544-63-8 | 1.97 |
| 64 | 31.601 | 1-Octadecene | 252.282 | 000112-88-9 | 0.34 |
| 65 | 31.964 | Nonahexacontanoic acid | 999.07 | 040710-32-5 | 0.32 |
| 66 | 32.568 | 1,2-Benzisothiazole, 3-(hexahydro-1H-azepin-1-yl)-, 1,1-dioxide | 264.093 | 309735-29-3 | 0.31 |
| 67 | 32.74 | Pentadecanoic acid | 242.225 | 001002-84-2 | 0.36 |
| 68 | 32.995 | 1-(2-Chlorophenyl)piperazine | 196.077 | 039512-50-0 | 0.12 |
| 69 | 33.306 | Pentadecanoic acid | 242.225 | 001002-84-2 | 0.50 |
| 70 | 33.688 | Cyclopentadecane | 210.235 | 000295-48-7 | 0.59 |
| 71 | 34.051 | Pentadecanenitrile | 223.23 | 018300-91-9 | 1.74 |
| 72 | 34.534 | Hexadecanoic acid, methyl ester | 270.256 | 000112-39-0 | 0.75 |
| 73 | 35.05 | Z-7-Hexadecenoic acid | 254.225 | 1000130-90-8 | 1.58 |
| 74 | 35.52 | n-Hexadecanoic acid | 256.24 | 000057-10-3 | 14.45 |
| 75 | 36.481 | Cyclotetradecane | 196.219 | 000295-17-0 | 0.46 |
| 76 | 36.665 | 9-Octadecenoic acid, (E)- | 282.256 | 000112-79-8 | 0.27 |
| 77 | 37.168 | Cyclopentadecanone, 2-hydroxy- | 240.209 | 004727-18-8 | 0.51 |
| 78 | 37.575 | Oleanitrile | 263.261 | 1000308-88-1 | 2.43 |
| 79 | 37.932 | Heptadecanenitrile | 251.261 | 005399-02-0 | 2.44 |
| 80 | 38.307 | Heptadecanoic acid, 14-methyl-, methyl ester, (+/-)- | 298.287 | 057274-45-0 | 0.81 |
| 81 | 38.803 | 6-Octadecenoic acid, (Z)- | 282.256 | 000593-39-5 | 12.16 |
| 82 | 39.102 | Octadecanoic acid | 284.272 | 000057-11-4 | 3.96 |
| 83 | 39.369 | Tetradecanamide | 227.225 | 000638-58-4 | 2.28 |
| 84 | 39.904 | 1,4-Diallyl-1,1,2,2,3,3,4,4-octamethyltetrasilane | 314.174 | 1000311-71-7 | 0.24 |

| | | | | | |
|-----|--------|---|---------|--------------|------|
| 85 | 41.1 | Cyclohexane, 1-(1,5-dimethylhexyl)-4-(4-methylpentyl)- | 280.313 | 056009-20-2 | 0.20 |
| 86 | 41.291 | Octadec-9-enoic acid | 282.256 | 1000190-13-7 | 0.23 |
| 87 | 42.417 | 9-Octadecenamide, (Z)- | 281.272 | 000301-02-0 | 1.17 |
| 88 | 42.728 | Octadecanamide | 283.288 | 000124-26-5 | 0.88 |
| 89 | 43.288 | Cyclotetradecanone oxime | 225.209 | 072255-85-7 | 0.18 |
| 90 | 43.651 | Octadec-9-enoic acid | 282.256 | 1000190-13-7 | 0.21 |
| 91 | 44.561 | 2-Diethylthiophosphorylmethyl allophanate | 270.044 | 1000140-64-2 | 0.30 |
| 92 | 45.248 | 1,2-Benzenedicarboxylic acid, mono(2-ethylhexyl) ester | 278.152 | 004376-20-9 | 1.26 |
| 93 | 45.699 | Piperazine, 1-[2-[.alpha.-(2-chlorophenyl)-3-chlorobenzyloxy]ethyl]-4-methyl- | 378.127 | 1000137-94-7 | 0.14 |
| 94 | 47.175 | 9-Octadecenoic acid, (E)- | 282.256 | 000112-79-8 | 0.13 |
| 95 | 47.43 | Tricosane | 324.376 | 000638-67-5 | 0.16 |
| 96 | 48.136 | Furane-2-carboxaldehyde, 5-(2-benzothiazolylthio)- | 260.992 | 039689-07-1 | 0.11 |
| 97 | 48.41 | Z-12-Pentacosene | 350.391 | 1000131-09-4 | 0.45 |
| 98 | 48.747 | Cholest-3-ene, (5.alpha.)- | 370.36 | 028338-69-4 | 2.50 |
| 99 | 49.122 | Cholest-7-ene, (5.alpha.)- | 370.36 | 040071-65-6 | 1.63 |
| 100 | 49.415 | Phthalic acid, hexyl neopentyl ester | 320.199 | 1000315-29-9 | 1.53 |
| 101 | 49.854 | 4-(4-(2-Naphthoxy)butylthio)-5-methylpyrimidin-2(1H)-one | 340.125 | 118365-79-0 | 0.51 |
| 102 | 50.191 | Cholesta-3,5-diene | 368.344 | 000747-90-0 | 1.88 |
| 103 | 50.592 | 7-Cholesten-3-one | 384.339 | 013097-64-8 | 0.44 |
| 104 | 51.114 | Pyridine-3-carboxamide, oxime, N-(2-trifluoromethylphenyl)- | 281.078 | 288246-53-7 | 0.90 |
| 105 | 51.406 | 2,4-Dibenzyl-5,8-dimethoxy-6-methyl-1-naphthol | 398.188 | 086649-80-1 | 1.10 |
| 106 | 51.769 | 2,4-Dibenzyl-5,8-dimethoxy-6-methyl-1-naphthol | 398.188 | 086649-80-1 | 1.18 |

| | | | | | |
|-----|--------|---|---------|--------------|------|
| 107 | 52.042 | Corynan-16-carboxylic acid, 16,17-didehydro-9,17-dimethoxy-, methyl ester, (16E)- | 398.221 | 004697-67-0 | 0.73 |
| 108 | 52.354 | Ergost-22-en-3-ol, (3.alpha.,5.beta.,22E)- | 400.371 | 055527-92-9 | 0.62 |
| 109 | 52.628 | Epicholesterol | 388.371 | 000516-95-0 | 0.68 |
| 110 | 52.793 | Stigmastan-3,5-diene | 396.376 | 1000214-16-4 | 1.15 |
| 111 | 53.137 | Cholest-5-en-3-ol (3.beta.)- | 386.355 | 000057-88-5 | 1.91 |
| 112 | 53.684 | Pyridine-3-carboxamide, oxime, N-(2-trifluoromethylphenyl)- | 281.078 | 288246-53-7 | 0.75 |
| 113 | 54.937 | Cholest-4-en-3-one | 384.339 | 000601-57-0 | 0.92 |
| 114 | 55.421 | 3'-Chlorooxanilic acid N'-(3-ethoxy-4-hydroxybenzylidene)hydrazide | 361.083 | 328018-74-2 | 0.57 |
| 115 | 56.54 | Pyridine-3-carboxamide, oxime, N-(2-trifluoromethylphenyl)- | 281.078 | 288246-53-7 | 0.43 |
| 116 | 56.827 | Hexadecanoic acid, hexadecyl ester | 480.491 | 000540-10-3 | 0.67 |

Table A.2. Major chemical compounds present in pyrolytic bio-oil of SSHZSM5@2-1.

| No. | RT (min) | Compound | MW | CAS Number | Relative content % |
|-----|-------------|--------------------------------------|---------|-------------|--------------------------|
| 1 | 3.698 | 1,4-Cyclohexadiene, 1-methyl- | 94.078 | 004313-57-9 | 1.24 |
| 2 | 3.78 | Pyridine | 79.042 | 000110-86-1 | 1.20 |
| 3 | 4.022 | Cyclopentene, 3-ethyl- | 96.094 | 000694-35-9 | 1.74 |
| 4 | 4.219 | Toluene | 92.063 | 000108-88-3 | 12.22 |
| 5 | 5.021 | Butanoic acid | 88.052 | 000107-92-6 | 7.11 |
| 6 | 5.18 | Butanoic acid | 88.052 | 000107-92-6 | 6.90 |
| 7 | 6.414 | Butanoic acid, 3-methyl- | 102.068 | 000503-74-2 | 2.20 |
| 8 | 6.72 | Ethylbenzene | 106.078 | 000100-41-4 | 3.42 |
| 9 | 6.968 | p-Xylene | 106.078 | 000106-42-3 | 6.27 |
| 10 | 7.642 | 1,3,5,7-Cyclooctatetraene | 104.063 | 000629-20-9 | 4.32 |
| 11 | 9.913 | Benzene, 1-ethyl-2-methyl- | 120.094 | 000611-14-3 | 2.98 |
| 12 | 10.69 | Phenol | 94.042 | 000108-95-2 | 2.02 |
| 13 | 10.89 | Benzene, 1,2,3-trimethyl- | 120.094 | 000526-73-8 | 1.09 |
| 14 | 13.64 | Phenol, 3-methyl- | 108.058 | 000108-39-4 | 2.27 |
| 15 | 18.27 | Isoquinoline | 129.058 | 000119-65-3 | 0.80 |
| 16 | 18.91 | Naphthalene, 1,2-dihydro-4-methyl- | 144.094 | 004373-13-1 | 0.84 |
| 17 | 19.90 | 1,4-Methanonaphthalene, 1,4-dihydro- | 142.078 | 004453-90-1 | 4.17 |
| 18 | 22.48 | 1H-Indole, 1-methyl- | 131.073 | 000603-76-9 | 3.03 |
| 19 | 22.79 | Naphthalene, 2,7-dimethyl- | 156.094 | 000582-16-1 | 1.83 |
| 20 | 24.94 | 1-Pentadecene | 210.235 | 013360-61-7 | 1.20 |

| | | | | | |
|----|-------|----------------------------|---------|-------------|-------|
| 21 | 29.67 | Tetradecanenitrile 4 | 209.214 | 000629-63-0 | 1.86 |
| 22 | 33.92 | Pentadecanenitrile 3 | 223.23 | 018300-91-9 | 15.05 |
| 23 | 37.80 | Heptadecanenitrile 4 | 251.261 | 005399-02-0 | 7.56 |
| 24 | 48.6 | Cholest-3-ene, (5.alpha.)- | 370.36 | 028338-69-4 | 3.71 |
| 25 | 48.98 | Cholest-5-ene 2 | 370.36 | 000570-74-1 | 2.33 |
| 26 | 50.06 | Cholesta-3,5-diene 4 | 368.344 | 000747-90-0 | 2.67 |

Table A.3. Major chemical compounds present in pyrolytic bio-oil of SSAC@2-1.

| No. | RT (min) | Compound | MW | CAS Number | Relative content % |
|-----|-------------|------------------------------------|---------|--------------|--------------------------|
| 1 | 3.717 | 1,3,5-Heptatriene, (E,E)- | 94.078 | 017679-93-5 | 1.13 |
| 2 | 3.793 | Pyridine | 79.042 | 000110-86-1 | 1.08 |
| 3 | 4.029 | Cyclopentene, 3-ethyl- | 96.094 | 000694-35-9 | 1.64 |
| 4 | 4.226 | Toluene | 92.063 | 000108-88-3 | 8.93 |
| 5 | 4.792 | 1-Octene | 112.125 | 000111-66-0 | 5.82 |
| 6 | 4.957 | Ethyl .alpha.-d-glucopyranoside | 208.095 | 1000127-29-4 | 4.60 |
| 7 | 5.937 | 2-Cyclopenten-1-one | 82.042 | 000930-30-3 | 1.88 |
| 8 | 6.72 | Ethylbenzene | 106.078 | 000100-41-4 | 3.25 |
| 9 | 6.981 | p-Xylene | 106.078 | 000106-42-3 | 2.47 |
| 10 | 7.642 | Styrene | 104.063 | 000100-42-5 | 5.71 |
| 11 | 7.922 | Nonane | 128.157 | 000111-84-2 | 1.32 |
| 12 | 8.119 | 2-Cyclopenten-1-one, 2-methyl- | 96.058 | 001120-73-6 | 2.03 |
| 13 | 8.399 | 2-Hexene, (E)- | 84.094 | 004050-45-7 | 1.70 |
| 14 | 9.964 | 2-Cyclopenten-1-one, 3-methyl- | 96.058 | 002758-18-1 | 4.01 |
| 15 | 10.702 | Phenol | 94.042 | 000108-95-2 | 1.14 |
| 16 | 10.88 | 1-Decene | 140.157 | 000872-05-9 | 1.91 |
| 17 | 11.122 | Decane | 142.172 | 000124-18-5 | 1.97 |
| 18 | 12.344 | 2-Cyclopenten-1-one, 2,3-dimethyl- | 110.073 | 001121-05-7 | 1.29 |
| 19 | 13.215 | Acetophenone | 120.058 | 000098-86-2 | 1.37 |
| 20 | 13.635 | Phenol, 4-methyl- | 108.058 | 000106-44-5 | 0.84 |

| | | | | | |
|----|--------|------------------------------------|---------|-------------|------|
| 21 | 14.011 | Cyclopropane, 1-heptyl-2-methyl- | 154.172 | 074663-91-5 | 1.07 |
| 22 | 15.156 | Benzyl methyl ketone | 134.073 | 000103-79-7 | 1.19 |
| 23 | 17.007 | Cyclododecane | 168.188 | 000294-62-2 | 2.84 |
| 24 | 17.236 | Dodecane | 170.203 | 000112-40-3 | 1.12 |
| 25 | 18.941 | Naphthalene, 1,2-dihydro-3-methyl- | 144.094 | 002717-44-4 | 3.34 |
| 26 | 19.819 | 1-Tridecene | 182.203 | 002437-56-1 | 4.27 |
| 27 | 20.035 | Tridecane | 184.219 | 000629-50-5 | 2.60 |
| 28 | 22.472 | 2-Tetradecene, (E)- | 196.219 | 035953-53-8 | 5.85 |
| 29 | 22.669 | Tetradecane | 198.235 | 000629-59-4 | 3.17 |
| 30 | 24.972 | 1-Pentadecene | 210.235 | 013360-61-7 | 2.67 |
| 31 | 25.157 | Pentadecane | 212.25 | 000629-62-9 | 3.41 |
| 32 | 27.345 | 1-Hexadecene | 224.25 | 000629-73-2 | 0.57 |
| 33 | 29.744 | Hexadecane | 226.266 | 000544-76-3 | 2.40 |
| 34 | 33.949 | 2-Heptadecanone | 254.261 | 002922-51-2 | 3.75 |
| 35 | 37.448 | Cyclopropanoic aldehyde, 2-octyl- | 280.277 | 056196-06-6 | 2.11 |
| 36 | 37.798 | 2-Nonadecanone | 282.292 | 000629-66-3 | 2.56 |
| 37 | 48.607 | Cholest-4-ene | 370.36 | 016732-86-8 | 1.81 |
| 38 | 48.989 | Cholest-7-ene, (5.alpha.)- | 370.36 | 040071-65-6 | 1.19 |

Table A.4. Major chemical compounds present in pyrolytic bio-oil of SSHZSM5@1-1.

| No. | RT (min) | Compound | MW | CAS Number | Relative content % |
|-----|----------|-----------------------------------|---------|--------------|--------------------|
| 1 | 3.698 | 1,4-Cyclohexadiene, 1-methyl- | 94.078 | 004313-57-9 | 1.21 |
| 2 | 3.78 | Pyridine | 79.042 | 000110-86-1 | 1.34 |
| 3 | 4.219 | Toluene | 92.063 | 000108-88-3 | 15.65 |
| 4 | 4.474 | 5-Heptyn-3-ol | 112.089 | 1000231-49-9 | 1.23 |
| 5 | 4.919 | Butanoic acid | 88.052 | 000107-92-6 | 4.16 |
| 6 | 5.014 | 4-Octene, (E)- | 112.125 | 014850-23-8 | 0.90 |
| 7 | 6.274 | Hexanoic acid, 6-bromo- | 193.994 | 004224-70-8 | 0.95 |
| 8 | 6.719 | Ethylbenzene | 106.078 | 000100-41-4 | 2.81 |
| 9 | 6.968 | p-Xylene | 106.078 | 000106-42-3 | 9.37 |
| 10 | 7.629 | Styrene | 104.063 | 000100-42-5 | 3.69 |
| 11 | 9.601 | Benzene, propyl- | 120.094 | 000103-65-1 | 1.38 |
| 12 | 9.913 | Benzene, 1-ethyl-2-methyl- | 120.094 | 000611-14-3 | 3.36 |
| 13 | 10.715 | Phenol | 94.042 | 000108-95-2 | 1.55 |
| 14 | 10.893 | Benzene, 1,3,5-trimethyl- | 120.094 | 000108-67-8 | 2.58 |
| 15 | 12.49 | Indene | 116.063 | 000095-13-6 | 1.45 |
| 16 | 13.654 | Phenol, 3-methyl- | 108.058 | 000108-39-4 | 1.45 |
| 17 | 16.74 | Naphthalene | 128.063 | 000091-20-3 | 1.39 |
| 18 | 18.279 | Quinoline | 129.058 | 000091-22-5 | 4.19 |
| 19 | 18.915 | 2-Propenenitrile, 3-phenyl-, (E)- | 129.058 | 001885-38-7 | 1.20 |
| 20 | 19.927 | Indole | 117.058 | 000120-72-9 | 7.17 |

| | | | | | |
|----|--------|----------------------------|---------|-------------|-------|
| 21 | 22.491 | 1H-Indole, 4-methyl- | 131.073 | 016096-32-5 | 7.71 |
| 22 | 22.796 | Naphthalene, 2,7-dimethyl- | 156.094 | 000582-16-1 | 1.43 |
| 23 | 24.953 | 1H-Indole, 2,3-dimethyl- | 145.089 | 000091-55-4 | 4.16 |
| 24 | 29.673 | Tetradecanenitrile | 209.214 | 000629-63-0 | 2.86 |
| 25 | 33.93 | Pentadecanenitrile | 223.23 | 018300-91-9 | 14.02 |
| 26 | 37.836 | Octadecanenitrile | 265.277 | 000638-65-3 | 2.81 |

Table A.5. Major chemical compounds present in pyrolytic bio-oil of SSAC@1-1.

| No. | RT (min) | Compound | MW | CAS Number | Relative content % |
|-----|----------|---|---------|--------------|--------------------|
| 1 | 3.755 | Pyridine | 79.042 | 000110-86-1 | 3.00 |
| 2 | 4.022 | 1-Ethylcyclopentene | 96.094 | 002146-38-5 | 1.66 |
| 3 | 4.219 | Toluene | 92.063 | 000108-88-3 | 10.70 |
| 4 | 4.506 | 1-Butene, 3,3-dimethyl- | 84.094 | 000558-37-2 | 1.39 |
| 5 | 4.779 | 2-Octene | 112.125 | 000111-67-1 | 7.30 |
| 6 | 4.995 | Octane | 114.141 | 000111-65-9 | 2.18 |
| 7 | 5.193 | 1H-Pyrazole, 4,5-dihydro-4,5-dimethyl- | 98.084 | 028019-94-5 | 1.37 |
| 8 | 5.466 | Pyridine, 2-methyl- | 93.058 | 000109-06-8 | 0.98 |
| 9 | 5.918 | 2-Cyclopenten-1-one | 82.042 | 000930-30-3 | 2.96 |
| 10 | 6.261 | Formic acid hydrazide | 60.032 | 000624-84-0 | 0.93 |
| 11 | 6.427 | 1H-Pyrrole, 3-methyl- | 81.058 | 000616-43-3 | 0.48 |
| 12 | 6.739 | o-Xylene | 106.078 | 000095-47-6 | 1.79 |
| 13 | 6.974 | p-Xylene | 106.078 | 000106-42-3 | 1.79 |
| 14 | 7.629 | Styrene | 104.063 | 000100-42-5 | 6.19 |
| 15 | 7.928 | Nonane | 128.157 | 000111-84-2 | 0.94 |
| 16 | 8.113 | 2-Cyclopenten-1-one, 2-methyl- | 96.058 | 001120-73-6 | 1.65 |
| 17 | 9.97 | 2-Cyclopenten-1-one, 3-methyl- | 96.058 | 002758-18-1 | 2.01 |
| 18 | 10.708 | Phenol | 94.042 | 000108-95-2 | 1.67 |
| 19 | 10.867 | 1-Decene | 140.157 | 000872-05-9 | 1.81 |
| 20 | 11.097 | 2-[5-(1-Hydroxy-1-methylethyl)-2,2-dimethyl[1,3]dioxolan-4-yl]propan-2-ol | 218.152 | 1000190-33-6 | 1.71 |

| | | | | | |
|----|--------|--|---------|--------------|------|
| 21 | 11.949 | 2-Cyclopenten-1-one, 2-hydroxy-3-methyl- | 112.052 | 000080-71-7 | 1.11 |
| 22 | 13.171 | 2-Pyrrolidinone | 85.053 | 000616-45-5 | 2.72 |
| 23 | 13.641 | Phenol, 4-methyl- | 108.058 | 000106-44-5 | 2.57 |
| 24 | 14.144 | 2-Propenal, 3-(dimethylamino)-2-(methylamino)- | 128.095 | 049582-62-9 | 0.97 |
| 25 | 15.862 | Phenol, 2,5-dimethyl- | 122.073 | 000095-87-4 | 1.26 |
| 26 | 16.428 | 2-Piperidinone | 99.068 | 000675-20-7 | 3.94 |
| 27 | 19.742 | 1H-Purine, 8-methyl- | 134.059 | 000934-33-8 | 1.15 |
| 28 | 19.914 | Indole | 117.058 | 000120-72-9 | 2.25 |
| 29 | 20.194 | 1H-Purine, 8-methyl- | 134.059 | 000934-33-8 | 0.48 |
| 30 | 22.472 | 1H-Indole, 7-methyl- | 131.073 | 000933-67-5 | 4.25 |
| 31 | 24.972 | 1-Pentadecene | 210.235 | 013360-61-7 | 3.50 |
| 32 | 25.15 | Pentadecane | 212.25 | 000629-62-9 | 2.39 |
| 33 | 27.332 | 1-Hexadecene | 224.25 | 000629-73-2 | 0.65 |
| 34 | 29.235 | 1,12-Tridecadiene | 180.188 | 021964-48-7 | 2.35 |
| 35 | 29.705 | Heptadecane | 240.282 | 000629-78-7 | 4.56 |
| 36 | 33.93 | Pentadecanenitrile | 223.23 | 018300-91-9 | 7.78 |
| 37 | 37.441 | 9-Tetradecenal, (Z)- | 210.198 | 053939-27-8 | 2.34 |
| 38 | 37.798 | Octadecanenitrile | 265.277 | 000638-65-3 | 2.48 |
| 39 | 48.607 | Acetamide, 2-(adamantan-1-yl)-N-(1-adamantan-1-ylethyl)- | 355.288 | 1000311-05-4 | 0.78 |

Table A.6. Major chemical compounds present in pyrolytic bio-oil of SSHZSM5@4-1.

| No. | RT (min) | Compound | MW | CAS Number | Relative content % |
|-----|----------|----------------------------------|---------|-------------|--------------------|
| 1 | 3.704 | 1,3,5-Heptatriene, (E,E)- | 94.078 | 017679-93-5 | 1.01 |
| 2 | 3.787 | Pyridine | 79.042 | 000110-86-1 | 0.81 |
| 3 | 4.022 | 1-Ethylcyclopentene | 96.094 | 002146-38-5 | 1.36 |
| 4 | 4.219 | Toluene | 92.063 | 000108-88-3 | 5.67 |
| 5 | 4.429 | Acetamide | 59.037 | 000060-35-5 | 1.16 |
| 6 | 5.199 | Butanoic acid | 88.052 | 000107-92-6 | 12.31 |
| 7 | 5.937 | 2-Cyclopenten-1-one | 82.042 | 000930-30-3 | 0.86 |
| 8 | 6.433 | Butanoic acid, 3-methyl- | 102.068 | 000503-74-2 | 2.04 |
| 9 | 6.72 | Ethylbenzene | 106.078 | 000100-41-4 | 2.34 |
| 10 | 6.968 | p-Xylene | 106.078 | 000106-42-3 | 2.66 |
| 11 | 7.636 | Styrene | 104.063 | 000100-42-5 | 3.21 |
| 12 | 9.932 | Benzene, 1-ethyl-2-methyl- | 120.094 | 000611-14-3 | 1.72 |
| 13 | 10.702 | Phenol | 94.042 | 000108-95-2 | 2.53 |
| 14 | 10.899 | Benzene, 1-ethyl-3-methyl- | 120.094 | 000620-14-4 | 0.96 |
| 15 | 11.122 | 3-Heptanol, 4-methyl- | 130.136 | 014979-39-6 | 1.66 |
| 16 | 11.962 | 1,2-Cyclopentanedione, 3-methyl- | 112.052 | 000765-70-8 | 0.77 |
| 17 | 12.865 | 1,2,3,4,5,8-Hexahydronaphthalene | 134.11 | 036231-13-7 | 1.16 |
| 18 | 13.145 | 2-Pyrrolidinone | 85.053 | 000616-45-5 | 1.10 |
| 19 | 13.641 | Phenol, 4-methyl- | 108.058 | 000106-44-5 | 2.00 |
| 20 | 15.442 | Benzonitrile, 2-methyl- | 117.058 | 000529-19-1 | 0.73 |

| | | | | | |
|----|--------|---|---------|--------------|------|
| 21 | 15.715 | Naphthalene, 1,2-dihydro- | 130.078 | 000447-53-0 | 0.55 |
| 22 | 15.881 | Naphthalene, 1,2-dihydro- | 130.078 | 000447-53-0 | 0.96 |
| 23 | 16.46 | 2-Piperidinone | 99.068 | 000675-20-7 | 1.06 |
| 24 | 16.727 | 1H-Indene, 1-methylene- | 128.063 | 002471-84-3 | 0.92 |
| 25 | 18.286 | Isoquinoline | 129.058 | 000119-65-3 | 1.11 |
| 26 | 18.903 | Naphthalene, 1,2-dihydro-4-methyl- | 144.094 | 004373-13-1 | 2.12 |
| 27 | 19.914 | Indolizine | 117.058 | 000274-40-8 | 2.81 |
| 28 | 22.44 | 1H-Indole, 4-methyl- | 131.073 | 016096-32-5 | 2.25 |
| 29 | 22.803 | Naphthalene, 2,7-dimethyl- | 156.094 | 000582-16-1 | 0.86 |
| 30 | 24.94 | Cyclopentadecane | 210.235 | 000295-48-7 | 0.85 |
| 31 | 26.677 | Dodecanoic acid | 200.178 | 000143-07-7 | 1.01 |
| 32 | 29.674 | Tetradecanenitrile | 209.214 | 000629-63-0 | 1.34 |
| 33 | 31.067 | Tetradecanoic acid | 228.209 | 000544-63-8 | 0.18 |
| 34 | 33.917 | Pentadecanenitrile | 223.23 | 018300-91-9 | 8.96 |
| 35 | 34.42 | Pentadecanoic acid, 14-methyl-, methyl ester | 270.256 | 005129-60-2 | 1.02 |
| 36 | 35.1 | n-Hexadecanoic acid | 256.24 | 000057-10-3 | 3.01 |
| 37 | 37.448 | Oleanitrile | 263.261 | 1000308-88-1 | 1.19 |
| 38 | 37.804 | Heptadecanenitrile | 251.261 | 005399-02-0 | 6.25 |
| 39 | 38.173 | Heptadecanoic acid, 16-methyl-, methyl ester | 298.287 | 005129-61-3 | 0.54 |
| 40 | 39.096 | Tetradecanamide | 227.225 | 000638-58-4 | 1.73 |
| 41 | 48.276 | Amidephrine | 244.088 | 003354-67-4 | 0.68 |
| 42 | 48.6 | Cholest-3-ene, (5.beta.)- | 370.36 | 013901-20-7 | 4.49 |

| | | | | | |
|----|--------|--|---------|-------------|------|
| 43 | 48.982 | Cholest-5-ene | 370.36 | 000570-74-1 | 2.95 |
| 44 | 49.275 | Cholest-8(14)-ene, (5.alpha.)- | 370.36 | 054725-42-7 | 1.19 |
| 45 | 50.057 | Cholesta-3,5-diene | 368.344 | 000747-90-0 | 2.87 |
| 46 | 51.272 | 4.alpha.-Methylcholest-7-en-3-one | 398.355 | 013490-57-8 | 1.22 |
| 47 | 51.635 | 2,4-Dibenzyl-5,8-dimethoxy-6-methyl-1-naphthol | 398.188 | 086649-80-1 | 1.12 |
| 48 | 52.653 | 2,2-Dichlorocyclopropanecarboxamide | 152.975 | 075885-60-8 | 0.70 |

Table A.7. Major chemical compounds present in pyrolytic bio-oil of SSAC@4-1.

| | RT (min) | Compound | MW | CAS Number | Relative content % |
|----|-------------|---|---------|-------------|-----------------------|
| 1 | 3.71 | 3-Cyclohexenecarbonyl chloride | 144.034 | 000932-67-2 | 0.62 |
| 2 | 3.774 | Pyridinium, 1-(2-hydrazino-2-oxoethyl)-, chloride | 187.051 | 001126-58-5 | 1.08 |
| 3 | 4.028 | Cyclopentene, 3-ethyl- | 96.094 | 000694-35-9 | 1.38 |
| 4 | 4.219 | Toluene | 92.063 | 000108-88-3 | 7.23 |
| 5 | 4.417 | Acetamide | 59.037 | 000060-35-5 | 1.01 |
| 6 | 4.499 | Acetamide | 59.037 | 000060-35-5 | 1.26 |
| 7 | 4.785 | 1-Octene | 112.125 | 000111-66-0 | 3.55 |
| 8 | 5.008 | .beta.-l-Arabinopyranoside, methyl | 164.068 | 001825-00-9 | 5.03 |
| 9 | 5.352 | Butanoic acid | 88.052 | 000107-92-6 | 9.43 |
| 10 | 5.924 | 2-Cyclopenten-1-one | 82.042 | 000930-30-3 | 1.37 |
| 11 | 6.49 | Butanoic acid, 3-methyl- | 102.068 | 000503-74-2 | 2.19 |
| 12 | 6.732 | Ethylbenzene | 106.078 | 000100-41-4 | 2.30 |
| 13 | 6.866 | Hexanoic acid, 2-methyl- | 130.099 | 004536-23-6 | 0.91 |
| 14 | 6.968 | Benzene, 1,3-dimethyl- | 106.078 | 000108-38-3 | 1.75 |
| 15 | 7.642 | Styrene | 104.063 | 000100-42-5 | 5.07 |
| 16 | 7.865 | Pentanoic acid | 102.068 | 000109-52-4 | 2.39 |
| 17 | 8.126 | 2-Cyclopenten-1-one, 2-methyl- | 96.058 | 001120-73-6 | 0.87 |
| 18 | 9.977 | 2-Cyclopenten-1-one, 3-methyl- | 96.058 | 002758-18-1 | 1.80 |
| 19 | 10.702 | Phenol | 94.042 | 000108-95-2 | 3.86 |
| 20 | 10.861 | 1-Decene | 140.157 | 000872-05-9 | 1.31 |
| 21 | 11.122 | Decane | 142.172 | 000124-18-5 | 1.89 |

| | | | | | |
|----|--------|--|---------|-------------|------|
| 22 | 11.962 | 1,2-Cyclopentanedione, 3-methyl- | 112.052 | 000765-70-8 | 1.24 |
| 23 | 12.961 | Phenol, 2-methyl- | 108.058 | 000095-48-7 | 1.62 |
| 24 | 13.19 | 2-Pyrrolidinone | 85.053 | 000616-45-5 | 2.40 |
| 25 | 13.635 | Phenol, 4-methyl- | 108.058 | 000106-44-5 | 3.65 |
| 26 | 15.474 | Benzonitrile, 2-methyl- | 117.058 | 000529-19-1 | 0.88 |
| 27 | 15.836 | Phenol, 2,3-dimethyl- | 122.073 | 000526-75-0 | 1.01 |
| 28 | 16.428 | 2-Piperidinone | 99.068 | 000675-20-7 | 1.89 |
| 29 | 19.857 | Naphthalene, 1-methyl- | 142.078 | 000090-12-0 | 3.08 |
| 30 | 20.029 | Tridecane | 184.219 | 000629-50-5 | 0.73 |
| 31 | 22.465 | 2-Tetradecene, (E)- | 196.219 | 035953-53-8 | 4.53 |
| 32 | 22.669 | Tetradecane | 198.235 | 000629-59-4 | 2.48 |
| 33 | 24.966 | 1-Pentadecene | 210.235 | 013360-61-7 | 3.07 |
| 34 | 25.15 | Pentadecane | 212.25 | 000629-62-9 | 3.72 |
| 35 | 27.339 | 1-Hexadecene | 224.25 | 000629-73-2 | 1.14 |
| 36 | 29.737 | Heptadecane | 240.282 | 000629-78-7 | 2.05 |
| 37 | 33.936 | Hexadecanenitrile | 237.246 | 000629-79-8 | 2.53 |
| 38 | 37.441 | Cyclohexane, 1-(1,5-dimethylhexyl)- 4-(4-methylpentyl)- | 280.313 | 056009-20-2 | 1.72 |
| 39 | 37.798 | Octadecanenitrile | 265.277 | 000638-65-3 | 2.11 |
| 40 | 48.607 | Cholest-3-ene, (5.beta.)- | 370.36 | 013901-20-7 | 1.78 |
| 41 | 48.982 | Cholestan-3-ol, acetate, (3.beta.,5.alpha.)- | 430.381 | 001255-88-5 | 1.04 |
| 42 | 50.051 | Cholesta-3,5-diene | 368.344 | 000747-90-0 | 1.06 |
